UNIVERSITÀ DEGLI STUDI DI PAVIA
DOTTORATO DI RICERCA IN FISICA – XXXI CICLO

Integrated optics based on Bloch surface waves

Daniele Aurelio

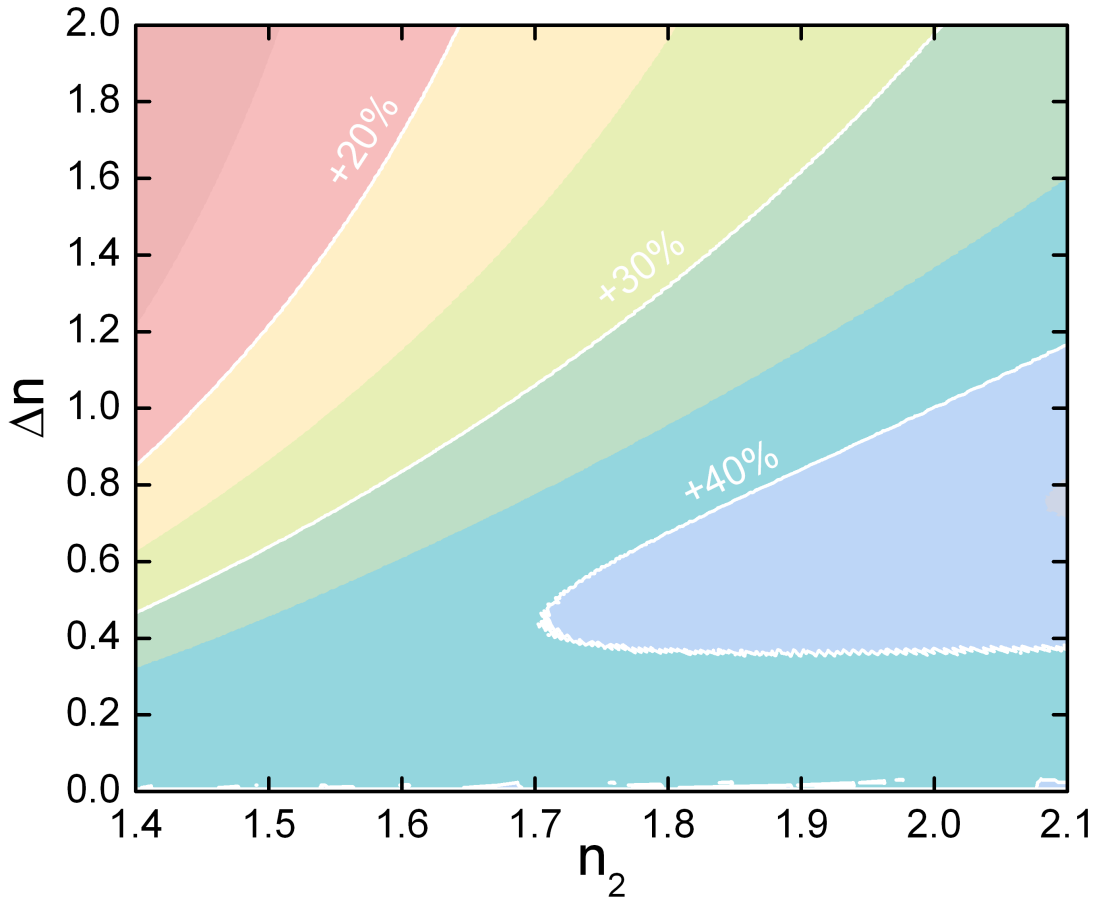

Tesi per il conseguimento del titolo

Università degli Studi di Pavia
Dipartimento di Fisica

DOTTORATO DI RICERCA IN FISICA – XXXI CICLO

Integrated optics based on Bloch surface waves

Daniele Aurelio

Submitted to the Graduate School of Physics in partial fulfilment of the requirements for the degree of

DOTTORE DI RICERCA IN FISICA

DOCTOR OF PHILOSOPHY IN PHYSICS

at the

University of Pavia

Supervisor: Prof. Marco Liscidini

Cover: Contour plot of the ratio between the best surface field of a BSW supported by a truncated periodic multilayer and the best surface field of the TE0 mode supported by an asymmetrical slab as a function of the lower refractive index n_2 and the refractive index contrast Δn.

Integrated optics based on Bloch surface waves
Daniele Aurelio
PhD thesis - University of Pavia
Pavia, Italy - September 2018

Introduction

Over the last decades, the research and development of chip-scale photonics has made giant leaps forward, and has brought about exciting new physics and technological devices that now permeate our lives. One of the fields that has garnered much interest is that of plasmonics, which manipulates light at the nanoscale by taking avail of the optical properties of metallic nanostructures. Surface plasmon polaritons (SPPs) are charge-density oscillations which propagate along the interface between a metal and a dielectric cladding. The SPP propagation constant is given by the simple equation

$$k_{SP} = \frac{\omega}{c}\sqrt{\frac{\varepsilon_m \varepsilon_d}{\varepsilon_m + \varepsilon_d}}, \tag{1}$$

where ω is the angular frequency, c is the speed of light and ε_d and ε_m are the dielectric functions of the dielectric and metallic media, respectively. Thus, k_{SP} inherits the complex nature of the metal dielectric function ε_m: its real part is linked to the effective index of the SPP, whereas its imaginary part entails attenuation along the direction of propagation. These intrinsic losses which plague metallic systems somewhat hinder the strength and the scope of SPP-based technology.

To overcome this limitation, one might be interested in bluntly avoiding metals and resorting to dielectric media: this is where Bloch surface waves (BSWs) come into play.

Bloch surface waves are particular solutions of Maxwell's equations which occur in systems consisting of a truncated periodic multilayer and a dielectric medium. An infinite periodic multilayer has a well-defined photonic band gap (PBG) and behaves as a perfect mirror, *i.e.* with reflectivity $R = 1$ for all the frequencies and wave vectors located inside the photonic band gap. However, in the same way as defects in an electronic crystal may introduce defect modes, a proper truncation of the multilayer periodicity may introduce photonic states inside the photonic band gap: these modes living both below the light line of the external material and inside the PBG of a 1D photonic crystal are known as Bloch surface waves. They were originally discovered in the late '70s[1, 2, 3], but research on them underwent a relative hiatus until the

'90s[4, 5, 6], when they attracted renewed interest thanks to the development of fabrication techniques that enable the growth periodic multi-layers with tens of periods relatively inexpensively. BSWs have been successfully applied in a variety of situations that require the confinement of light close to the surface of a device, *e.g.* optical surface sensors[7] and control of light emission[8, 9]. The main feature that led researchers to delve into the subject of BSWs is their intense surface field. Indeed, as with surface plasmons, most of the light in a BSW is trapped near the surface of the multilayer. This occurs because such modes exist both below the light line of the external medium and inside the PBG, which means that light is confined by total internal reflection (TIR) on the dielectric side and by the presence of a photonic band gap in the stacking direction[10]. This allows for strongly peaked mode profiles, which is the reason why BSWs have naively been considered "dielectric plasmons". However, unlike plasmons, with proper design of the supporting multilayer both TE (transverse-electric) and TM (transverse-magnetic) polarized BSWs may exist. In addition to this, the decay rate of the Bloch mode in the stacking direction can be changed by piloting the mode inside the photonic band gap, which can be achieved by modifying the truncation layer on the interface with the external dielectric[11]. Altogether, this shrinks the envelope of the mode and reduces the modal volume of BSWs: this is particularly useful with a view to full three-dimensional confinement of the mode, since the field enhancement depends on the ratio between the quality factor of the cavity and the volume of the mode[12].

In spite of all the advances, there still are many open questions that have not allowed a full on-chip integration of Bloch surface waves.
In the first place, surprising though it may sound, the question whether BSWs actually have a strategic advantage - in terms of field enhancement or modal volume - with respect to simpler, fully TIR-based solutions is still unanswered. Most researchers simply take for granted that such an advantage exists, but no proof has ever been published in the scientific literature.
Another open question that has only been partially addressed up to now is how BSWs interact with two-dimensional objects such as gratings, *i.e.* with a one-dimensional refractive index modulation along the direction of propagation, *i.e.* independent of the multilayer supporting the mode itself. This is important by itself, but also with a view to optimizing the coupling scheme, which until now has *mostly* been prism-based.
Moreover, while it is known both theoretically[13] and experimentally[14] that BSWs can be successfully guided using dielectric ridges, *resonators* based on BSWs - another fundamental optical element and building block of a BSW-based photonic circuit - are still being actively researched. The ground seems to be particularly fertile, as a couple of years ago an experimental demonstration of a two-dimensional BSW disk resonator was published[15]. However, with a view to further reducing the modal volume of the BSW, resorting to a ring resonator seems inevitable. Features of BSW ring resonators have been

studied theoretically[16], but a full-fledged experimental observation of their behavior has not been carried out up to now.
Finally, the last point that should be addressed is how full three-dimensional confinement of BSWs could be achieved. Photonic cavities are another fundamental scientific tool, and for at least the last two decades, the scientific community has struggled to develop ultrahigh quality-factor (UHQ) photonic cavities on the scale of the wavelength of light[17, 18, 19, 20, 21]. The applications of such devices are many, and range from strong coupling between light and matter[22, 23, 24] to optical sensing[25], optical switching[26], lasing[27], etc. No such device has ever been demonstrated for BSWs, and thus most of these applications, with the exception of BSW-based sensors[28, 7], are still lacking.

This PhD thesis represents my attempt to answer some of these open questions. It reports a selection of some of the results of my three-year research activity on Bloch surface waves. In chapter 1, I will give a brief presentation of Bloch surface waves by summarising their main features. After this, in chapter 2, I will introduce a general optimization procedure that allows one to understand a priori the minimum modal length and maximum surface electric field achievable with a BSW, given a set of refractive indices[29]. In chapter 3, I will report my results on guided modes supported by a 1D grating built on a 1D truncated periodic multilayer as a function of the geometrical grating parameters. The role of these parameters on the position and width of the PBG will be investigated, together with their influence on the mode dispersion[30]. In chapter 4 the first experimental demonstration of a BSW ring resonator will be reported. This work represents a collaboration with the group of professor S.M.Weiss from Vanderbilt University in Nashville, Tennessee. The material employed for both the multilayer and the ring resonator was porous silicon, which had been chosen for the fine tunability of its refractive index. In chapter 5, a theoretical study of nanobeam cavities based on BSWs is reported. We first developed a general design strategy based on Fourier transforming the profile of the electric field inside the cavity. This allowed us to optimize the cavity parameters and to test the validity of our approximations with FDTD simulations. Finally, in chapter 6 we draw our conclusions.

Contents

Chapter 1

Bloch surface waves

A distributed Bragg reflector (DBR) consists of a long enough repetition of alternating materials with different refractive indices. This periodic variation creates multiple reflections from each layer boundary, which can interfere constructively if the incident wavelength is close to four times the optical thickness of the layer. In this case, the overall reflectance of the structure ideally reaches unity when the number of layers is infinite, and the range of wavelengths this works for is called *photonic band gap* or *photonic stopband*.

However, no such thing as an infinite crystal can exist in physical reality; sooner or later, the repetition of the unit cell would have to be truncated on both sides. An adequate truncation in a photonic crystal, in the same way in which defects in electronic crystals can introduce defect states, may give rise to particular photonic modes called *Bloch surface waves* (BSWs).

As the name suggests, BSWs are propagating modes existing at the interface between a homogeneous medium and a truncated photonic crystal. Light confinement close to the interface is achieved via two different physical mechanisms: the presence of a photonic band gap (PBG) on the multilayer side and total internal reflection (TIR) on the homogeneous side.

They were discovered in the late '70s[2, 31, 1], but interest in propagating surface states was rekindled in the '90s[10, 5, 6]. This revival saw the birth of many diverse applications of Bloch surface waves, from optical sensing[32, 33, 11, 7, 28] to coupling with quantum objects such as quantum dots (QDs)[8].

Moreover, as will be shown in the next chapter, the dispersion of BSWs is rather flexible: by slightly varying the design of the supporting truncated multilayer, the dispersion of the surface mode can be piloted inside the PBG, drastically changing two key figures that characterize guided modes, such as the surface field and the mode volume.

Most of the results that follow will rely on *transfer matrix theory*. The interested reader can find a reasonably light introduction to this technique in Appendix A.

1.1 Bilayer transfer matrix

Consider a truncated periodic multilayer whose unit cell consists of two layers of thicknesses d_1 and d_2 and refractive indices n_1 and n_2.

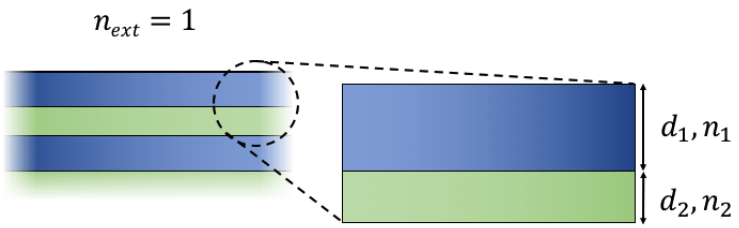

Figure 1.1: Scheme of a multilayer formed by the infinite repetition of a bilayer unit cell. The unit cell has two layers characterized by thicknesses d_1 and d_2 and refractive indices n_1 and n_2.

If we consider the structure to extend indefinitely, we can construct its transfer matrix T, according to the procedure reported in appendix A. The result, reported in eq. (A.51), is

$$M = \begin{pmatrix} e^{i(\phi_1+\phi_2)} + r_{12}r_{21}e^{i(\phi_1-\phi_2)} & r_{21}e^{i(\phi_2-\phi_1)} + r_{12}e^{-i(\phi_1+\phi_2)} \\ r_{12}e^{i(\phi_1+\phi_2)} + r_{21}e^{i(\phi_1-\phi_2)} & r_{12}r_{21}e^{i(\phi_2-\phi_1)} + e^{-i(\phi_1+\phi_2)} \end{pmatrix}, \tag{1.1}$$

where r_{mn} and t_{mn} are the Fresnel reflection and transmission coefficients defined in eq. (A.9) for s-polarization and eq. (A.10) for p-polarization, and ϕ_1 and ϕ_2 are the phases gained by the electric field as it crosses the layer transversally, *i.e.* $\phi_j = e^{w_j d_j}$. w_j, the wave vector component perpendicular to the interfaces of the multilayer in the j-th layer, is defined as

$$w_j = \frac{2\pi n_j}{\lambda_0}\cos\theta, \tag{1.2}$$

for light impinging at an angle θ against the interface.

The photonic band gap for this structure can be found by enforcing the *gap condition* reported in eq. (A.59), which yields

$$2\cos(q\Lambda) = \frac{1}{t_{12}t_{21}}\left[\left(e^{i(\phi_1+\phi_2)} + e^{-i(\phi_1+\phi_2)}\right) + r_{12}r_{21}\left(e^{i(\phi_1-\phi_2)} + e^{-i(\phi_1-\phi_2)}\right)\right]. \tag{1.3}$$

As can be seen, the absolute value of the LHS in eq. (1.3) is less than or equal to 2, whereas the RHS is virtually unbounded. Thus, by sweeping on the parallel component of the propagation wave vector $k_\parallel$ - linked to w_j by the relation $k_\parallel^2 + w_j^2 = (2\pi/\lambda_0)^2$ - we can map out the regions where the equation cannot be satisfied. The result is shown in fig. (1.2) for a specific set of geometrical parameters.

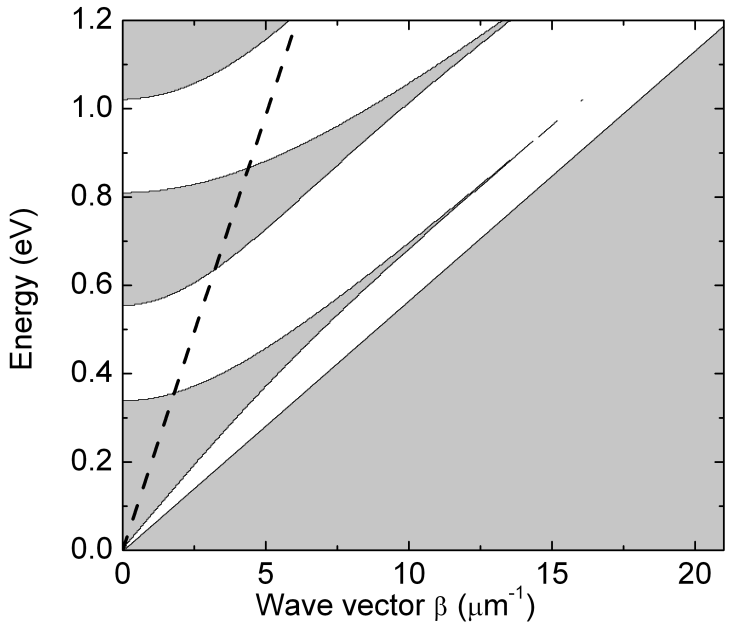

Figure 1.2: Energy-wave vector diagram for a SiO_2-Si unit cell formed by $d_1 = 260$ nm, $n_1 = 3.48$, $d_2 = 320$ nm, $n_2 = 1.44$. The photonic band gap is shown in white. The light line for the external medium (air) is dashed.

As can be seen from this diagram, the structure supports no gap modes. However, one may consider a slightly different unit cell such as the one shown in fig. 1.3.

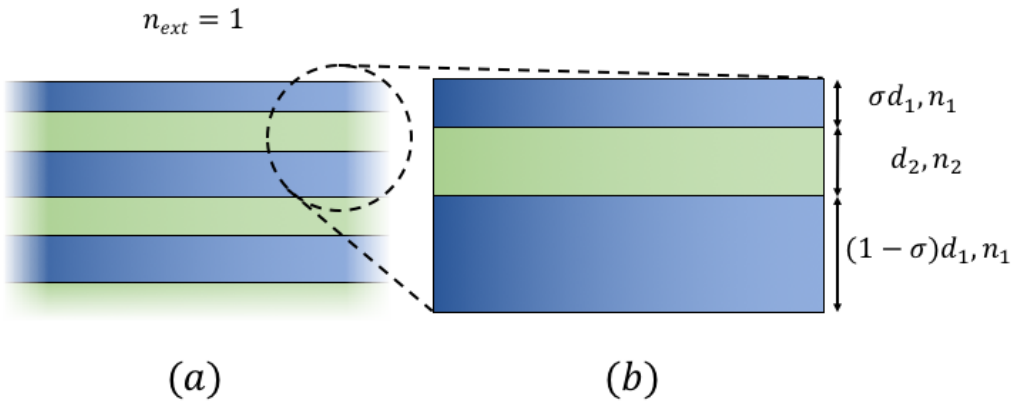

Figure 1.3: Truncated version of fig. 1.1: the first layer in the multilayer is now shrunk to a thickness $d_{1st} = \sigma d_1$, where $0 < \sigma < 1$ is given by eq. (A.132).

In this case, the unit cell is a *shifted* version of the former one, where the first layer has thickness σd_1, with a truncation factor $0 < \sigma < 1$ given by

equation (1.4)[1], *i.e.*

$$\sigma = \frac{i}{2w_1 d_1} \ln\left(\frac{(M_{11} - e^{iKL})(iw_1 + q_e)}{(q_e - iw_1)M_{12}}\right), \tag{1.4}$$

and the last layer has thickness $(1-\sigma)d_1$. It may be useful to remark that such a structure would have the same bulk properties as the one shown in fig. 1.1, since the two adjacent σd_1 and $(1-\sigma)d_1$ layers would sum to form the former thickness d_1. This means, in particular, that the photonic band gap, which is a bulk property, would not change[11]. We can then look for photonic modes supported by the structure by looking for poles of the reflectance.

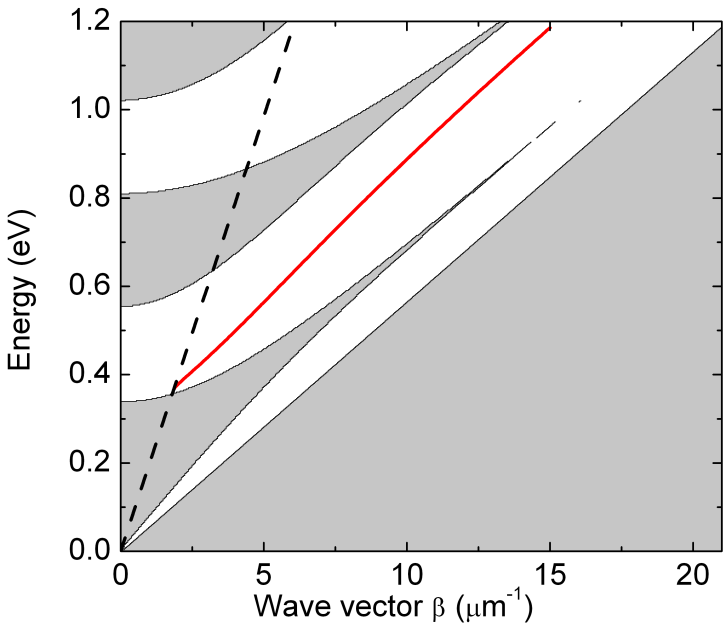

Figure 1.4: Energy-wave vector diagram for a semi-infinite SiO_2-Si 1D PhC whose unit cell is formed by $d_1 = 260$ nm, $n_1 = 3.48$, $d_2 = 320$ nm, $n_2 = 1.44$. The first layer is truncated to a length σd_1, with the truncation factor σ given by eq. (1.4). The photonic band gap is shown in white, the light line for the external medium (air) is dashed and the BSW is in solid red.

As can be seen from picture 1.4, the PBG is not changed by the shift in the unit cell (as can be checked against fig. 1.2); however, the presence of the first, truncated layer gives rise to a defect mode, shown in solid red. This mode lives inside the band gap (shown in white in fig. 1.4); this means that the electric field decays in the stacking direction, as implied by Bloch's theorem for a Bloch wave vector of non-zero imaginary part (see eq.A.60). Moreover, the mode lives below the light line of the external medium; this implies that the mode will be confined by TIR on the opposite interface. Altogether, the mode

[1]The full derivation of the truncation factor is given in the Appendices, eq. (A.132)

cannot propagate in the z direction and is thus localized in the proximity of the surface of the structure. This mode is called *Bloch surface wave*, and its electric field profile is shown in fig. 1.5.

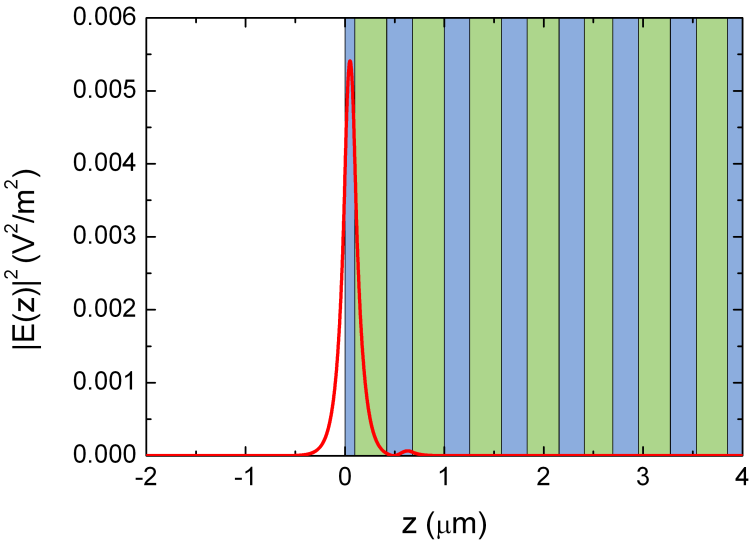

Figure 1.5: Field profile of the Bloch surface wave shown in fig. 1.4 for $E = 0.8$ eV.

The Bloch wave vector inside the photonic band gap has a non-zero imaginary part which entails the exponential decay of the field in the stacking direction. The value of the imaginary part $q = \Im[k_{Bloch}]$ changes as the parallel component of the propagation wave vector $k_{\|}$ varies inside the band gap according to eq. (A.60), *i.e.*

$$2\cos(k_{Bloch}\Lambda) = \frac{1}{t_{12}t_{21}}\left[\left(e^{i(\phi_1+\phi_2)}+e^{-i(\phi_1+\phi_2)}\right)+r_{12}r_{21}\left(e^{i(\phi_1-\phi_2)}+e^{-i(\phi_1-\phi_2)}\right)\right]. \tag{1.5}$$

Inverting this equation yields

$$q = \frac{1}{\Lambda}\ln\frac{Tr(M)\pm\sqrt{\Delta}}{4}, \tag{1.6}$$

where the sign inside the logarithm is to be chosen to enforce exponential decay in the stacking direction, as explained in section A.3. The typical behavior of q is shown in fig. 1.6 for a Si/SiO_2 multilayer of thicknesses $d_{Si} = 260$ nm and $d_{SiO_2} = 320$ nm, at a wavelength $\lambda_0 = 1.55$ μm ($E = 0.8$ eV).

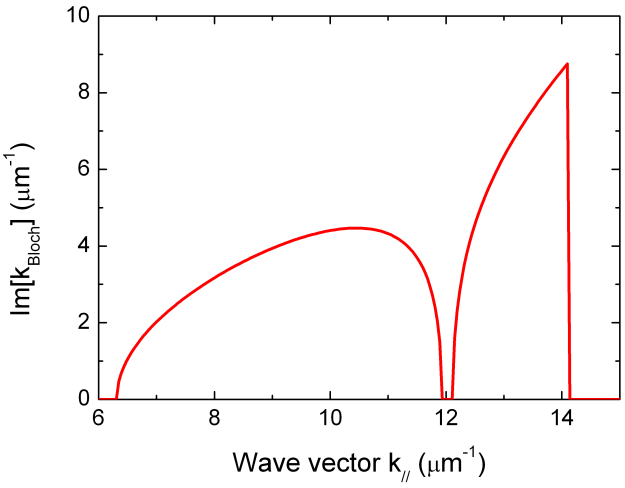

Figure 1.6: Imaginary part of the Bloch wave vector inside a photonic band gap for a typical Si/SiO_2 multilayer.

As the energy increases, the photonic band gap broadens, together with the variability range of the Bloch wave vector. In fig. 1.7, a contour plot of the imaginary part of the Bloch wave vector is shown in the energy range [0; 1.2 eV] for the same multilayer employed in fig. 1.6.

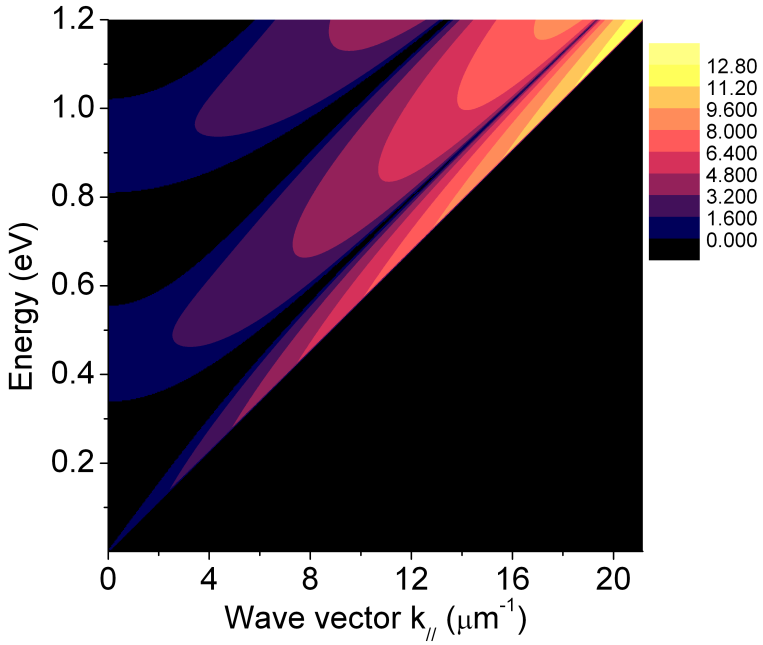

Figure 1.7: Contour plot of the imaginary part of the Bloch wave vector inside a photonic band gap for a typical Si/SiO_2 multilayer.

The position of the Bloch surface wave inside the photonic band gap can be

piloted by slightly modifying the truncation factor σ. In the following pictures two cases are reported for the usual Si/SiO_2 structure relative to $\sigma_1 = 0.192$ and $\sigma_2 = 0.423$.

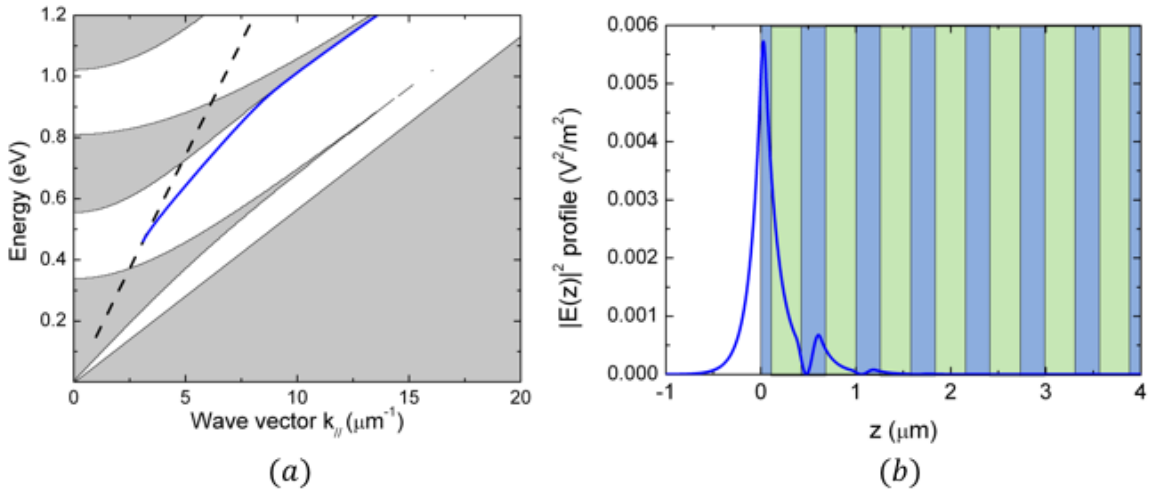

Figure 1.8: Bloch surface wave supported by a 9-layer Si/SiO_2 multilayer with $d_{Si} = 260$ nm, $d_{SiO_2} = 320$ nm, $\sigma \approx 0.192$ ($d_{1st} = 50$ nm), $n_{Si} = 3.48$, $n_{SiO_2} = 1.44$. The external medium on both sides of the structure was chosen to be water ($n_{ext} = 1.33$). Mode dispersion (a) and square modulus of the electric field mode profile (b) at $E = 0.8$ eV.

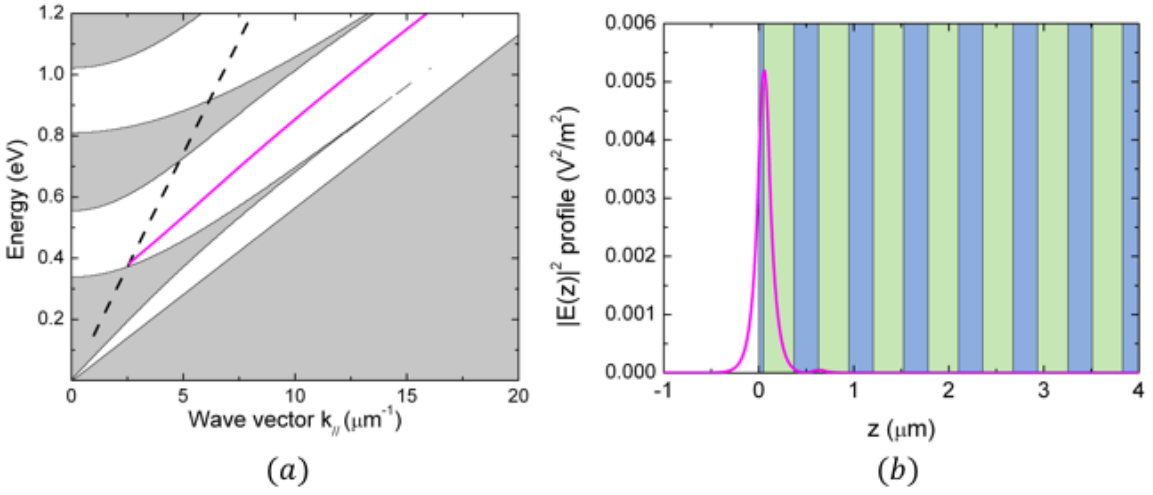

Figure 1.9: Bloch surface wave supported by a 9-layer Si/SiO_2 multilayer with $d_{Si} = 260$ nm, $d_{SiO_2} = 320$ nm, $\sigma \approx 0.423$ ($d_{1st} = 110$ nm), $n_{Si} = 3.48$, $n_{SiO_2} = 1.44$. The external medium on both sides of the structure was chosen to be water ($n_{ext} = 1.33$). Mode dispersion (a) and square modulus of the electric field mode profile (b) at $E = 0.8$ eV.

1.2 Light-coupling for Bloch surface waves

As was explained in section 1.1, Bloch surface waves exist below the light line of the external material and within one of the photonic band gaps induced by a truncated one-dimensional photonic crystal. This is due to the fact that the confinement of light along the stacking direction of the multilayer occurs via total internal reflection on the dielectric side and via the presence of a photonic band gap on the multilayered side, respectively[1]. Each such mode is represented by a pole in either the overall reflectance (or transmittance), as shown in eq. A.48, and it has an associated parallel component of the wave vector $\beta = k_{\parallel}$ greater than that of photons propagating freely in the external material ($k = \omega n_{ext}/c$), as demonstrated by the fact that the amplitude of the field decays within these regions. By definition, this entails that light from some external source cannot typically be coupled into a BSW as it is; either a glass prism or a grating coupler will be necessary to match the propagation constant of the incoming wave to that of the Bloch surface wave. This is typically achieved via a glass prism or a grating coupler.

Prisms are typically all dielectric devices placed on top of the multilayer in the so-called *Kretschmann configuration*[34]. This technique was developed in 1968 and became the main coupling scheme for surface plasmon polaritons. In the original SPP version, it involves depositing a nano-dimensional metallic layer on top of the prism surface. Total internal reflection of light causes evanescent fields to appear and pass through the thin metal film and to excite a surface plasmon on its opposite surface. In the case of Bloch surface waves, no metals are involved, and the prism is placed on the bottom surface of the multilayer; even in this case, phase matching between the incident wave vector and the pole in the reflectance, ultimately allowing light to be plugged into the BSW, is achieved via evanescent coupling.

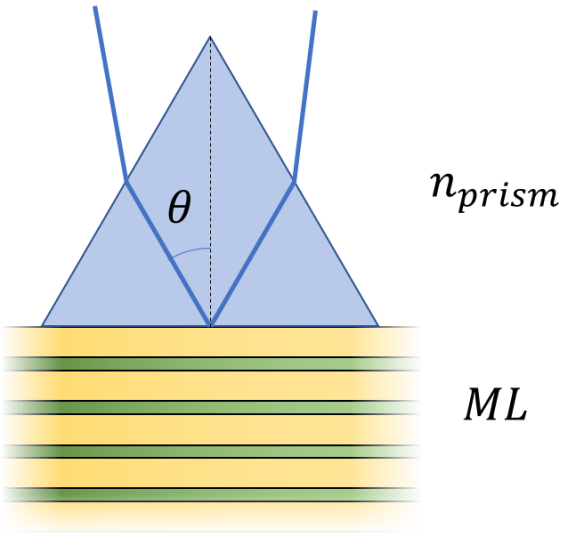

Figure 1.10: A multilayer topped by a coupling prism in the Kretschmann configuration.

Another coupling scheme involves grating couplers, *i.e.* a periodic corrugation placed on top of a multilayer to enforce phase matching conditions between incoming light and the proper BSW.

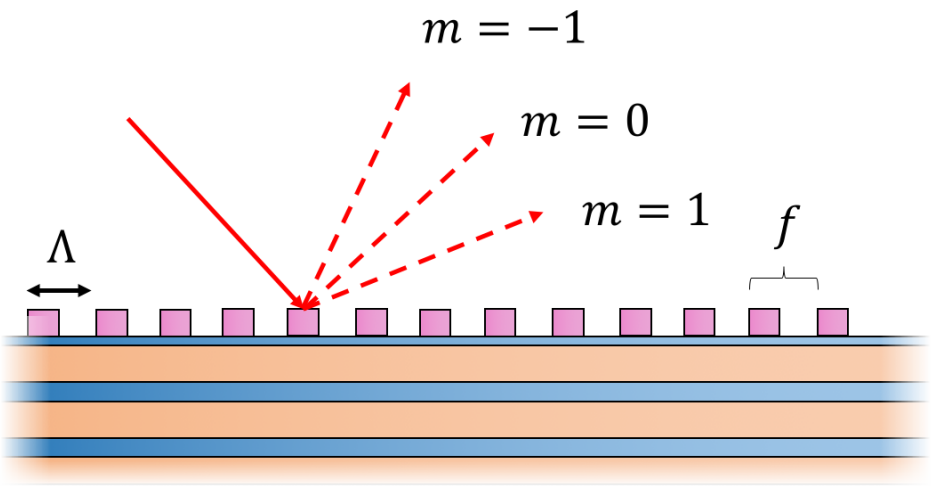

Figure 1.11: A periodic grating placed on top of a truncated periodic multilayer. The grating is characterized by a period Λ and a filling fraction f.

Incident radiation impinging on the coupler at an angle θ with respect to the normal will be characterized by a wave vector $k_{inc} = n_{ext}k_0$, where $k_0 = 2\pi/\lambda_0$. Light can then be scattered from the grating, and its wave vector is changed by integer multiples of the grating wave vector $k_G = 2\pi/\Lambda$, Λ being the grating period. The actual integer $m \in \mathbb{Z}$ represents the *order* of diffraction. A diffracted order having a wave vector greater than that of photons moving freely in a medium of refractive index n_j, *i.e.* $k > k_j = k_0 n_j = 2\pi n_j/\lambda_0$ becomes evanescent. Then, when a phase matching condition is met between the diffracted order and the parallel wave vector component of a BSW supported by the underlying multilayer, *i.e.*

$$\frac{2\pi n_{ext}}{\lambda_0}\cos(\theta) + mk_G = k_{BSW}, \tag{1.7}$$

light is coupled selectively into the Bloch surface wave having a parallel wave vector component k_{BSW}.

Thus, both coupling techniques rely on the evanescent coupling of light. Grating couplers have the considerable pro of being *mode selective*, since, as shown in eq. (1.7), the grating can be designed so that the phase-matching condition is met just for a single mode. However, this selectivity comes at a price, specifically the experimental disadvantage of fabricating a grating with stringent optical tolerance.

Another coupling technique which was not taken into account in this thesis is that of *edge/butt coupling*, in which light from an optical fiber is coupled to a multilayer by holding the fiber facet against the cleaved side of a truncated periodic multilayer. This technique can typically show high efficiency, which is however counterweighted by the need for cleaving a facet of the multilayer, which may still be a technical issue, and the lack of selectivity, as a variety of modes can be coupled at the same time.

Chapter 2

Optimization of Bloch surface waves

2.1 Motivation

Bloch surface waves have always garnered interest because of the intrinsically intense electric fields which characterize these modes. Indeed, BSWs found application in a variety of scenarios whose common feature was the enhancement of the interaction between light and matter near the surface of the structure, such as control of light emission[35, 36, 37] or optical sensing[38, 39, 14, 32, 33]. Some examples of this interest can be gathered from recent papers, *e.g.*

1. "*Another favorable property of PCs is the possibility of large enhancements of local fields with BSW.*"[40]

2. "*Because the maximum intensity associated with the BSW can be engineered to be at the surface, it is particularly attractive for biosensing using the large field enhancements.*"[41]

3. "*This large field enhancement can be used for improving the sensitivity of sensors, fluorescence emission enhancement and enhancement of the Goos–Hänchen effect.*"[42]

It may therefore seem striking that their most renowned feature - the intense surface field - has never been demonstrated, and that many authors take this strategic advantage as given without inquiring whether simpler solutions based on total internal reflection, *e.g.* guided modes in dielectric slab waveguides, have similar performances.

It appears that this problem might be due to the confusion between the field enhancement, which depends by definition on the physical volume in which light confinement takes place, and the amount of energy that can be stored at the surface of the structure due to the external excitation of the guided mode. In a 1982 paper[43], Sipe *et al.* showed that, assuming a monochromatic plane

wave impinging on a dielectric planar waveguide, the amount of energy that it is possible to store in the photonic mode - and thus the electric field at the surface of the structure itself - increases with the distance between the structure and the prism which evanescently couples light inside the slab. Thus, as a consequence of using plane waves in the theoretical derivation, the field increases as the coupling strength decreases[43, 44], and in principle any value of the electric field at the surface can be achieved by fine tuning the coupling distance, regardless of the actual electric field distribution of the mode or the input pump power. It is clear that, in this scenario, relying on the electric field at the surface as a figure of merit to compare different structures would leave a flank exposed to arbitrariness.

Thus, we are still faced with the question whether Bloch surface waves are so special and deserve the extra complications they entail with respect to simpler alternatives, such as regular asymmetric slabs.

Luckily, it is still possible to devise an objective procedure that allows one to compare the surface fields supported by different structure in terms of their electric field enhancements, which are *intrinsic* properties of the modes. In this chapter we will present a systematic comparison between TE-polarized Bloch surface waves propagating on a truncated periodic multilayer and guided modes supported by an asymmetric slab waveguide. The results presented in this chapter were published in [29]. The focus will be on TE-polarized BSWs for at least two reasons: firstly, as shown in Appendix A (fig. A.7), the PBG for TM-polarized modes closes and thus the range of existence of a Bloch surface wave is limited; furthermore, if one is interested in TM-polarized modes, then resorting to the electric field enhancement brought about by surface plasmons can be exploited. With this in mind, it makes more sense to look for a solution in the TE-polarization scenario.

2.2 Structural parameters

To start our analysis, consider the two planar dielectric structures shown in fig. 2.1.

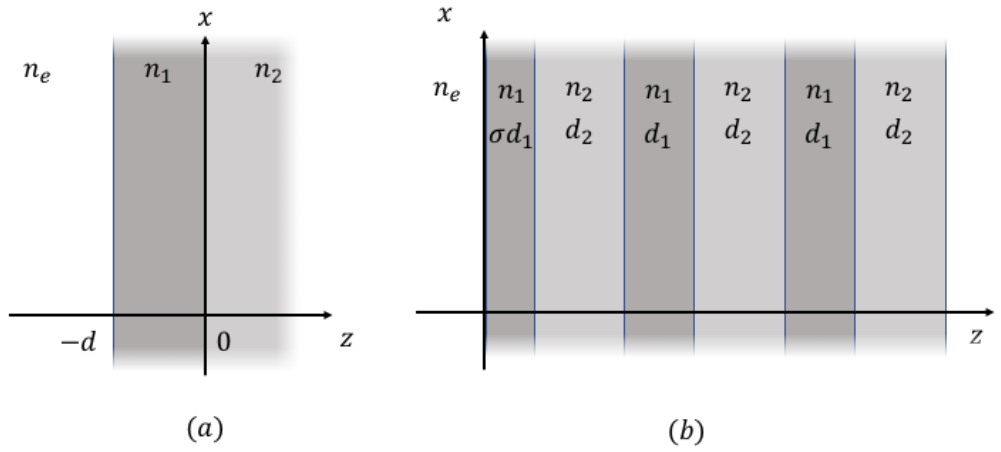

Figure 2.1: The structures we want to compare: (a) an asymmetric slab waveguide and (b) a truncated periodic multilayer.

They consist of an asymmetric dielectric slab waveguide and a truncated periodic multilayer. The slab has core thickness d and real refractive index $n_1 = n_2 + \Delta n$. On either side, the core layer is bounded by a semi-infinite layer having refractive index n_2 on the side of the substrate and $n_{ext} = 1$ on the external one. We chose to neglect symmetrical structure, *e.g.* membranes, because in typical experimental conditions solid substrates are extremely useful to facilitate the manipulation and movement of the waveguides.

The unit cell of the periodic multilayer consists of three layers layers having refractive indices $n_1 = n_2 + \Delta n$, n_2 and n_1 again; their thicknesses are σd_1, d_2 and $(1 - \sigma)d_1$. The multilayer is semi-infinite, truncated by air on only one side, and the truncation factor satisfies the inequality $0 < \sigma < 1$. This choice for the unit cell is justified in chapter 1.1. Some technical details on how to calculate the modes supported by a semi-infinite one-dimensional photonic crystal are reported in appendix D.

In the case of the dielectric slab waveguide, the confinement of light is due only to total internal reflection; because of this, the effective index of the mode[1] satisfies the inequality

$$n_2 < n_{eff} < n_1. \tag{2.1}$$

On the other hand, light confinement in the multilayer occurs due to TIR on the external side and to the presence of a PBG in the stacking direction. In principle, light could be confined in this direction also by TIR, but we restricted our analysis to the case where $1 < n_{BSW} < n$, *i.e.* above the light line of the lighter dielectric material.

[1]The effective index of the mode is linked to the parallel component of the propagation wave vector β by the following definition: $\beta = 2\pi n_{eff}/\lambda_0$.

2.3 Figures of merit

Our analysis started from two questions:

1. Which structure performs best in terms of electromagnetic energy density at a point at random along the stacking direction?

2. Which structure maximizes the electric field on the interface between the structure and the external medium?

To try and answer these two questions, we exploited two figures of merit (FoMs). The first one is the *modal length*, which was borrowed from the modal volume used in the field of three-dimensional resonators[45]. In our one-dimensional case, the modal length is defined as

$$L_{mod} = \frac{1}{\max\limits_{z}[\varepsilon(z)|E(z)|^2]} \int_{-\infty}^{+\infty} \varepsilon(z)|E(z)|^2 dz, \tag{2.2}$$

where $\varepsilon(z) = \varepsilon_0 n^2(z)$ is the dielectric function in the stacking direction and $\varepsilon_0 = 8.854187817\cdots \times 10^{-12}$ F/m is the vacuum permittivity. $E(z)$ is the electric field profile in the stacking direction. According to eq. (2.2), for a properly normalized mode the definition becomes

$$L_{mod} = \frac{1}{\max\limits_{z}[\varepsilon(z)|E(z)|^2]} \frac{\hbar\omega}{2}, \tag{2.3}$$

and thus maximizing the electromagnetic energy density amounts to minimizing the modal length.

The second figure of merit is the value of the electric field on the surface of the structure, close to the external dielectric, *i.e.* $E(0)$. To avoid incurring in the issue presented at the beginning of this chapter, the one-dimensional mode profile $E(z)$ must be properly normalized. According to the procedure reported in appendix A.6, the modes are normalized according to this condition:

$$S \int_{-\infty}^{+\infty} \varepsilon(z)|E(z)|^2 dz = \frac{\hbar\omega}{2}, \tag{2.4}$$

where $E(z)$ is the electric field profile in the stacking direction, $\omega = \frac{2\pi c}{\lambda_0}$ is the (angular) frequency of the field and $\varepsilon(z)$ is the dielectric function profile of the structure under scrutiny. S is a normalization surface in the transverse direction, *i.e.* the plane of the structure, which we set equal to 1 m^2. We further assumed no chromatic dispersion for all the media around the wavelength of interest λ_0. It is important to notice that when the field is normalized as in eq. (2.4), then energy-independent calculations can be produced by resorting to scale-invariant figures such as L_{mod}/λ_0 and $E(0)\lambda_0$. To this aim, the figures

of merit we employed were

$$FoM_1 = \frac{L_{mod}}{\lambda_0} = \frac{1}{\lambda_0 \max_z[\varepsilon(z)|E(z)|^2]} \frac{\hbar\omega}{2}, \tag{2.5}$$

$$FoM_2 = |E(0)|\lambda_0. \tag{2.6}$$

Before closing this section we feel it appropriate to remark that our choice for the figures of merit is not the only one, and that other authors have investigated different possible strategies. Among them, the minimization of the limit of detection (LoD), defined as the minimum variation in some parameter that can still be resolved by a sensor, is the most common one. The LoD depends on the sensitivity of the sensor and the width and depth of the resonance dips it relies on[46]. Such an approach for BSWs would not be unfruitful, as BSW-based sensors typically feature larger sensitivities than SPR-based systems involving metallic media[47]. Thus, this chapter represents only a fraction of the whole issue of the optimization of Bloch surface waves, and it leaves room for further improvements in such a diverse field.

2.4 Theoretical procedure

For each pair of refractive indices in the range $n_1 \in [1.4;\ 4.1]$ and $n_2 \in [1.4;\ 2.1]$, our goal was to find out which structure - either the asymmetric slab waveguide or the truncated periodic multilayer - managed to maximize the field confinement via the scaled modal length L_{mod}/λ_0 or to maximize the scaled surface field $E(0)\lambda_0$. The procedure differed according to the type of structure.

For the asymmetric slab waveguides, we employed the semi-analytical approach sketched in appendix B. For each set of refractive indices n_1 and n_2, we considered a sweep on the scaled core thickness between

$$\frac{d_{min}}{\lambda_0} = \frac{1}{2.0\pi\sqrt{n_1^2 - n_2^2}}(m\pi + \arctan\left(\sqrt{\frac{n_{sub}^2 - n_{ext}^2}{n_{core}^2 - n_{sub}^2}}\right) \tag{2.7}$$

$$\frac{d_{max}}{\lambda_0} = \frac{1}{2.0\pi\sqrt{n_1^2 - n_2^2}}((m+1)\pi + \arctan\left(\sqrt{\frac{n_{sub}^2 - n_{ext}^2}{n_{core}^2 - n_{sub}^2}}\right), \tag{2.8}$$

where $m = 0$ is a mode-count index[48]. The equations were found by inverting the mode dispersion relation, *i.e.*

$$\tan(hd) = \left(\frac{h(q+p)}{h^2 - qp}\right), \tag{2.9}$$

as shown in appendix B.19, and then substituting the definitions of the wave vector components in each layer, as given by eq. (B.5-B.7). The scaled core length is the only independent geometric parameter in this case, and both

figures of merit can be expressed a functions of d/λ_0; therefore, the parameter space can be searched for the structure with the highest FoMs among *all* the possible asymmetric slab waveguides of the form shown in figure 2.1.

This is not the case with a truncated 1D photonic crystal, which depends on more structural parameters, namely the refractive indices of both layers in the unit cell, n_1 and n_2, their thicknesses d_1 and d_2, and the truncation factor σ. Thus, in this case we endeavored to reduce the dimensionality of the parameter space by choosing specific layer thicknesses in such a way as to guarantee the fastest decay of the electric field in the multilayer. This occurs when the so-called generalized quarter-wavelength condition is satisfied, *i.e.* when the thicknesses are

$$d_1 = \frac{\lambda_0}{4\sqrt{n_1^2 - n_{BSW}^2}} \tag{2.10}$$

$$d_2 = \frac{\lambda_0}{4\sqrt{n_2^2 - n_{BSW}^2}}, \tag{2.11}$$

where n_{BSW} is the effective index of the BSW, linked to the propagation wave vector by $\beta_{BSW} = 2\pi n_{BSW}/\lambda_0$. With this new hypothesis, for each pair of refractive indices $(n_1; n_2)$ in the unit cell, we considered all possible values of the effective index $n_{BSW} \in [1;\ n_2]$, and for each of these we calculated the corresponding truncation factor σ according to the matricial procedure reported in appendix A.8, *i.e*

$$\sigma = \frac{i}{2w_1 d_1} \ln\left(\frac{(M_{11} - e^{ik_{Bloch}\Lambda})(iw_1 + q_e)}{(q_e - iw_1)M_{12}}\right). \tag{2.12}$$

An explanation for all the physical quantities appearing in this equation is presented in appendix A. Briefly, M_{11} and M_{12} are elements of the transfer matrix for the structure under consideration; k_{Bloch} is the Bloch wave vector proceeding from the multilayer structure of period $\Lambda = d_1 + d_2$; w_1 is the perpendicular component of the propagation wave vector of light in the first layer, and q_e is the imaginary part of the propagation wave vector of light in the external medium.

Conditions (2.10, 2.11) seem reasonable, as they maximize the field decay in the stacking direction of the multilayer. However, assuming these generalized quarter-wavelength conditions is no guarantee that our numerical procedure will lead to the best structures, *i.e.* those maximizing the two FoMs in eq. (2.6, 2.5). In fact, we verified via a more time-consuming brute-force approach that these assumptions are reasonable: after fixing the refractive indices (n_1, n_2) around some value of interest, we verified that the structural parameters maximizing our FoMs were either equal to or not considerably different from those obtained by assuming conditions (2.10, 2.11).

2.5 Results and discussion

The goal of our analysis was to find the structural parameters of both asymmetrical slab waveguide and truncated periodic multilayer that maximize the field confinement, *i.e.* minimize the wavelength-scaled modal length L_{mod}/λ_0, and/or maximize the surface field $|E(0)|\lambda_0$. This research was carried out for each pair of refractive indexes (n_1, n_2), where $n_2 \in [1.4, 2.1]$ and $n_1 = n_2 + \Delta n$, with $\Delta n \in [0, 2.0]$.

2.5.1 Modal volume

In figures 2.2b and 2.3c-d we plotted the thickness of the core layer of an asymmetric slab and the thicknesses of the low-index and high-index layer of a truncated 1D photonic crystal, respectively, corresponding to the structures that minimize the mode length of a Bloch surface wave.

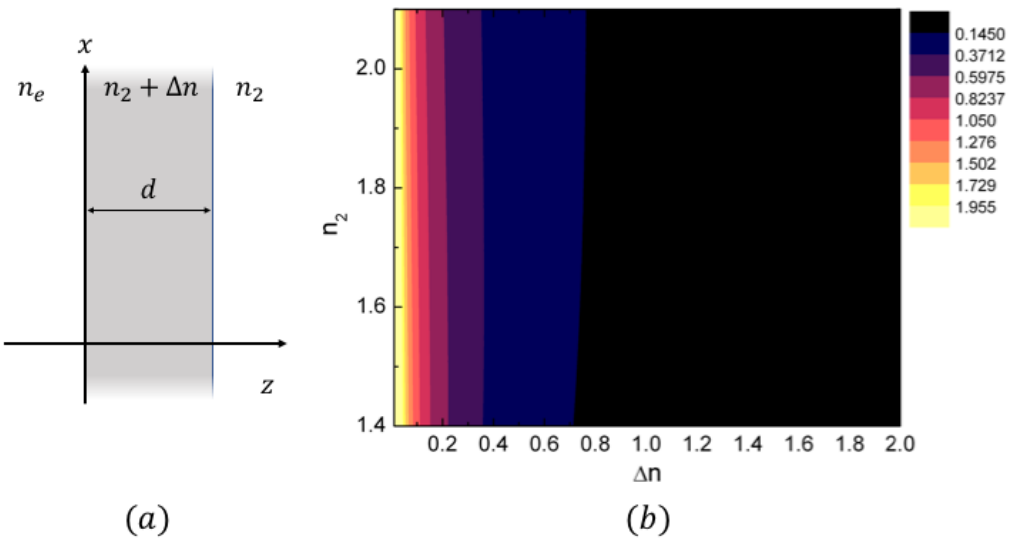

Figure 2.2: (a) The structure that is being optimized: an asymmetric slab waveguide of core thickness d and core refractive index $n_2 + \Delta n$, surrounded by two semi-infinite media of refractive indices $n_e = 1.0$ and n_2. (b) Contour plot of the core thickness d of an asymmetrical slab waveguide corresponding to the minimum wavelength-scaled mode length L_{mod}/λ_0.

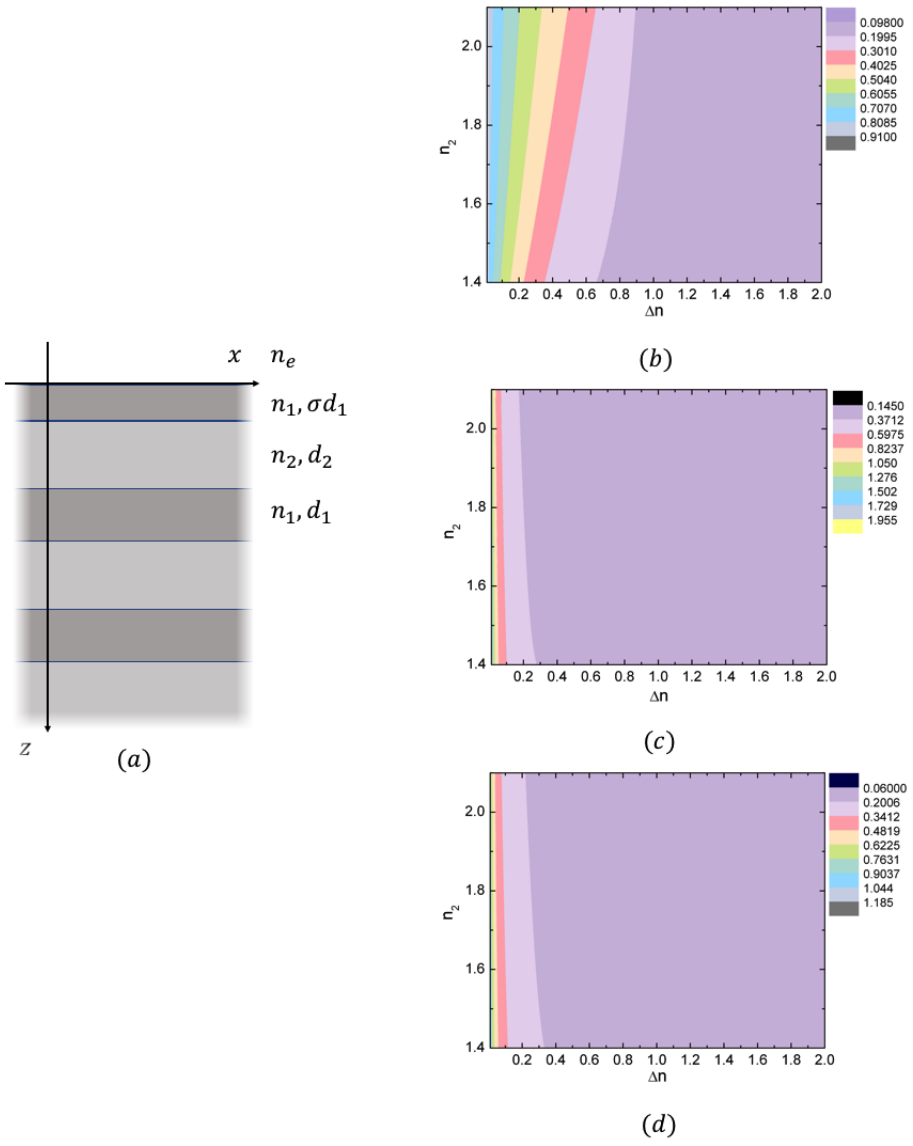

Figure 2.3: (a) Sketch of the multilayer structure under scrutiny; (b) Contour plot of the truncation factor σ that yields the minimum wavelength-scaled mode length L_{mod}/λ_0; (c) Contour plot of the low-index layer thickness d_2 that yields the minimum wavelength-scaled mode length L_{mod}/λ_0; (d) Contour plot of the high-index layer thickness d_1 that corresponds to the minimum wavelength-scaled mode length L_{mod}/λ_0.

The plot shows a non-trivial behavior, except for the divergence of the layer thickness with decreasing refractive-index contrast (RIC) Δn. With these geometrical parameters, the figures of merit given in eq. (2.5) and (2.5) can be evaluated.

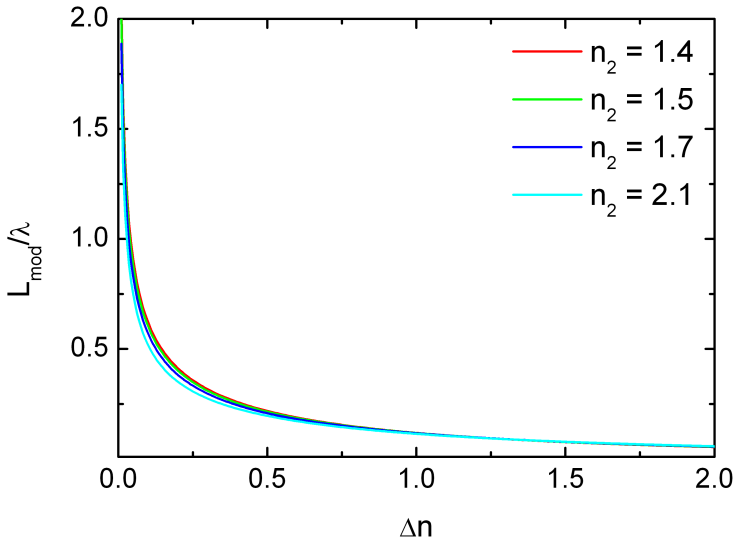

Figure 2.4: Wavelength-scaled modal length of the TE0 mode supported by an asymmetrical slab waveguide as a function of the refractive-index contrast $\Delta n = n_1 - n_2$. The refractive index of the substrate n_2 takes 4 selected values reported in the legend.

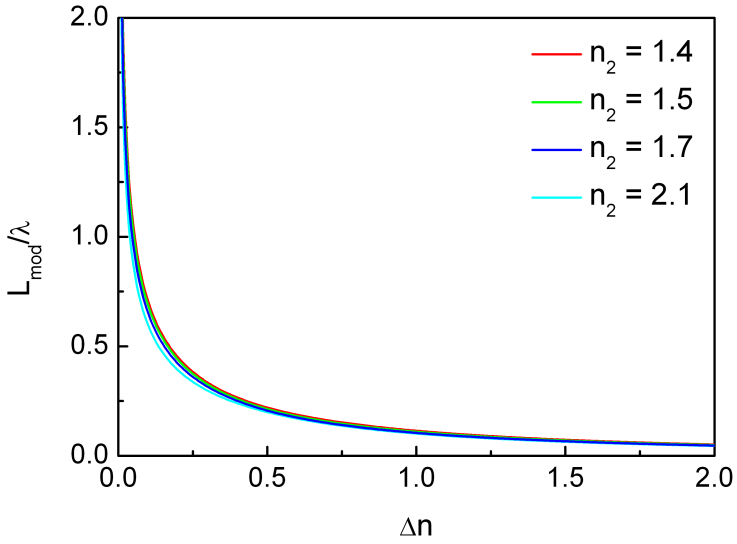

Figure 2.5: Wavelength-scaled modal length of the Bloch surface wave supported by a truncated periodic multilayer as a function of the refractive-index contrast $\Delta n = n_1 - n_2$. The lower refractive index n_2 takes 4 selected values reported in the legend.

In figures 2.4 we plot the smallest wavelength-scaled modal length L_{mod}/λ_0

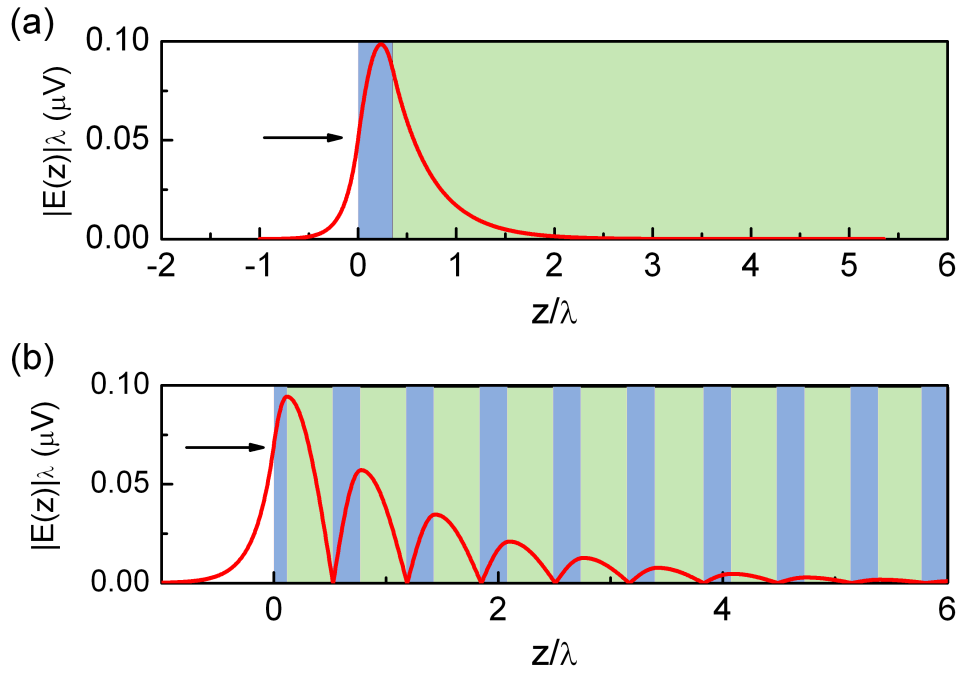

Figure 2.6: Wavelength-scaled moduli of the electric fields of (a) the TE0 mode supported by an asymmetric slab waveguide of core index $n_1 = 1.7$, cladding index $n_2 = 1.5$ and core thickness $d = 0.354\lambda_0$;

for a the fundamental TE mode supported by an asymmetric slab waveguide in terms of the refractive-index contrast $\Delta n = n_1 - n_2$; likewise, in figure 2.5 we plot the same physical quantity relative to a Bloch surface wave supported by a truncated periodic multilayer. We can immediately recognize that in both structures the wavelength-scaled modal length is essentially independent of the lower refractive index n_2; on the other hand, it is characterized by a strong dependence on the refractive index contrast Δn. Moreover, for a given RIC Δn, the best TE0 mode - confined by total internal reflection - and the Bloch surface wave - mainly confined by the presence of a photonic band gap - appear to have similar mode lengths.

Another important remark can be made by looking at the mode profile of the electric field corresponding to the points starred in figures (2.4) and (2.5).

From these pictures, it is clear that the maximum $\varepsilon(z)|E(z)|^2$ of the TE0 mode in the best asymmetric slab is extremely close to that of a BSW in a truncated periodic multilayer. However, from picture 2.6 it is also clear that the BSW extends much deeper into the multilayer with respect to the TE0 mode. This may seem paradoxical, since the modal length L_{mod} is usually associated to how *tightly* the field is confined. However, if one is interested in measuring how tightly a mode is confined, then one must resort to the usual statistical concepts of barycenter ($< z >$) and variance (σ^2_{mode}) of the mode

distribution, defined as

$$< z > = \frac{\int_{-\infty}^{+\infty} z\varepsilon(z)|E(z)|^2 dz}{\int_{-\infty}^{+\infty} \varepsilon(z)|E(z)|^2 dz}, \tag{2.13}$$

$$\sigma^2_{mode} = \frac{\int_{-\infty}^{+\infty} (< z > -z)^2 \varepsilon(z)|E(z)|^2 dz}{\int_{-\infty}^{+\infty} \varepsilon(z)|E(z)|^2 dz}. \tag{2.14}$$

Furthermore, another explanation could be that the Bloch surface wave oscillates in the multilayer, and thus the contributions to the modal length coming from the layers are modulated, whereas a TIR-guided mode undergoes simple exponential decay without oscillatory behavior.

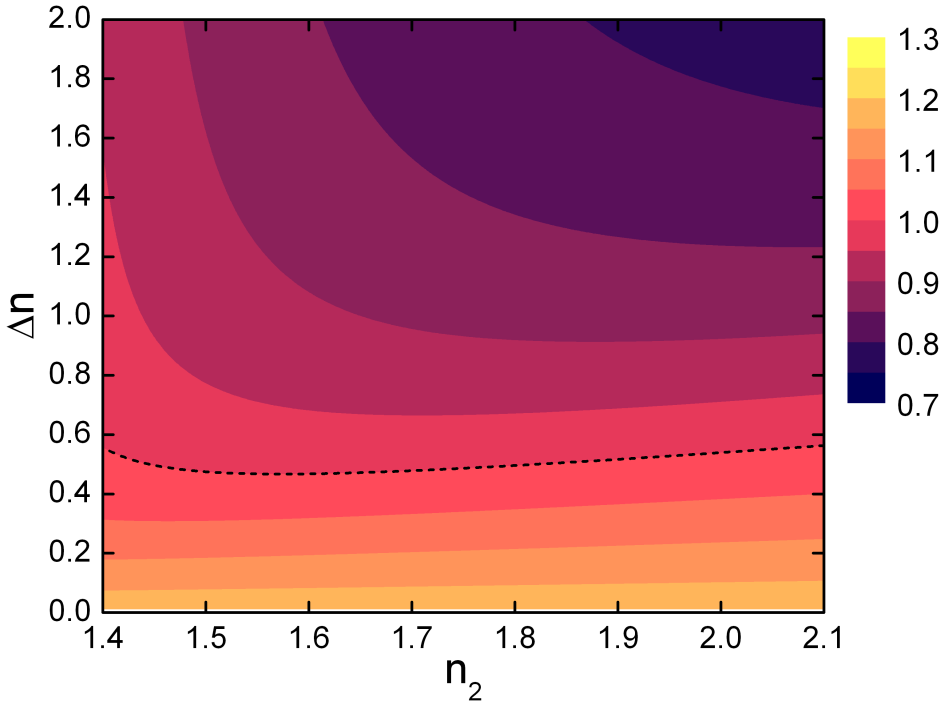

Figure 2.7: Contour plot showing the ratio between the best mode length of a BSW supported by an optimized truncated periodic multilayer and the best mode length of the TE0 mode supported by an optimized asymmetrical slab waveguide as a function of the lower refractive index n_2 and the refractive index contrast Δn. The star corresponds to the structural parameters used in fig. 2.6.

In figure 2.7 we plotted the ratio of the modal lengths of the Bloch surface wave and the TE0 mode as a function of both the lower refractive index and the refractive index contrast. The contour plot confirms the slight dependence of the mode length on the lower refractive index n_2, which had already been pointed out in fig. 2.4 and fig. 2.5. However, in addition to this, the plot also shows further features. Firstly, the plot can be ideally divided in three regions:

- In the region $\Delta n > 0.6$, the ratio goes below unity: this means that the modal length of the TE0 mode is greater than that of the BSW, and this implies in turn that the largest electromagnetic density in a generic point is achieved in a truncated periodic multilayer. This behavior becomes more pronounced with increasing refractive index contrast.

- For small refractive index contrasts, *i.e.* the region where $\Delta n < 0.5$, the ratio is greater than unity, which means that the largest electromagnetic energy density in a generic point is achieved with an asymmetric slab waveguide. This behavior increases as the refractive index contrast decreases.

- In the intermediate region, *i.e.* where $0.5 < \Delta n < 0.6$, the ratio is close to unity, and the two structures substantially behave in the same way. This means that it is always possible to find an optimized asymmetric slab that has similar performance to that of a truncated periodic multilayer.

In all our analysis, we always took the external medium to be air ($n_e = 1.0$). However, we do not believe this to be a limitation, and we expect that changing the refractive index of the upper cladding would lead to similar results.

2.5.2 Surface field

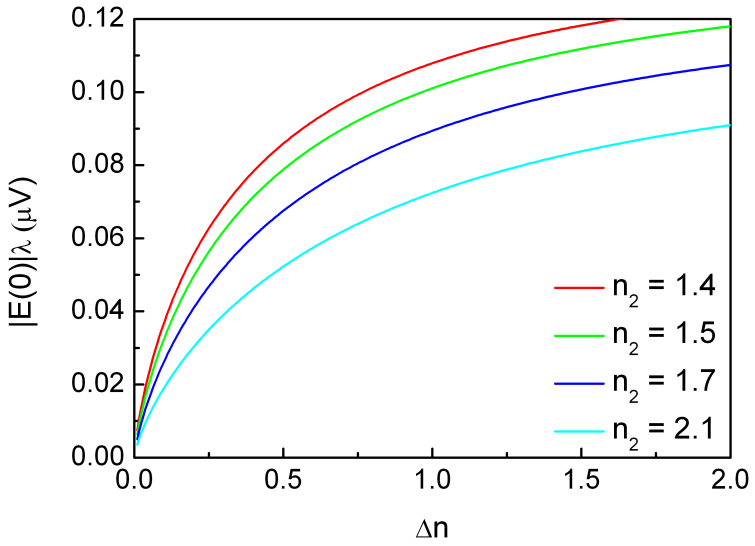

Figure 2.8: Plot of the highest value of the wavelength-scaled surface field $|E(0)|\lambda_0$ that can be achieved by the TE0 mode in an asymmetric slab waveguide as a function of the refractive index contrast between core and substrate.

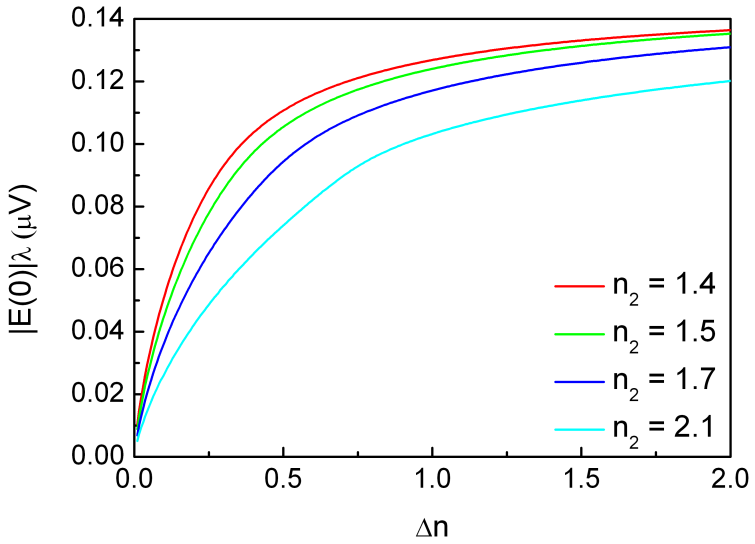

Figure 2.9: Plot of the highest value of the wavelength-scaled surface field $|E(0)|\lambda_0$ that can be achieved by a BSW in a truncated periodic multilayer as a function of the refractive index contrast between the high-index and the low-index layers in the unit cell.

In figures 2.8 and 2.9 we plotted the highest wavelength-scaled surface field $|E(0)|\lambda_0$ that can be achieved with either the fundamental TE mode or a Bloch surface wave. In both cases, one can recognize that the surface field increases with the RIC Δn, since this induces a shrinking of the modal length as shown in the previous section. Furthermore, the surface field decreases as the lower index increases, especially in the case of the TE0 mode in an optimized asymmetric slab waveguide, where confinement is only due to total internal reflection. It was also noticed that as the average refractive index of the structure increases, the maximum starts to drift away from the structure interface, as shown in fig. 2.10. Finally, we notice that the values of the surface field in the two structures are comparable.

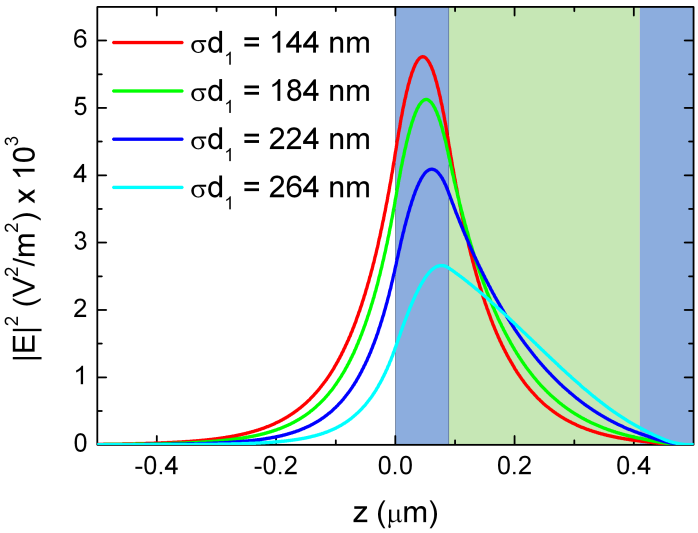

Figure 2.10: Shift of the maximum square modulus of the electric field for Bloch surface waves supported by different multilayer structures. The multilayer parameters are $d_1 = 260$ nm, $d_2 = 320$ nm, $\sigma \approx 0.346$, $n_1 = 3.48$ and either $n_2 = 1.44$ (red line), $n_2 = 1.84$ (green line), $n_2 = 2.24$ (blue line) or $n_2 = 2.64$ (cyan line).

To better compare the performance of the two structures, one can look at fig. 2.11, where we plotted the ratio between the optimized surface field of a BSW and that of the TE0 mode, once more as a function of the lower refractive index n_2 and the refractive index contrast Δn.

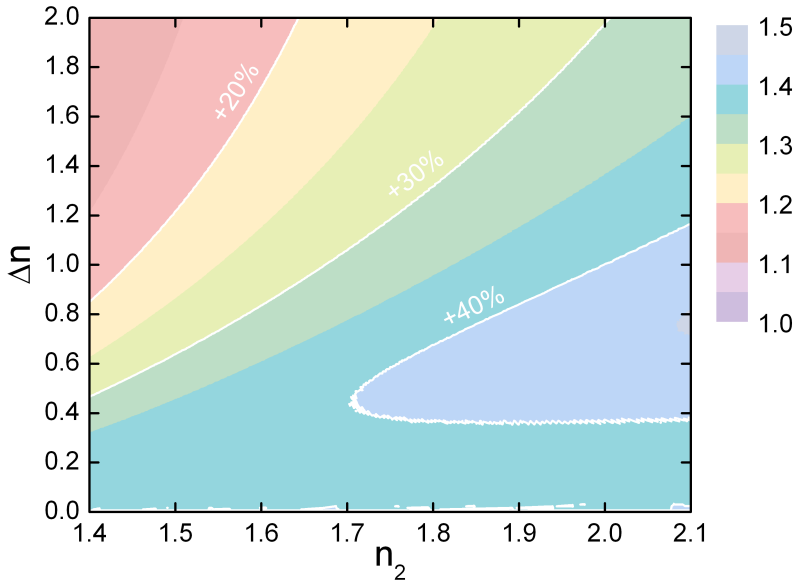

Figure 2.11: Contour plot showing the ratio between the best surface field of a BSW supported by a truncated periodic multilayer and the best surface field of the TE0 mode supported by an asymmetrical slab as a function of the lower refractive index n_2 and the refractive index contrast Δn. The star corresponds to the structural parameters used in fig. 2.6.

The contour variable is always greater than unity; this clearly shows that Bloch surface waves supported by optimized truncated periodic multilayers always have greater surface fields with respect to the fundamental mode in an asymmetric slab waveguide. The enhancement with a BSW can reach up to 45% of the TE0 surface field; this occurs when $n_2 > 1.7$ and $0.4 < \Delta n < 0.8$. Comparing this result with those summarized in fig. 2.7 leads to a surprising conclusion: the region where the surface field of a BSW overtakes that of the TE0 mode is characterized by comparable modal lengths. This means that the advantage featured by BSWs must not be ascribed to a smaller modal length, but to the particular energy distribution in the mode profile across the supporting structure, and ultimately to the fact that confinement in this complex structure is due to interference rather than total internal reflection.

Thus, these results indicate that the need for larger surface fields does not always require resorting to Bloch surface waves. Indeed, they are always characterized by the largest surface field with respect to simpler TIR-based solutions, but the enhancement is rather small, especially in the strong RIC regime.

2.6 Conclusions

In this chapter we dealt with the optimization of Bloch surface waves, and we tried to understand whether the general interest shown in their features

is justified or if simpler structures can behave similarly. With this in mind, we compared the performance of the fundamental TE mode supported by am asymmetrical slab waveguide and the Bloch surface wave supported by a truncated periodic multilayer. This comparison relied on two figures of merit, *i.e.* the modal length and the value of the electric field on the external side of the surface of the structures. For our analysis, we considered dielectric media with refractive indices in the range $[1.4; 4.1]$, with a refractive index contrast $0 < \Delta n < 2$. This wide range includes diverse materials such as semiconductors and organic media. Given the generalness of our approach, we could account for neither chromatic dispersion $n(\omega)$ nor absorption losses.

The most surprising result regards the modal length: we showed that, under certain circumstances, modes confined by total internal reflection do not always have the smallest modal length. For a strong enough refractive index contrast ($\Delta n > 0.5$), Bloch surface waves feature smaller mode length, *i.e* a larger electromagnetic energy density in a generic point across the structure, than the best TE0 mode in an asymmetric slab of any core thickness based on the same set of refractive indices. This result was obtained with a periodic multilayer obtained by enforcing a generalized quarter-wavelength condition for the thickness of the constituent layers.

On the other hand, it was shown that BSWs always exhibit larger values of the electric field at the surface with respect to the best case achievable with TIR-based solutions. However, our results show that the ratio between the surface fields does not overtake the 45% threshold, and thus simple asymmetric slabs may still be viable solutions to achieve strong light-matter interaction at the surface of the structure.

The conclusions presented in this chapter were drawn from wavelength-independent figures, and thus they apply to a wide range of energies in which our hypotheses are satisfied.

The results presented in this chapter were published in 2017[29].

Chapter 3

Gratings for Bloch surface waves

In this chapter we shall consider a patterned multilayer structure composed of a one dimensional grating placed on top of a truncated one-dimensional photonic crystal. The multilayer supports a Bloch surface wave, and the presence of the grating strongly modifies its dispersion relation and its field distribution. Our analysis relies on rigorous coupled wave analysis (RCWA), which is exact within numerical approximations, but we also propose a numerical solution based on effective-index theory to quickly reconstruct the dispersion relations.

3.1 Motivation

Diffraction gratings fabricated on top of a periodic multilayer have been investigated either to excite Bloch surface waves or as the main transducer element in the field of optical sensing. In all these situations, one is forced to work both above the light line of the cladding material and the diffraction cut-off[11, 49], but in 2008 Descrovi et al.[50] showed that the dispersion relation of Bloch surface waves supported by a truncated one-dimensional photonic crystal and a photonic crystal slab located on top of it can change dramatically and give rise to the opening of a photonic band gap. This is not entirely new in the context of photonic-crystal slabs. For example, it was shown by Gerace and Andreani[51] that the propagating modes featured by these systems can be seen as arising from the coupling between the guided modes supported by an effective slab formed by the presence of the two-dimensional photonic crystal. This gives rise to a strong modification of the mode dispersion relation and to the opening of photonic band gaps in which light propagation in the plane is forbidden. The interaction between surface waves and periodically corrugated one-dimensional photonic crystals (1DPC) has also been studied experimentally[52, 53]. The long-term experimental interest is clear: by nature, surface waves are extremely sensitive to any sort of modification involving the top layers in the supporting 1DPC; indeed, most Bloch surface waves-based optical sensors rely on this feature[28, 54, 55]. Besides, especially when sur-

face electromagnetic waves are involved, the opening of bandgaps induced by a grating is also useful for a variety of goals, ranging from light guiding[56] to amplification of the interaction between light and matter[57].

All these results may be of particular interest when focusing on BSW-oriented integrated optics. In this context, photonic crystals are fundamental tools which allow one - among the rest - to control the propagation of light and to design BSW-based resonators[14, 13, 39, 16, 15, 58].

With a view to implementing Bloch surface waves integrated optics, in this chapter I will present some results of a systematic study on the interaction between a one-dimensional PhC slab and a one-dimensional truncated periodic multilayer supporting a Bloch surface wave. In particular, we analyzed the effect of the structural parameters of the grating, *e.g.* its refractive index, its height and its filling fraction, on the dispersion of the mode and on the electric field distribution. This analysis was carried out by means of rigorous coupled-wave analysis and even confirmed via the approximate method of effective-index theory.

3.2 Structure details

A sketch of the structure we investigated is reported in fig. 3.1.

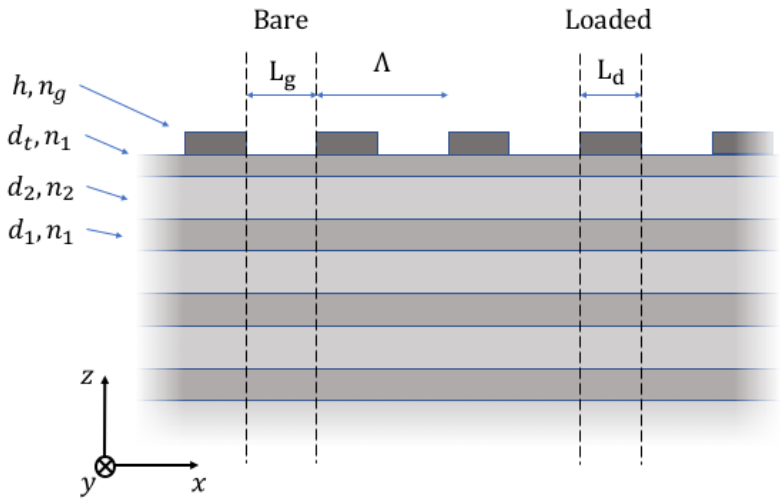

Figure 3.1: Sketch of the structure under consideration.

The structure consists of a one-dimensional rectangular grating placed transversally on top of a one-dimensional truncated periodic multilayer. The grating is periodic along the x direction, with a period $\Lambda = L_d + L_g$ and a filling fraction $f = 1 - L_g/\Lambda$, its height is h_g and its refractive index n_g. On the other hand, the underlying one-dimensional photonic crystal is periodic along the z direction; its unit cell is formed by two layers of refractive indices n_1, n_2 and

thicknesses d_1, d_2, respectively. The top layer of this photonic crystal is truncated to a thickness $d_t = \sigma d_1$, where the truncation factor, as was explained in chapter 1, satisfies the inequality $0 < \sigma < 1$. Altogether, the system consists of two different periodic structures: the multilayer, which supports and confines the Bloch surface wave along z, and the grating, which gives rise[50] to a photonic band structure along x. As before, even in this chapter we will only focus on TE-polarized light, *i.e.* where the only non-vanishing components of the electromagnetic field are H_x, E_y and H_z.

3.3 Theoretical procedure

The structure shown in figure 3.1 can support propagating modes confined in the z direction by both total internal reflection and the presence of a photonic band gap. Their dispersion relation can be reconstructed experimentally by means of attenuated total reflectance or angle-resolved reflectance measurements[59, 60]. For example, one may couple light into the structure via a prism in the Kretschmann configuration and focus on the guided modes lying below the light line corresponding to the cladding. Numerically, one may resort to approaches that take into account the periodicity of the system, such as rigorous coupled-wave analysis (RCWA)[61, 62].

The new theoretical setting is sketched in fig. 3.2.

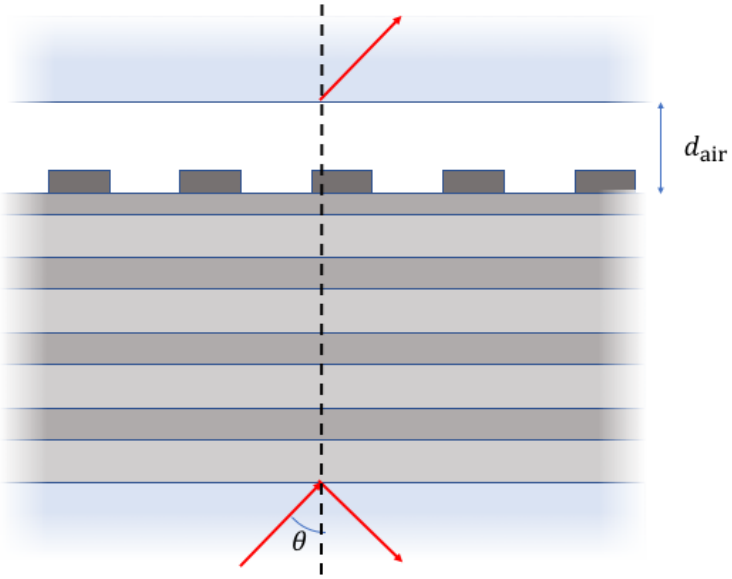

Figure 3.2: Typical setting for a numerical attenuated total reflectance simulation. A coupling prism is attached to the lower interface of the structure. Light from this layer can either be reflected backwards or couple into a mode supported by the structure.

The prism is represented by a high-index layer located at a distance d_{air} from the surface of the structure. A mode is excited by means of a second

high-index layer in the Kretschmann configuration. When light impinges on the lower interface between the prism and the multilayer, it can either be reflected back into the prism or tunnel into the upper layer; in this second scenario, the coupling of light into the structure would result in a dip in the reflectance spectrum, whose visibility would ultimately depend on the coupling conditions: in a system such as the one we analyzed, the coupling efficiency towards the upper layer increases exponentially[44, 43] with the distance d_{air}, whereas the coupling efficiency towards the substrate decreases exponentially with the number of periods in the multilayer[16]. The *critical coupling* condition, in which the reflectance dips would drop to 0, would require the absence of absorption and the coupling efficiencies towards the upper and lower substrates to be identical; however, in a numerical simulation one can tune the excitation conditions by tweaking both the number of periods in the vertical multilayer and the distance d_{air} to adjust the visibility of the dip to any desired value. Figure 3.3 shows a typical reflectance spectrum plotted as a function of the angle of incidence θ in the lower prism.

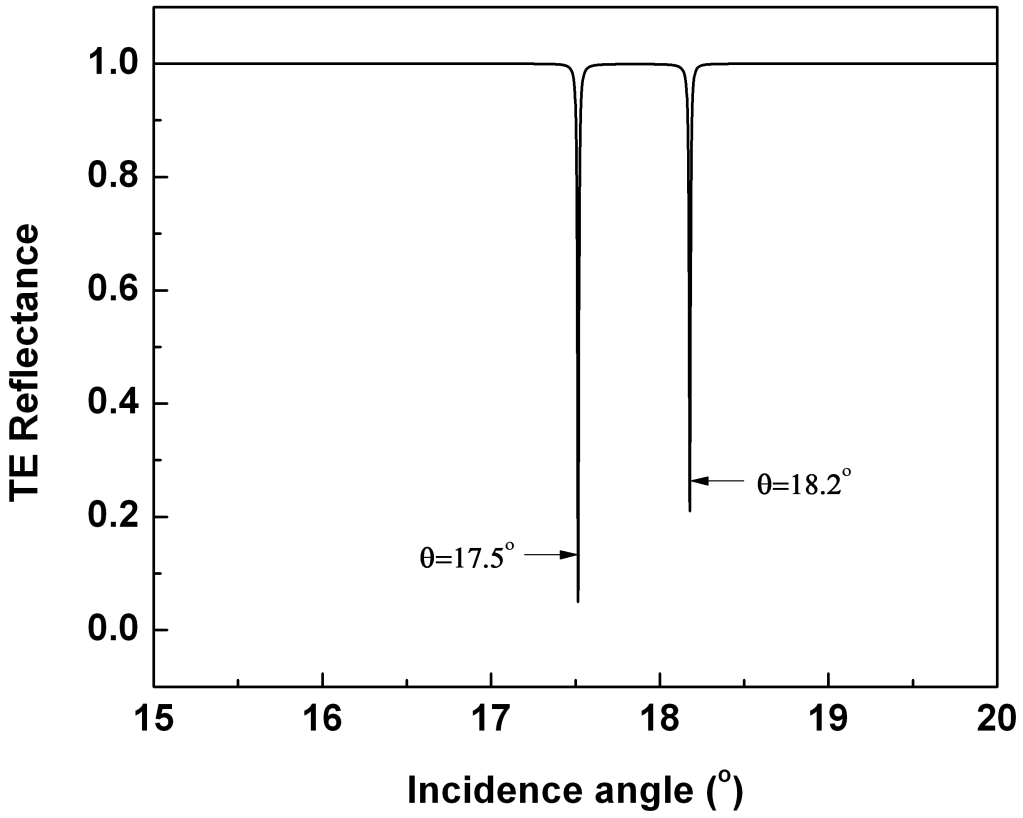

Figure 3.3: Reflectance spectrum of the structure as a function of the angle of incidence at the energy $E = 1.1642$ eV.

Similarly, one can calculate the reflectance spectra at fixed angles and varying energy. In fig. 3.4 we reported the reflectance spectra for fixed angles of incidence from $\theta_{min} = 13°$ to $\theta_{max} = 25°$. It has been shown[60] that one can extract the dispersion relation of the mode supported by the ideal, isolated structure, provided the coupling to the extra coupling elements is sufficiently small.

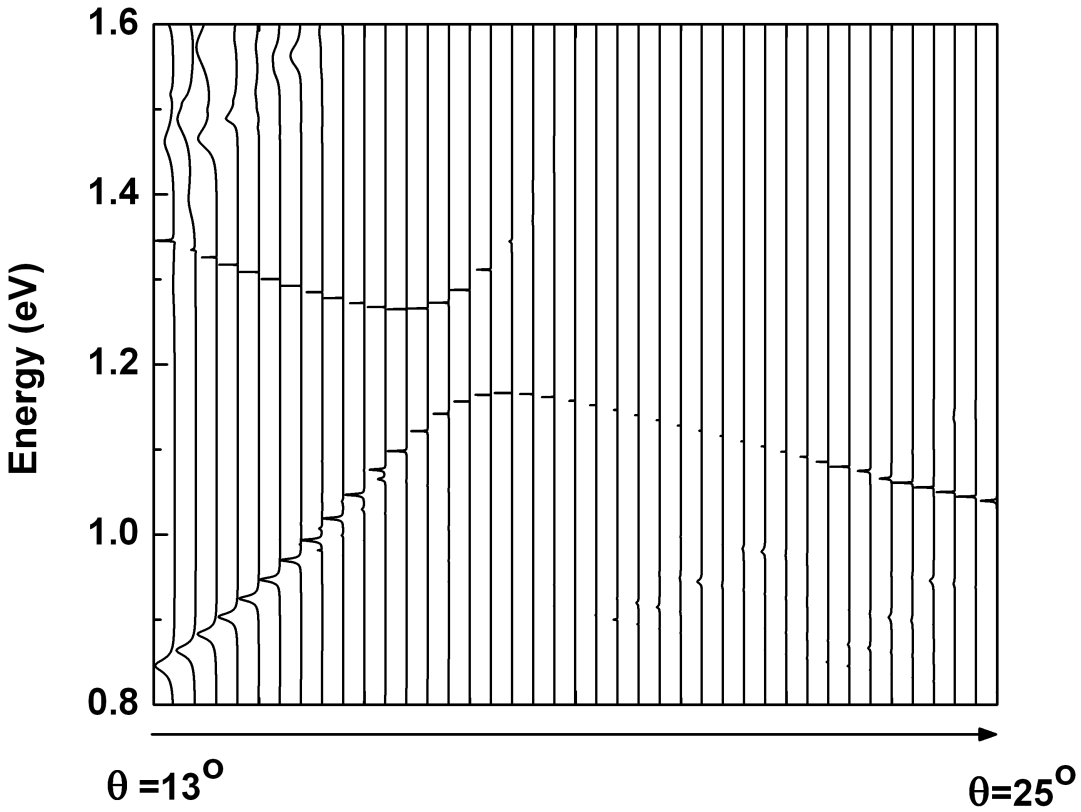

Figure 3.4: Reflectance spectrum at different angles of incidence, for a structure with a filling fraction $f = 0.5$.

In order to calculate of the modes supported by the structure in fig. 3.1 one can also resort to the approximation of the effective-index method (EIM)[48, 63], which is particularly useful when both the *loaded* and *bare* regions of the structure support Bloch surface waves[13]. In this case, one can approximate these regions as uniform materials having refractive indices n_{load} and n_{bare} given by the frequency-dependent effective indices of the supported modes, thereby reducing the dimensionality of the problem.

In our case, the structure can be approximated as an effective one-dimensional photonic crystal with alternating layers of width L_g for the bare region (the grooves in the grating) and $\Lambda - L_g$ for the loaded region (the rulings of the

grating), and the band structure of the approximated system can be found by calculating the overall transmittance and its poles, as explained in appendix A. Naturally, this simplification translates in an improvement of the calculation times, and thus it allows for a quick exploration of the vast parameter space involved in such complex structure. In the rest of this chapter, it will be shown that under the hypothesis mentioned above, the agreement between the effective-index method and the spectra calculated with rigorous coupled-wave analysis is rather accurate.

3.4 Results and discussion

The first system we analyzed was the one in fig. 3.1, *i.e.* a structure whose unit cell is formed by layers of thickness $d_1 = 111.3$ nm, $d_2 = 263.7$ nm and refractive indices $n_1 = 2.5$, $n_2 = 1.45$. The truncation layer has thickness $d_t = \sigma d_1 = 11.13$ nm, where $\sigma = 0.1$. These parameters were obtained with the optimization procedure described in chapter 2: the layer thicknesses were chosen using a generalized quarter-wavelength condition for the gap design, and the truncation factor guaranteed the existence of a Bloch surface wave within the photonic band gap with the largest surface field enhancement achievable given the refractive indices provided[29]. Finally, the grating has a refractive index $n_g = 1.7$, and period $\Lambda = 434.8$ nm and thickness $h = 111.3$ nm. All the results reported in this chapter were scaled to the wavelength, which in our case was taken as $\lambda_0 = 1$ μm; this means that if chromatic dispersion is negligible, the results can be scaled to any wavelength the reader might be interested in.

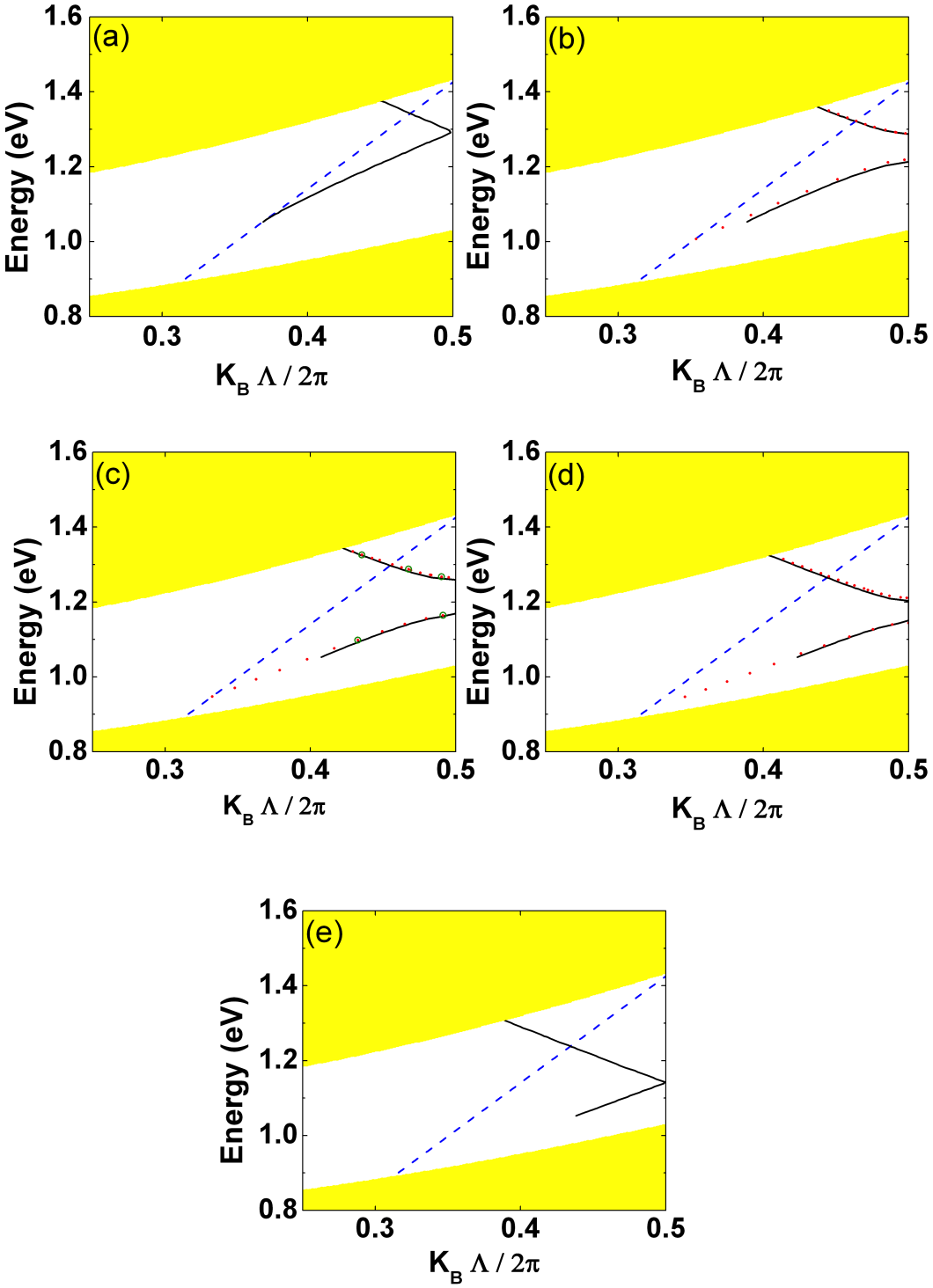

Figure 3.5: Dispersion relation for the Bloch surface waves in the patterned multilayer approximated via the EIM (solid line) and RCWA (dotted) for various grating filling factors: (a) $f = 0$ (no grating), (b) $f = 0.25$, (c) $f = 0.5$, (d) $f = 0.75$, (e) $f = 1$ (full layer) and thickness $h = 111.3$ nm. The white region corresponds to the band gap. The band structure of the photonic crystal for TE-polarized light is also shown, together with the light line of air (dashed).

The dispersion relation of the mode supported by the structure in fig. 3.1 is shown in fig. 3.5 for different values of the filling fraction of the grating $f = L_d/\Lambda$. The dispersion relation is plotted as a function of the in-plane component of the wave vector k_x, *i.e.* along the grating direction; the periodicity of the grating along x allows a reduction to the first Brillouin zone associated to the period Λ. The two extreme cases in which the filling fraction equals $f = 0$ (figure 3.1a) and $f = 1$ (figure 3.1e) correspond to the dispersion relation of the Bloch surface waves supported by the *bare* multilayer and the *loaded* multilayer, *i.e.* one in which no grating is present and one surmounted with a uniform layer of height h and refractive index n_g. In these two cases, the folding of the energy/wave vector plot inside the first Brillouin zone is clearly arbitrary, as the structures are invariant for any in-plane translation.

On the other hand, when the filling fraction satisfies the inequality $0 < f < 1$, the translation invariance in the xy plane does not hold, as the presence of the grating implies that the structure is no longer uniform in the plane. These cases correspond to figures 3.5(b-d), which are associated to the filling fractions $f_b = 0.25$, $f_c = 0.25$ and $f_d = 0.25$, respectively. The black solid lines represent the dispersion relations calculated by means of effective-index theory; the red dots correspond to the results obtained by means of rigorous coupled-wave analysis. As can be seen from fig. 3.5, the agreement between the two methods is striking for each filling fraction f. The presence of a photonic band gap along k_x, *i.e.* for light propagating along x, can be seen as resulting from the contra-directional coupling of the forward- and the backward-propagating Bloch surface waves supported by the truncated multilayer in which the grating has been substituted by an effective slab. The coupling is determined by the grating, and its strength depends on the filling factor f, as can be deduced by the fact that the largest photonic band gaps correspond to values of the filling fraction close to $f = 0.5$.

Furthermore, the position of the mode inside the photonic band gap can be piloted by means of the filling fraction of the grating. As the filling fraction f increases, the refractive index of the effective slab increases; this increase in the optical thickness causes the band structure in fig. 3.5 to redshift.

To complete the analysis, and with a view to potential applications in the field of biosensing, in figure 3.6 we plot the square modulus of the electric field calculated with rigorous coupled-wave analysis. The setup is the one described in fig. 3.2, *i.e.* the excitation of the mode occurs in the Kretschmann configuration. In the case of figures 3.6a-b, the field distribution is peaked in the rulings of the grating: this occurs because the parameters belong to the lower band, *i.e.* the so-called *dielectric band*. Light is localized near the surface of the multilayer, it decays in air because the modes lies below the corresponding light line and undergoes damped oscillations in the stacking direction of the multilayer, which is a clear signature of the presence of a photonic band gap.

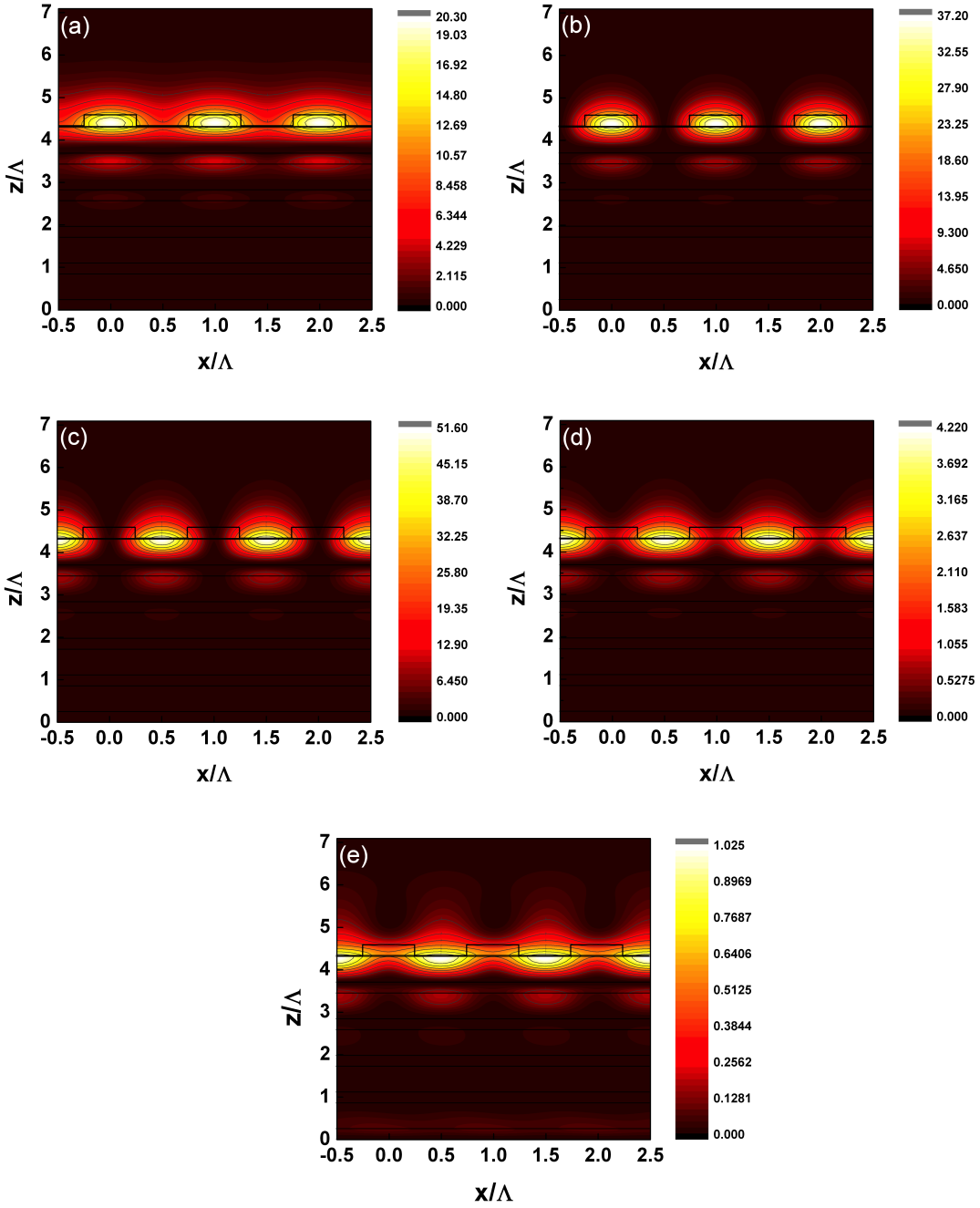

Figure 3.6: Square modulus of the electric field obtained by means of rigorous coupled-wave analysis for a few selected values of $\frac{K_B\Lambda}{2\pi}$: (a) 0.4326 , (b) 0.4912, (c) 0.4903, (d) 0.4676 and (e) 0.4335. The modes in figures (a) - (b) correspond to the lower bands, whereas figures (c) - (e) correspond to the upper bands.

In figures 3.6c-e, we show the field distributions for points in the upper band, the so-called *air band*. Indeed, in this case the maxima of the field are concentrated between the rulings, *i.e.* inside the air gaps in the grating. As one considers points even higher in energy, *e.g.* fig. 3.6d-e, the dispersion

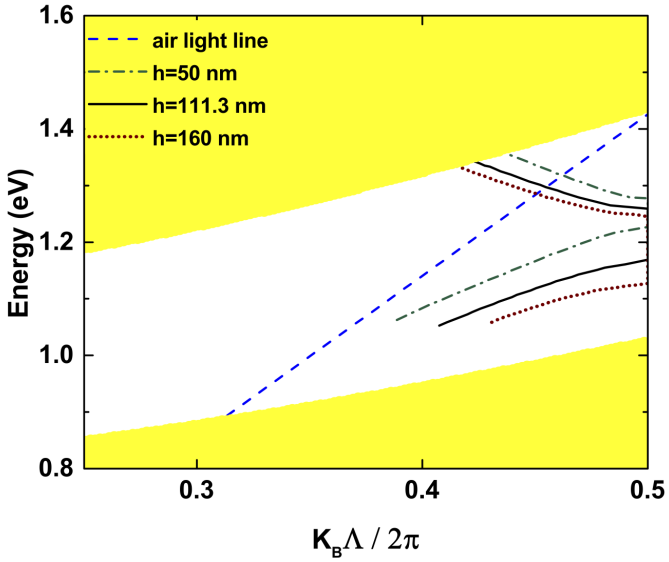

Figure 3.7: Dispersion relation of Bloch surface waves for several grating heights. The theoretical curves were done by means of the EIM for heights $h = 50$ nm (dash dot line), $h = 111.3$ nm (solid line) and $h = 160$ nm (dot line). The filling fraction was $f = 0.5$ throughout the analysis.

relation approaches the light line and the modes are less and less confined in the grating region. Fig. 3.6e in particular corresponds to a point above the light line, where the field distribution no longer decays in the cladding as the modes are coupled to those in the radiative region. This situation is akin to that of quasi-guided modes of a photonic crystal slab[59].

Lastly, we evaluated the role of the grating height on the dispersion relation of the Bloch surface waves. Indeed, the strength of the contra-directional coupling between the forward- and backward-propagating modes depends on all its parameters, *i.e.* its refractive index n_g, its filling fraction f and also its height h. For example, it is known[64, 65] that the response of the grating under certain conditions - typically when the thickness of the grating itself is smaller than the wavelength of light - is proportional to the square of the grating height h^2. Thus, in fig. 3.7 we report the Bloch surface wave dispersion relation for heights of the grating equal to $h_1 = 50$ nm (dash-dotted line), $h_2 = 111.3$ nm (solid line) or $h_3 = 160.0$ nm (dotted line).

The effect of the increasing grating height h is both a gradual red-shifting of the center of the photonic band gap and a widening of the gap itself. A wider gap also entails a relative flattening of the dispersion relation in the proximity of the band edge, which corresponds to a smaller group velocity: this is particularly relevant with a view to enhancing the interaction between light and matter.

It is worth noticing that when the structure does not support guided modes, the validity of the effective-index method is debatable. To show this, we chose

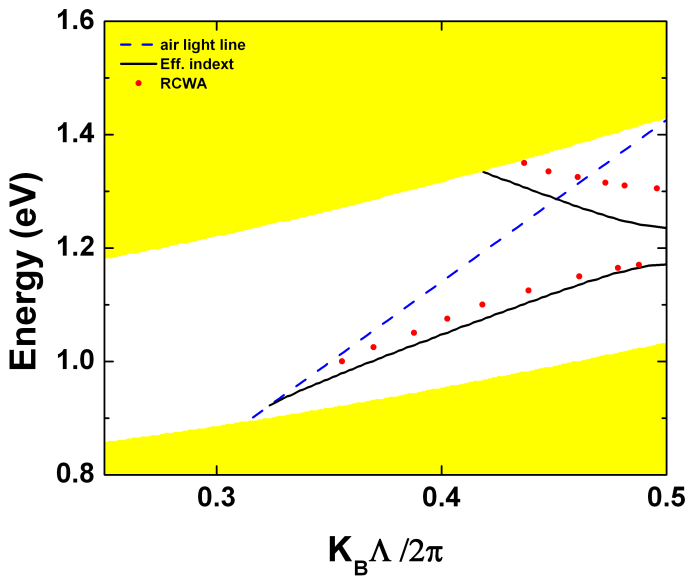

Figure 3.8: Dispersion relation of the Bloch surface waves for a structure supporting no *bare* modes. The exact numerical solutions are shown in red dots; the solution obtained via the effective-index method is shown in solid black. The so-called *dielectric mode* band, *i.e.* the lower one is recovered with both approaches, whereas the *air mode* band shows significant differences between the two methods.

to slightly modify the structure shown in fig. 3.1: the new truncation layer is now $\sigma d_1 = 327$ nm. To follow the same approach we applied earlier in this chapter, we assume an effective index for the bare structure equal to the refractive index of air, *i.e.* $n = 1.0$. The results are shown in fig. 3.8; as can be seen from the plot, the dispersion relations calculated via the scattering matrix approach and the effective-index method are in relatively good agreement in the lower band, *i.e.* the one relative to dielectric modes, but suffer from significant discrepancies in the upper band.

3.5 Conclusions

In this chapter we studied the behavior of guided modes supported by a one-dimensional grating located on a one-dimensional truncated periodic multilayer as a function of the geometrical parameters of the grating. Firstly, the field distributions and the modal dispersions were calculated via rigorous coupled-wave analysis. To simplify this approach, we successfully applied effective-index theory to approximate the grating region: our simulations found an excellent agreement between the results obtained with the two methods, thus confirming the validity of this approximate approach.

The periodicity of the grating causes a folding of the dispersion relation of the modes in the first Brillouin zone; this gives rise to the opening of a photonic band gap between the two branches of the folded dispersion relation. Both the position of the modes inside the band gap and the width of the gap strongly depend on the filling factor of the grating: as the filling factor increases, the effective index of the equivalent slab increases: this increase in the optical thickness of the slab causes a redshift of the guided modes.

Moreover, the effect of the height of the grating was studied by means of effective-index theory: as the grating becomes thicker, the guided modes redshift further and the width of the gap increases.

The electric field distributions of the modes belonging to the lower or upper branches of the dispersion relation are localized in the dielectric ridges of the grating or in the air gaps between the rulings, respectively.

The results shown in this chapter were published in 2018[30].

Chapter 4

BSW ring resonators

Ring resonators are optical waveguides looped back onto themselves in the shape of a circle. When the optical path of the resonator is an integer number of wavelengths, a resonance occurs, and the distance between adjacent resonances is called free spectral range. Ring resonators by themselves would be unaccessible from the outside world, therefore they become useful only when some kind of coupling to external optical elements exists. The easiest and by far the most common coupling technique relies on evanescent coupling between the ring and an bus waveguide close by. In the case of a single ring resonator, the transmission spectrum as measured on the bus waveguide shows dips at the resonances of the ring. Ring resonators can be useful in a variety of applications, ranging from optical filters, optical sensing, optical communications, etc.

Thus, with a view to employing Bloch surface waves in integrated optics, ring resonators are fundamental building blocks. In this chapter, I will report our results on the first experimental observation of a BSW-based ring resonator.

4.1 Motivation

In order to obtain complete integration of Bloch surface waves, BSW-based optical resonators must be adequately investigated. Resonators are unavoidable components for many reasons. In the first place, they have much smaller footprints than those that would be necessary for travelling light. Moreover, having light dwell inside a small enough volume for a long enough time amplifies its chances of interacting with matter inside said volume. This is the basis of a series of physical applications ranging from optical biosensors[32, 33, 38, 11], interaction with 2D materials[66] and with quantum dots[67].

It is already known that Bloch surface waves can be guided by fabricating dielectric ridges on top of the supporting multilayer. In this case, BSWs are confined vertically by both total internal reflection (TIR) and the pres-

ence of a photonic band gap (PBG), and the additional lateral confinement is achieved via TIR. Guided BSWs (GBSWs) in ridges have been studied both theoretically[13] and experimentally[14, 68, 69], and it has also been suggested theoretically that BSWs could be confined in ring resonators[16]. Indeed, after the theoretical suggestion, the first BSW-based microdisk resonator was fabricated and demonstrated experimentally[15] by Herzig et al.

Along this line, in this chapter, I will present our results on the first experimental confirmation of a Bloch surface wave ring resonator. This joint work was a collaboration with the group of professor S. M. Weiss from Vanderbilt University, in Tennessee. Both the ring and the underlying multilayer were fabricated in porous silicon (pSi), a low-cost and extremely tunable material that has already been successfully employed in a variety of physical scenarios ranging from tunable Bragg mirrors, microcavities, etc[70, 71].

4.2 Basics of ring resonator theory

Ring resonators are fundamental optical elements that lead to the confinement of light in three dimensions. They are essentially formed by a ridge waveguide bent in a closed circular shape, as sketched in fig. 4.1.

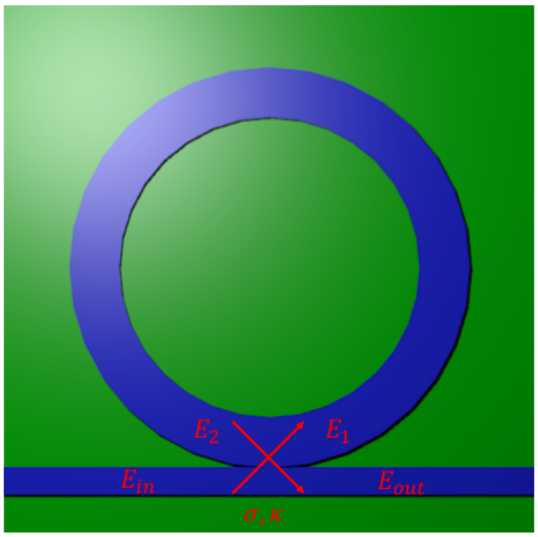

Figure 4.1: Sketch of a ring resonator of radius R.

Light can be injected inside the ring resonator by means of evanescent side-coupling to a *bus waveguide*. The strength of the coupling depends essentially on the distance between the ring resonator and the waveguide itself: this distance is typically designed before fabrication, but it can also be fine-tuned in a completed structure by employing heaters, which can slightly modify the ring by thermal expansion. In its simplest version, the coupling between the bus waveguide and the ring resonator can be expressed in terms of two real

values: the *cross-coupling constant* κ and the *self-coupling constant* σ. When the coupling is reciprocal, the two coupling constants satisfy $\sigma^2+\kappa^2 = 1$. With reference to fig. 4.1, we can write[48]

$$E_1 = \sigma E_2 + i\kappa E_{in} \tag{4.1}$$
$$E_{out} = i\kappa E_2 + \sigma E_{in}. \tag{4.2}$$

As light propagates inside the ring, it is subject to various sources of losses, such as bending, absorption and scattering losses. All these effects can be taken into account with a single loss coefficient $0 < \alpha < 1$, *i.e.*

$$E_2 = \alpha E_1 e^{ik(\omega)\cdot L}, \tag{4.3}$$

where $L = 2\pi R$ is the length of a full round trip around the ring resonator. Clearly, the case when $\alpha = 1$ represents the lossless scenario. For the field in eq. (4.3) to undergo constructive interference as it resonates inside the ring, the following condition must hold:

$$k(\omega)L = 2\pi m, \tag{4.4}$$

where $m \in \mathbb{Z}$ is an integer. The wave vector $k(\omega)$ can be expanded around a central frequency ω_0 to get

$$k(\omega) = \frac{\omega_0}{c}n + \frac{1}{v_g}(\omega-\omega_0) + \frac{1}{2}GVD(\omega-\omega_0)^2 + \cdots, \tag{4.5}$$

where n is the refractive index at frequency ω_0,

$$v_g = \frac{\partial\omega}{\partial k} \tag{4.6}$$

is the *group velocity* and

$$GVD = \frac{\partial^2 k(\omega)}{\partial^2\omega} \tag{4.7}$$

is the group velocity dispersion. We can evaluate the transmittance $T(\omega)$, defined as

$$T(\omega) \equiv \left|\frac{E_{out}}{E_{in}}\right|^2 \tag{4.8}$$

starting from the ratio between the amplitudes of the transmitted field and the incoming field, *i.e.*

$$\frac{E_{out}}{E_{in}} = \frac{\sigma - \alpha e^{ik(\omega)L}}{1-\sigma\alpha e^{ik(\omega)L}}. \tag{4.9}$$

Altogether, one has[72]

$$T(\omega) = \frac{\sigma^2+\alpha^2-2\sigma\alpha\cos(k(\omega)L)}{1+\sigma^2\alpha^2-2\sigma\alpha\cos(k(\omega)L)}. \tag{4.10}$$

From eq. (4.10), one can recognize that the resonant frequencies given by condition (4.4) correspond to the minima in the transmittance. The transmittance is plotted in figure 4.2.

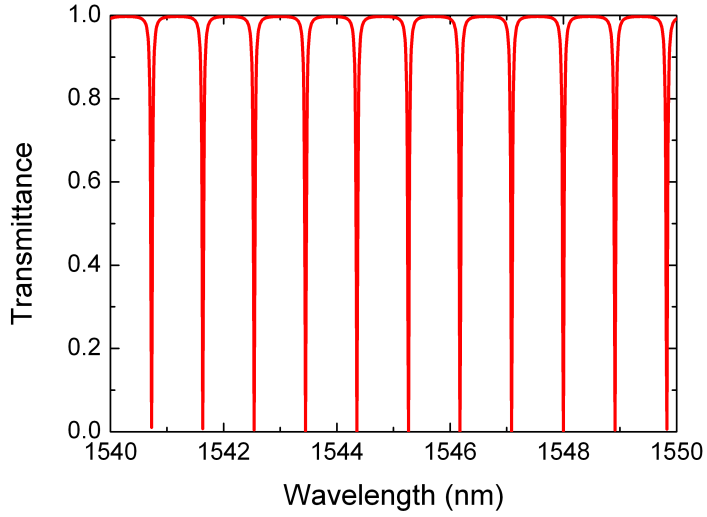

Figure 4.2: Transmission spectrum for a side-coupled ring of radius $R = 120\ \mu m$ ($\alpha = \sigma = 0.95$) in critical coupling condition.

The frequency distance between adjacent resonances is the *free spectral range*, defined as

$$FSR_\nu = \frac{c}{2\pi R n_g}, \tag{4.11}$$

where n_g is the group index of the mode. When the frequency ω equals one of the resonances of the ring ω_{res}, the transmittance simplifies to

$$T(\omega_{res}) = \frac{(\sigma - \alpha)^2}{(1 - \sigma\alpha)^2}. \tag{4.12}$$

When $\sigma = \alpha$, the transmission at resonance becomes $T(\omega_{res}) = 0$. This is known as *critical coupling condition*, and it usually a useful experimental condition due to the high visibility of the dips. A fundamental figure of merit for resonators is the *quality factor* Q, which is defined as the number of oscillations undergone by the field before its amplitude drops to a fraction $1/e$ of its original value; thus, this factor gives a precise measurement of how effective the three-dimensional confinement of light is, since any source of loss is detrimental to its value. The quality factor can in general be extracted from a transmission spectrum such as the one shown in figure 4.2 by evaluating the ratio between the resonance frequency and the FWHM of the dip, *i.e.* $Q = \omega_{res}/\Delta\omega$. However, it is possible to separate different contributions inside the overall quality factor.

The bus waveguide, in addition to being a way to couple light inside the resonator, is also a way for light to escape it. This term gives an *extrinsic* quality factor Q_{ext}. Scattering, absorption and bending losses, on the other hand, contribute to an *intrinsic* quality factor Q_{int}, which is defined by

$$Q_{int} = \frac{2\pi n_g}{\lambda_j a}, \tag{4.13}$$

where the λ_js are the resonance wavelengths and a is a loss coefficient in units of reciprocal length.

4.3 Structural parameters

The structure we analyzed is sketched in figure 4.3. It consists of a multilayer composed of $N = 24$ layers fabricated in porous silicon of different porosities[28]. A porous-silicon ring resonator of radius $R = 105$ μm was realized on top of the multilayer by means of electron beam lithography; the width of the ridge is $w_{WG} = 6$ μm, and its height is $h_{WG} = 149$ nm. The refractive index of the porous-silicon ring structure is $n_{WG} = 1.69$. 100 nm away from the outer radius of the ring lies a tapered channel waveguide to couple light into the resonator. The geometrical features of the channel waveguide in the coupling region is the same as the ring: its width is $w_{WG} = 6$ μm and its height is $h_{WG} = 149$ nm.

The ring was realized on top of a truncated periodic multilayer formed by porous silicon layers of alternately high or low refractive index. The refractive index of the high-index layer is $n_{high} = 1.79$ and its thickness is $d_{high} = 248$ nm; the refractive index of the low-index layer is $n_{low} = 1.24$, and its thickness is $d_{low} = 704$ nm. Between the periodic crystal and the ring lie three layers with the following structural details: $d_1 = 753.5$ nm, $n_1 = 1.24$; $d_2 = 231$ nm, $n_2 = 1.69$; $d_3 = 743$ nm, $n_3 = 1.24$.

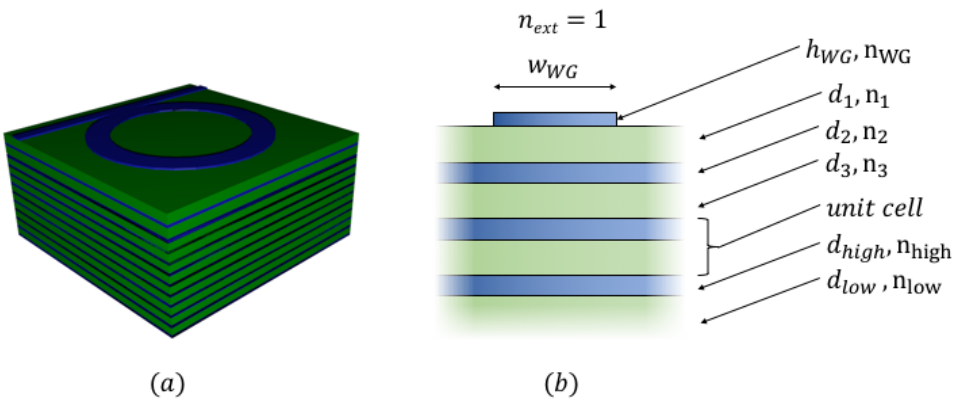

Figure 4.3: Sketch of the three-dimensional structure under scrutiny. The ring and channel waveguide are not to scale.

The inclusion of pores inside the silicon matrix is achieved with a combination of electrochemical etching and lithographic processing. A thorough description of the fabrication process can be found in [54], but for the sake of clarity it will also be sketched out here. As previously reported[28], the porous-silicon multilayer was formed by electrochemical etching of p+ (0.01 Ω·cm) Si (100) in a 15% hydrofluoric acid (HF) solution. The top layer was electrically etched at a current density of 18 mA/cm^2 for 28 s. The following two layers were etched at current densities of 48 mA/cm^2 for 22 s and 18 mA/cm^2 for 34 s, respectively. The rest of the multilayer was obtained by etching 10 unit cells formed by high and low refractive index layers with an alternating current density of 5 mA/cm^2 for 63 s and 48 mA/cm^2 for 22 s, respectively. Finally, the pore diameters were widened by drop casting a 1.5 mM KOH solution in ethanol on the as-anodized pSi multilayer film for 5 minutes. The structure was then rinsed with ethanol. The porous silicon surface was passivated via thermal oxidation at 500°C for 5 minutes in air. Finally, the ring resonator pattern was then transferred on top of the pSi multilayer by electron beam lithography and reactive ion etching. To confirm the layer thicknesses reported above, the pSi structure was studied by means of scanning electron microscopy imaging, and reflectance spectra at normal incidence were fitted with transfer matrix simulations.

4.4 Results and discussion

The lateral confinement of the Bloch surface wave inside the ring resonator was accounted for by means of the effective-index method (EIM)[13]. Following the horizontal EIM[16], we substituted the porous silicon ridge on top of the multilayer with an effective homogeneous layer of the same thickness h_{WG} and a refractive index $n_{eff,WG}(\omega)$ calculated as the fundamental TM[1] guided mode supported by a symmetric slab waveguide of porous silicon ($n = 1.69$) of width w_{WG} surrounded by air ($n = 1$).

[1]Note that in this scenario, TM polarization refers to the plane of the porous silicon ridge.

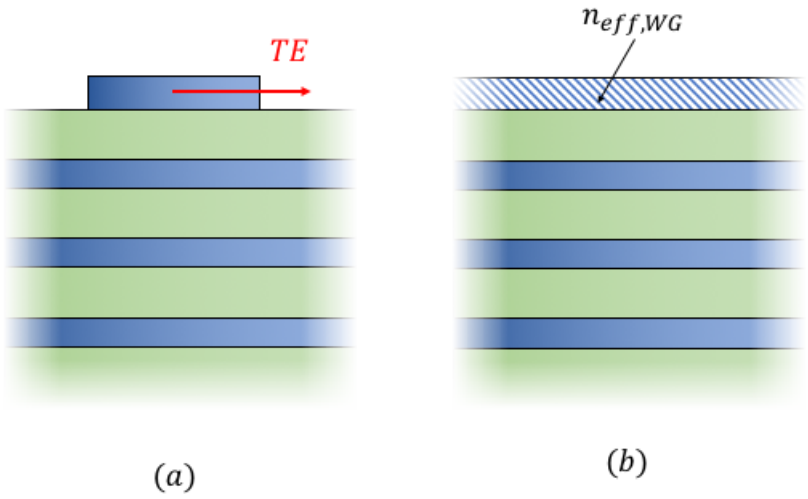

Figure 4.4: The original truncated periodic multilayer supporting a ring resonator (a) and the structure approximated via effective-index theory (b): the effective slab has the same height as the ridge in (a), and the refractive index of the TM0 mode supported by the ridge in air.

In this specific case, the width of the curved ridge is $w_{WG} = 6\ \mu m$, which is wide enough to cause but a slight variation in the effective index $n_{eff,WG} = 1.685 \approx n_{WG}$.

With this uniform layer, the photonic crystal ridge was numerically shown to support two guided Bloch surface waves whose dispersion relations are shown in Fig. 4.5.

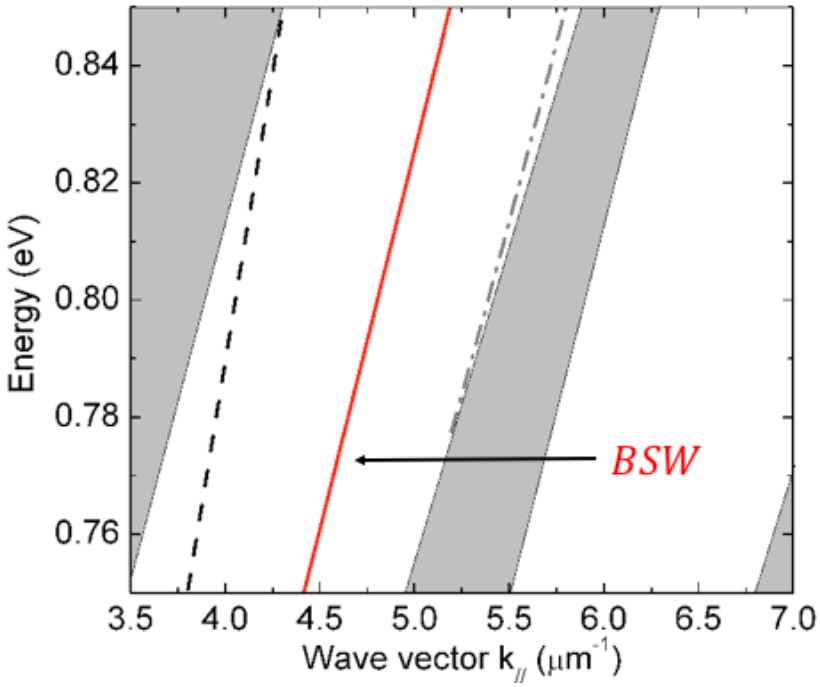

Figure 4.5: Dispersion relation for the modes in the photonic band gap (lighter region). The air light line is shown in dashed black, the BSW is solid red and a further gap mode is shown in gray (dotted and dash-dotted).

The white region in fig. 4.5 corresponds to the photonic band gap of the periodic multilayer, and the dashed black line represents the light line of the external medium (air, $n_{ext} = 1$). The parameters of the unit cell were chosen so that the photonic band gap would be reasonably wide, and the truncation factor was selected in order to have a guided Bloch surface wave around the center of the gap for the energy of interest, $E = 0.8$ eV. Fig. 4.5 also shows the presence of two guided Bloch surface waves inside the photonic band gap: the first one is close to the lower band edge and has the largest wave vector component ($k_{\parallel}^{BSSW} = 5.39\ \mu m^{-1}$); the electric field associated to this mode is peaked in the third layer, and the mode is thus a Bloch *sub-surface* wave[28]. The other gap mode falls at $k_{\parallel} = 4.80\ \mu m^{-1}$ at $E = 0.8$ eV, and its electric field profile is peaked at the interface between the truncated multilayer and the curved ridge. This is the Bloch surface wave we are interested in.

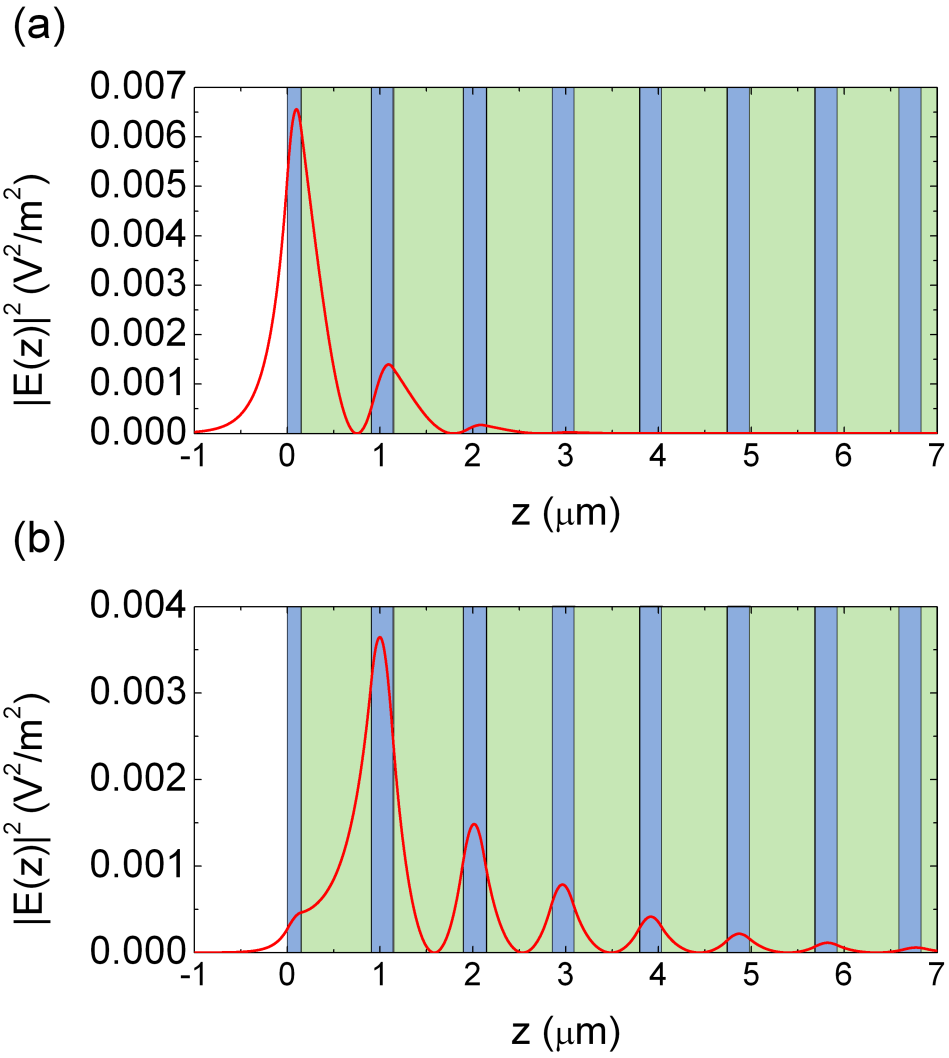

Figure 4.6: a) Square modulus of the electric field of the Bloch surface wave ($k_{\parallel}^{BSW} = 4.80\ \mu m^{-1}$); b) Square modulus of the electric field of the Bloch sub-surface wave ($k_{\parallel}^{BSSW} = 5.39\ \mu m^{-1}$).

When light at $\lambda_0 = 1.55\ \mu m$ plugged into the channel waveguide couples to the porous silicon ring, the transmission spectrum contains the typical dips shown in fig. 4.7.

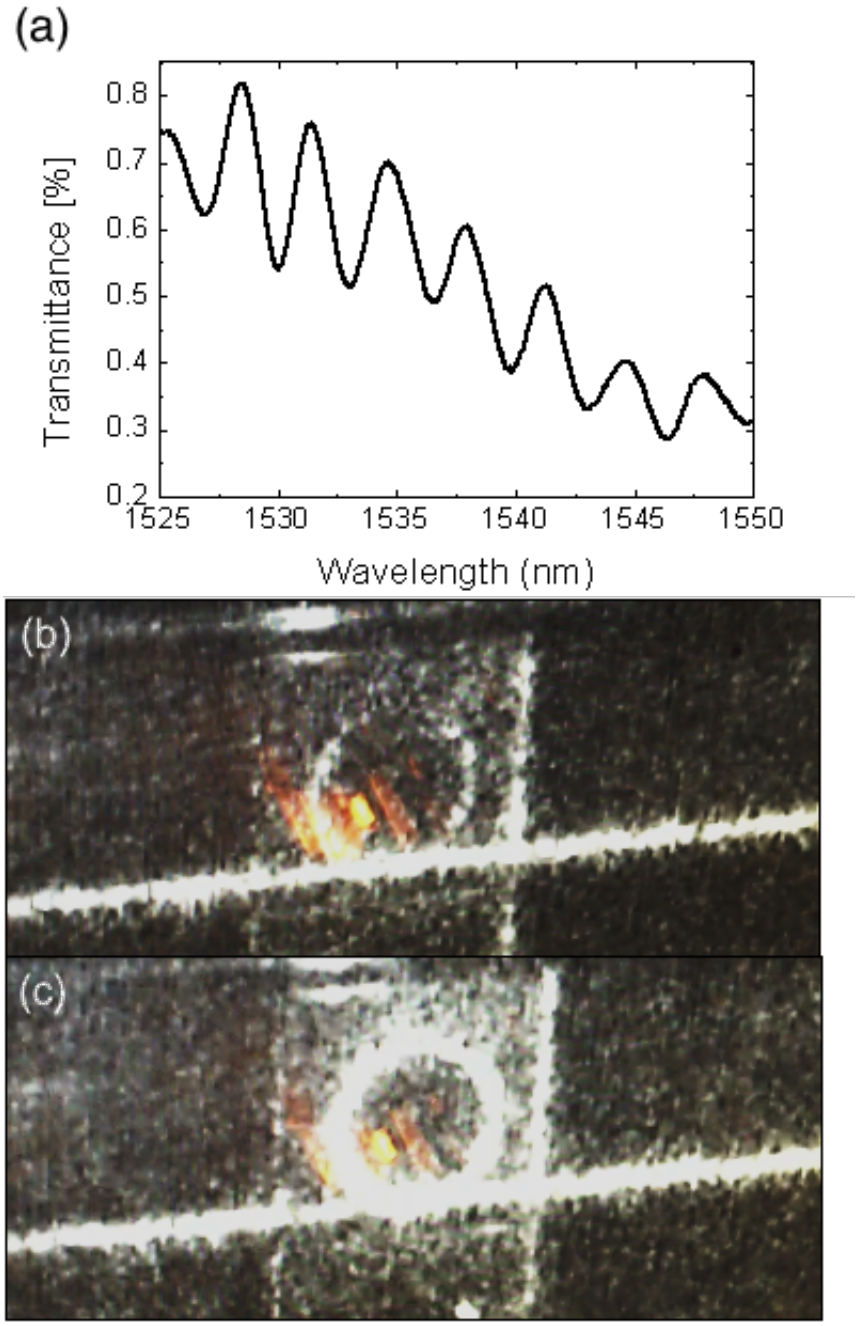

Figure 4.7: a) Transmission spectrum from the ring resonator; b) ring resonator off resonance; c) ring resonator on resonance.

As can be seen from fig. 4.7a, the visibility of the peaks is limited: we attribute this low visibility to the small distance between the ring and the bus waveguide, which is likely to result in a strong over-coupling of the ring resonator. Evidence for this interpretation also comes from Fig. 4.7c: when the light from the channel waveguide resonates with the ring, it can couple into the resonating structure; here, it is scattered in all direction due to the

porosity of the pSi medium, and this appears as the ring resonator lighting up. On the other hand, the ring remains dark when the resonance condition is not satisfied, as shown in fig. 4.7b. This confirms that we are in the presence of a resonant mode inside the ring.

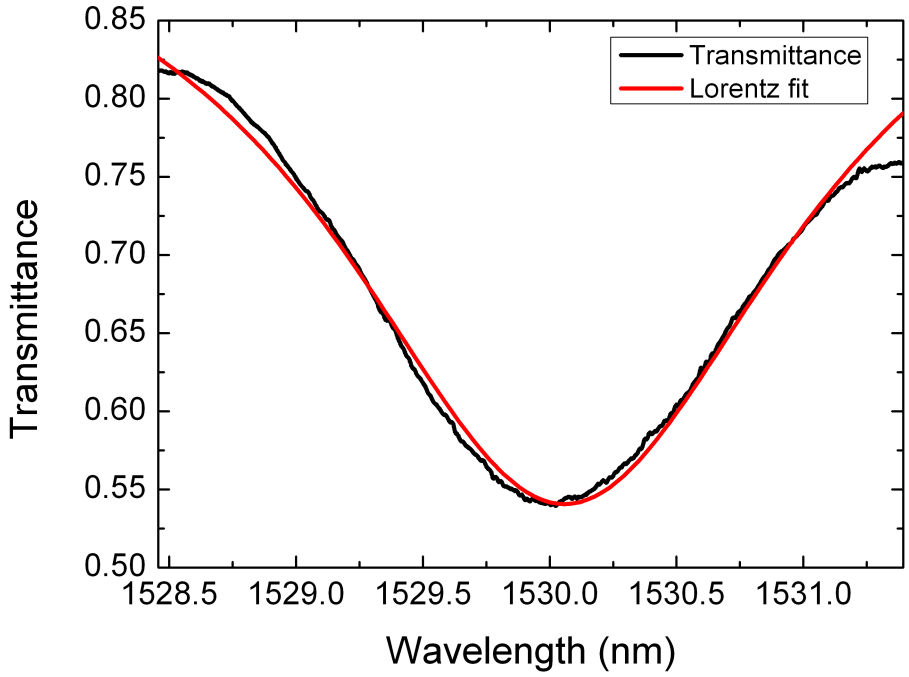

Figure 4.8: Zoom on one of the transmission dips shown in Fig. 4.7. The black solid line represents the transmission, the red solid line is a superimposed Lorentzian fit.

From the experimental transmission plot in fig. 4.7a, we also estimate a free spectral range FSR $\approx 3\ nm$, and from fig. 4.8 we can deduce a quality factor $Q \approx 10^3$. Interestingly, this rather low value of the Q factor was also replicated by means of FDTD calculations where roughness in the pSi matrix was neglected. Thus, the relatively low quality factor is likely to be due to over-coupling or inter-modal cross-talk between the resonating mode and leaky modes supported by the multilayer structures. We believe that a careful optimization of the structure parameters may lead to quality factors as high as 10^4. The maximum experimental value we managed to collect, albeit on a different wavelength range, was $Q \approx 3700$, as shown in fig. 4.9.

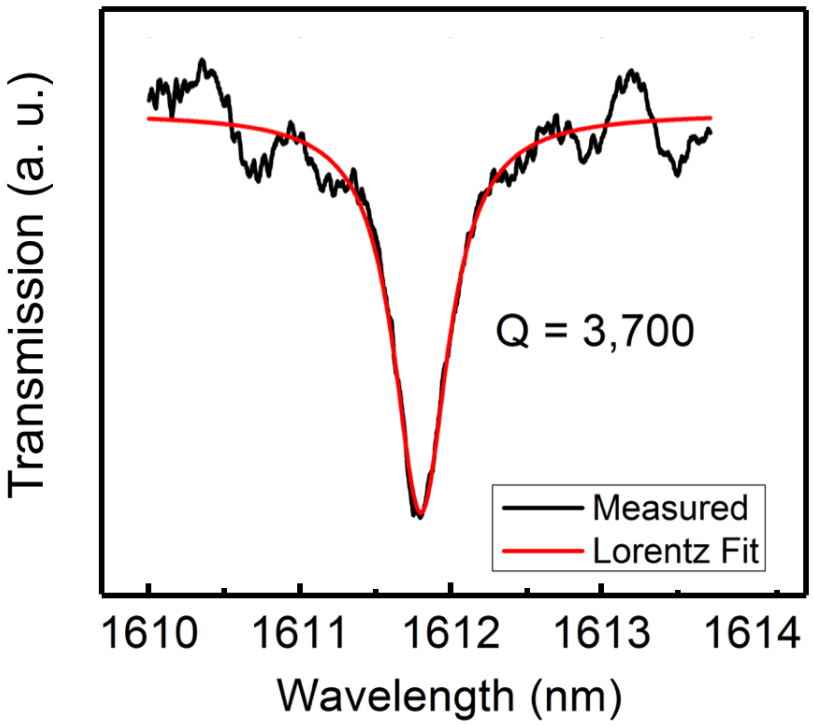

Figure 4.9: Transmission dip on a different wavelength range (black solid) with a superimposed Lorentzian fit (red solid).

To confirm that the features observed in the transmission spectrum correspond to a guided Bloch surface wave, we can estimate the group velocity of the mode guided in the ring resonator from the transmission plot. When the group velocity dispersion (GVD) is negligible[48], the free spectral range of a ring resonator is related to the group velocity v_g according to:

$$\frac{m}{R} = \frac{2\pi}{v_g}\left(\nu_m - \nu_0\right), \tag{4.14}$$

where m is the order of the resonance at frequency ν_m with respect to a reference wavelength $\lambda_0 = 1552.75$ nm ($\nu_0 = 2\pi c/\lambda_0$), and R is the radius of the ring resonator. In figure 4.10, we plot the experimental points corresponding to the resonance order m with respect to a reference resonance at $\nu_0 =$ versus the frequency detuning $\Delta\nu_m = (\nu_m - \nu_0)$. Multiplying eq. (4.14) by the speed of light c makes the formula even wieldier, *i.e.*

$$\frac{cm}{R} = 2\pi n_g\left(\nu_m - \nu_0\right), \tag{4.15}$$

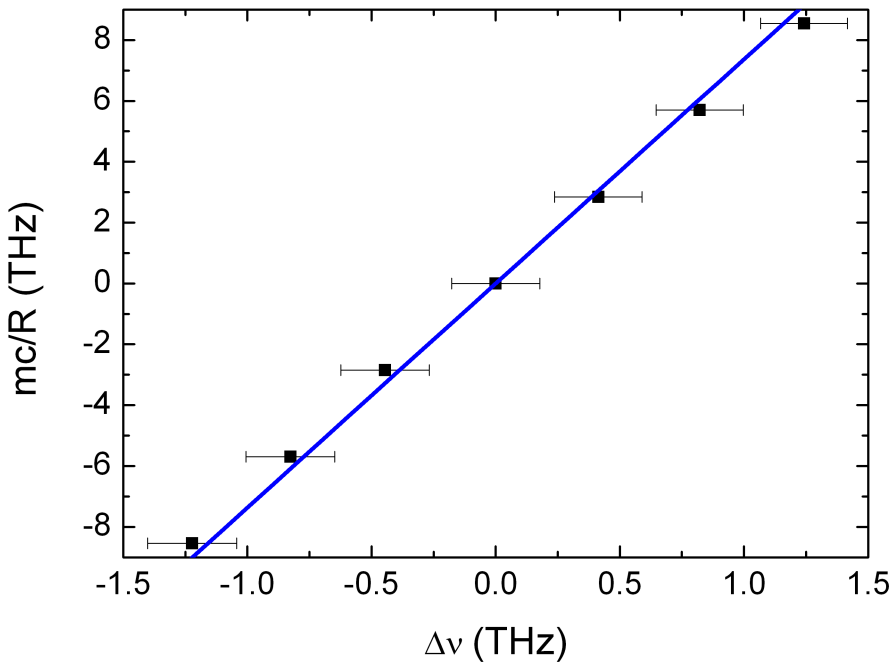

Figure 4.10: Plot of the relation given in equation (4.15) for the experimental points shown in 4.7a. The angular coefficient of the blue line is the theoretical group index n_g evaluated from one-dimensional transfer-matrix theory.

The linear dependence of the resonances on $\Delta\nu_m$ confirms that the GVD is indeed negligible. The horizontal error bars correspond to the full-width-at-half-dip of the transmission resonances. According to eq. (4.15), the slope of the linear fit corresponds to the group index of the guided mode $n_g = c/v_g$. From the experimental data we estimated the value $v_g = 1.967\times10^8$ m/s, which is well comparable to the theoretical value that can be obtained by evaluating the graphical slope of the dispersion relation shown in Fig. 4.5.

4.5 Conclusions

In conclusion, in this chapter we presented the first experimental demonstration of a Bloch surface wave-based ring resonator. The resonator was obtained on a truncated periodic multilayer alternating high- and low-index porous silicon layers. The one-dimensional photonic crystal was designed to have a wide photonic band gap and to support a guided Bloch surface wave in the center of the gap, and porous silicon was selected for the utmost tunability of its refractive index. An experimental quality factor $Q \approx 10^3$ was demonstrated, which, in spite of being still rather small with respect to typical quality factors in ring resonators, still represents an important landmark in the road towards the application of Bloch surface waves in integrated optics.

Chapter 5

BSW nanobeam cavity

In this last chapter, I will present my results on the three-dimensional confinement of Bloch surface waves. We decided to focus on a one-dimensional photonic crystal nanobeam cavity for a series of reasons, essentially related to their design flexibility and the reasonably small footprint. The cavity is localized on top of a one-dimensional photonic crystal that supports Bloch surface waves, and the cavity was designed so that no spurious Fourier component of the electric field would fall inside the light cone. This argument was originally suggested by Akahane et al.[73] in 2003, and is generally known as *Noda's argument*. Our design strategy is based on the effective-index method to reduce the dimensionality of the problem. The resulting structure was tested with two-dimensional FDTD simulations which confirmed a reasonably high quality factor $Q \approx 10^5$.

Some of the calculations summarized in this chapter were developed together with a master student in Physics, dr. Tommaso Perani, and later became part of his master thesis. The results were presented at the 2018 International Conference on Transparent Optical Networks (ICTON) in Bucharest, Romania.

5.1 Motivation

We saw in chapter 2 that Bloch surface waves, after an appropriate optimization of the underlying supporting photonic crystal, have indeed a more intense surface field with respect to simpler TIR-based solutions. This represents an asset in a variety of applications, ranging from BSW-based optical sensing[55, 74, 75] to coupling with quantum objects[8]. In the second scenario, the interaction between a QD575 quantum dot and a one-dimensional photonic crystal was limited to a simple increase in the fluorescence count of the QD575 with respect to the case in which the quantum dot was on a bare glass substrate. In order to move from this unsurprising angular redistribution

of energy to deeper physical effects, including strong coupling, what we need is a strategy to further increase the spatial and temporal overlap between Bloch surface waves and matter. It has already been pointed out in the previous chapter that the best way to enhance the probability of light and matter interacting is to create high-Q optical resonator capable of storing light for many optical cycles[76]. However, it must also be considered that, depending on the physical mechanism one is interested in, the relevant figure that has to be maximized is not just the quality factor Q, but the ratio between Q and the *mode volume* V_{mod}, defined as the three-dimensional upgrade of eq. (2.2), *i.e.*

$$V_{mod} = \frac{1}{[\varepsilon|E|^2]_{max}} \int_{-\infty}^{+\infty} \varepsilon(\mathbf{r})|E(\mathbf{r})|^2 d\mathbf{r}. \tag{5.1}$$

This implies that high-Q optical resonators in which photons are spread out over large modal volumes would still perform badly in terms of the ratio Q/V. The best way to overcome this limitation associated with optical resonators is resorting to photonic crystal cavities, which typically offer quality factors $Q > 10^6$ and wavelength-scale modal volumes. In this chapter, we will present our design strategy and preliminary results regarding a photonic crystal nanobeam cavity for Bloch surface waves.

Nanobeam cavities can be fabricated by starting from a ridge waveguide and patterning it - either via etching or e-beam lithography - in such a way as to create a central cavity surrounded on each side by distributed Bragg reflectors[77]. Many different one-dimensional patterns have been studied: among them, one-dimensional lattices of holes in ridges of variable widths[78, 79], one-dimensional lattices of holes of different sizes[80], one-dimensional lattices of tapered air slits in ridges of fixed thickness[81], etc...

In this region, an adequate tapering profile of the optical thicknesses of the layers can lead to light confinement. The principle governing this behavior was published by S. Noda et al.[73][1]: one must calculate the two-dimensional Fourier transform of the electric field inside the cavity and remove the Fourier components which either lie inside the light cone of the external medium or lie outside the PBG. A consequence of this principle is that the profile of the cavity in terms of optical thicknesses must be *gentle*, as any abrupt modification would call forth undesirable Fourier components. In spite of the simplicity of this argument, the parameter space is still very vast, and finding the proper cavity parameters by trial and error can be a tiresome and time-consuming procedure. Therefore a design algorithm is still necessary to produce high-Q cavities with wavelength-scale modal volumes[82].

5.2 Structural parameters

The structure we have analyzed is shown if fig. 5.1.

[1] Although in their paper the authors referred to two-dimensional photonic-crystal slabs, the argument still holds for different geometries.

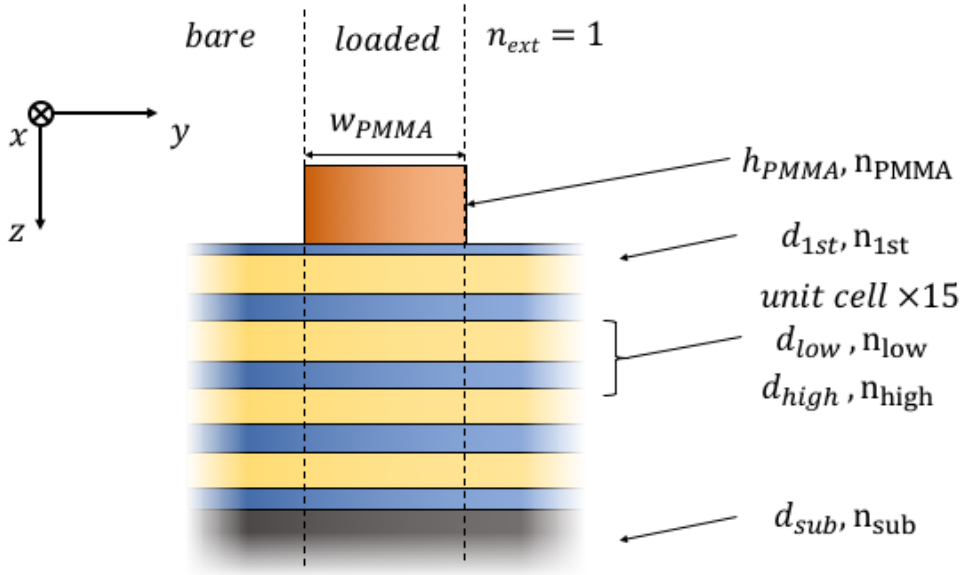

Figure 5.1: Frontal view of the structure under investigation. It consists of a one-dimensional truncated photonic crystal supporting a nanobeam cavity.

The structural parameters were selected so that the work wavelength could be $\lambda = 532$ nm ($E = 2.331$ eV), corresponding to the green line of a Nd:YAG laser, while at the same time maximizing the width of TE-polarized photonic band gap. The layer thicknesses and refractive indices are as follows:

$$d_{1st} = 10 \text{ nm} \tag{5.2}$$
$$n_{Ta_2O_5} = 2.113 \tag{5.3}$$
$$d_{Ta_2O_5} = 93 \text{ nm} \tag{5.4}$$
$$n_{TiO_2} = 1.484 \tag{5.5}$$
$$d_{TiO_2} = 135 \text{ nm}. \tag{5.6}$$

The nanobeam cavity is a ridge made in polymethylmethacrylate (PMMA), and its parameters are

$$n_{PMMA} = 1.48 \tag{5.7}$$
$$d_{PMMA} = 230 \text{ nm} \tag{5.8}$$
$$w_{PMMA} = 1 \ \mu\text{m}. \tag{5.9}$$

The three-dimensional structure appears as shown in fig. 5.2.

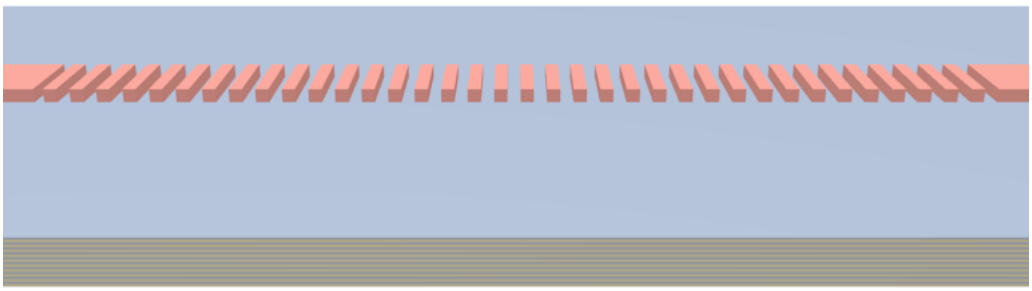

Figure 5.2: Graphical rendition of the three-dimensional nanobeam cavity.

5.3 Theoretical procedure

One of the strengths of nanobeam cavities is their high versatility: they can consist of air holes or air slits with parallel facets; each of these features can be characterized by equal sizes or change according to some pattern; the holes can be placed on a one-dimensional lattice or they can be staggered to create a desired tapering, etc. This versatility, however, entails a series of drawbacks. The parameters space of such complex structures, for example, is considerably vast: among the relevant parameters, we can mention the height of the ridge waveguide, its thickness, the composition of the distributed Bragg reflectors on its sides, etc. Moreover, we must also take into account the parameters of the vertical one-dimensional photonic crystal supporting Bloch surface waves: all the components in the unit cell and the truncation factor. It is then clear that a brute-force optimization based, for example, on fine-tuning the structural parameters and then checking their effects via FDTD simulations would be astoundingly time-consuming.

Thus, our approach proceeded as follows. To start with, we relied on effective-index theory to reduce the dimensionality of the analysis: two dimensional stacks of layers were substituted with a uniform layer of index n_{eff} given by the effective index of the Bloch surface wave we were interested in. This aspect is discussed in subsection 5.3.1. With this approximation, our goal was to enhance the quality factor of the cavity by properly engineering the distribution of the Fourier components in k-space. In a dielectric structure where no material absorption occurs, light only has three possible channels to leak out of the cavity: in-plane leakage can either occur along x, *i.e.* through the side mirrors in the ridge ($Q_{\parallel}^{PBG}$), or along y, where it is confined by total internal reflection due to the refractive index contrast with the surrounding medium ($Q_{\parallel}^{TIR}$); moreover, light can escape along z, *i.e.* by leaking through the vertical multilayer ($Q_{\perp}$). The various contributions to the overall quality

factor are then taken into account as sums of reciprocals:

$$\frac{1}{Q_{tot}} = \frac{1}{Q_{\perp}} + \frac{1}{Q_{\parallel}^{TIR}} + \frac{1}{Q_{\parallel}^{PBG}}. \tag{5.10}$$

Of the three terms, $Q_{\parallel}^{PBG}$ is the most tractable, as the amount of light leaking through the distributed Bragg reflector along the ridge, *i.e.* in the x direction, can be reduced by simply increasing the number of unit cell repetitions. In our simulations, we noticed that a value $N_{DBR} > 15$ was sufficient to reduce this contribution. As to $Q_{\perp}$, this comes from the fact that we are dealing with Bloch surface waves, which require a supporting truncated periodic multilayer. However, the photonic band gap from this photonic crystal does not extend indefinitely in k space, but only between the upper and lower band edges relative to the reference energy, k_{UBE} and k_{LBE}, respectively. Wave vector components smaller than k_{UBE} or greater than k_{LBE} will not be confined, and will thus couple to the radiative modes and leak away from the cavity. $Q_{\parallel}^{TIR}$, the last term in eq. (5.10), depends on the amount of radiation whose wave vector component is less than that of the light line of the external medium ($k_{LL} = \omega/c \cdot n$): for three-dimensional structures, these are said to lie within the *light cone* of this medium[83]. In order to maximize the quality factor, one must then design the cavity in such a way that the field profile in real space has no Fourier components localized in the region below $max(k_{ext}, k_{UBE})$ and above k_{LBE}, where k_{ext} is the light line of the external medium.

It has been shown by Noda et al.[73] that the amount of these unconfined Fourier components can be minimized if the in-cavity field profile changes "smoothly" across the cavity, without abrupt changes. This principle was first introduced in the field of double-heterostructure nanocavities by the same authors[18], and was later applied to photonic crystal nanocavities by Notomi et al.[84]. Once the in-cavity field has been worked out, via transfer-matrix theory, rigorous coupled-wave analysis or otherwise, many techniques are available to calculate the Fourier transform (FT) of the field; in section 5.3.2 we show how the FT can be calculated starting from the knowledge of the field amplitudes in each layer. The strategy that seems to better fulfill the goal of attracting most Fourier components in the range $\max(k_{ext}, k_{LBE}) < k < k_{UBE}$ is to modulate the thicknesses of the in-cavity ridges according to a parabolic law[85]. In section 5.3.3 we will inquire into this aspect and try and understand its origin. Finally, in the last section we propose a step-by-step approach of our design algorithm.

In the following subsections, we relate on various aspects of the approaches we relied on in our analysis.

5.3.1 Effective-index theory

As has already been discussed in the previous chapters, the structure can be divided in the *loaded* region, which supports the ridge, and the *bare* region,

where the PMMA ridge has already been etched. Plotted in fig. 5.3a and b we can see the Bloch surface waves supported by the two photonic crystals.

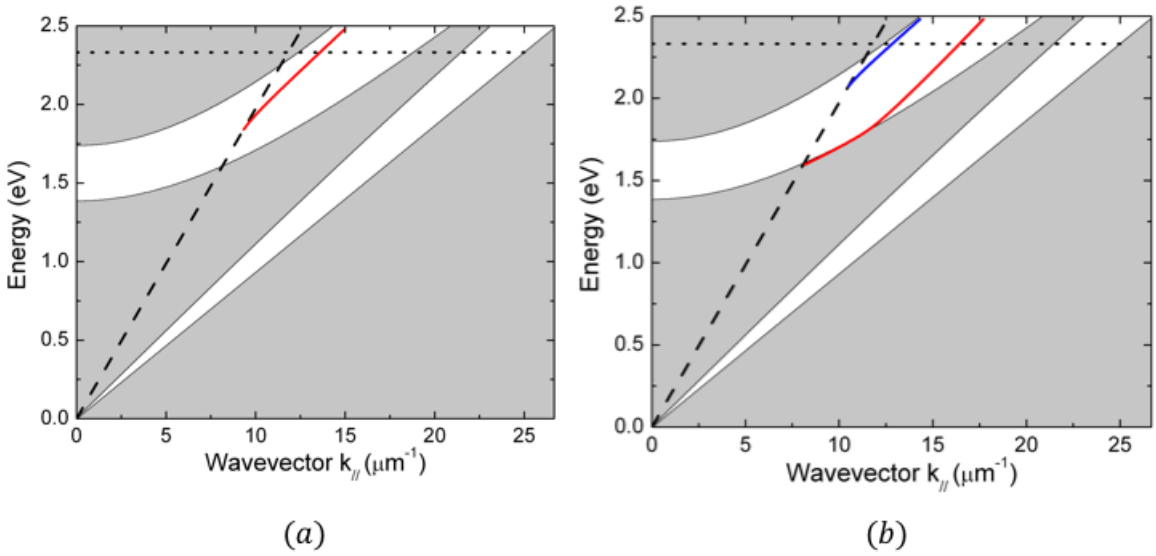

Figure 5.3: (a) The Bloch surface wave supported by the bare structure; at the energy of interest, $k_{bare} = 13.60\ \mu\text{m}^{-1}$ (b) The modes supported by the loaded structure. For the upper Bloch surface wave, $k_{load} = 16.43\ \mu\text{m}^{-1}$. The black dashed line is the light line of the external medium (air: $n_{ext} = 1$), and the black dotted line represent the work wavelength $\lambda_0 = 532$ nm ($E \approx 2.33$ eV).

The *bare* and *loaded* Bloch surface waves at the work wavelength $\lambda_0 = 532$ nm fall at $k_{bare} = 13.60\ \mu\text{m}^{-1}$ and $k_{load} = 16.43\ \mu\text{m}^{-1}$, respectively, and correspond to the effective indices

$$n_{load} = 1.391 \tag{5.11}$$
$$n_{bare} = 1.152. \tag{5.12}$$

The Bloch surface wave mode profiles are plotted in fig. 5.4.

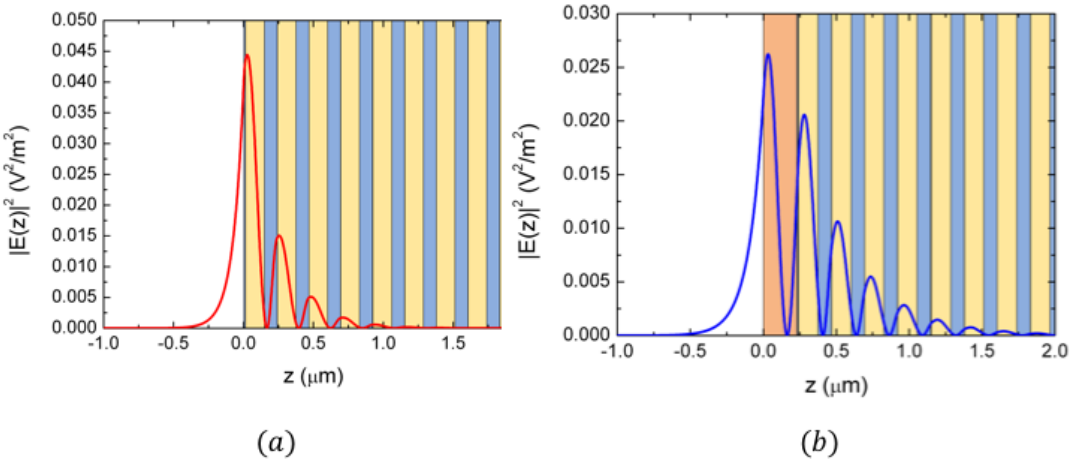

Figure 5.4: (a) Square modulus of the electric field of the Bloch surface wave supported by the bare structure; at the energy of interest, $k_{bare} = 13.60\ \mu\text{m}^{-1}$ (b) Square modulus of the electric field of the Bloch surface wave supported by the loaded structure. For the upper Bloch surface wave in fig. (5.3), $k_{load} = 16.43\ \mu\text{m}^{-1}$.

5.3.2 Fourier transforms

The electric field in the j-th layer can be written as

$$E_j(z) = E_j^+ e^{iw_j z} + E_j^- e^{-iw_j z}, \tag{5.13}$$

where, as usual, the transversal wave vector component is defined as

$$w_j = \sqrt{(2\pi n_j/\lambda_0)^2 - \beta^2}. \tag{5.14}$$

The whole mode profile can then be recovered by summing all the contributions due to each layer given by eq. (5.13), with adequate characteristic functions. The Fourier transform of the field is then given by

$$\hat{E}(k) = \int_{-\infty}^{+\infty} E(z) e^{-i2\pi kz} dz \approx \tag{5.15}$$

$$\approx \sum_j \int_j E_j(z) e^{-i2\pi kz} dz \tag{5.16}$$

This corresponds to $E_j(z') = E_j^+ e^{iwz'} + E_j^- e^{-iwz'}$, where $0 < z' < d_j$. In other terms, $z' = z - \sum_j d_j$, so that the variable can actually roam only in the region between $[0; d_j]$. With the new notation, we have

$$\hat{E}(k) = \sum_j \int_{z_j}^{z_{j+1}} \left(E_j^+ e^{iwz'} + E_j^- e^{-iwz'} \right) e^{-i2\pi kz} dz =$$

$$= \sum_j \int_{z_j}^{z_{j+1}} \left(E_j^+ e^{iw\left(z - \sum_j d_j\right)} + z_j e^{-iw\left(z - \sum_j d_j\right)} \right) e^{-i2\pi kz} dz$$

Let us now make a variable change $z \to z'$, so that $dz = dz'$, $z = z' + \sum_j d_j$ and the extrema become $z_j \to 0$ and $z_{j+1} \to d_j$:

$$
\begin{aligned}
\hat{E}(k) &= \sum_j \int_0^L \left(E_j^+ e^{iwz'} + E_j^- e^{-iwz'} \right) e^{-i2\pi k \left(z' + \sum_n^j d_n \right)} dz' = \\
&= \sum_j \int_0^L \left(E_j^+ e^{iwz'} + E_j^- e^{-iwz'} \right) e^{-i2\pi k z'} e^{-i2\pi k \sum_n^j d_n} dz' = \\
&= \sum_j e^{-i2\pi k \sum_n^j d_n} \int_0^L \left(E_j^+ e^{iwz'} e^{-i2\pi k z'} + E_j^- e^{-iwz'} e^{-i2\pi k z'} \right) dz' = \\
&= \sum_j e^{-i2\pi k \sum_n^j d_n} \int_0^L \left(E_j^+ e^{i(w-2\pi k)z'} + E_j^- e^{-i(w+2\pi k)z'} \right) dz' = \\
&= \sum_j e^{-i2\pi k \sum_n^j d_n} \left(E_j^+ \int_0^L e^{i(w-2\pi k)z'} dz' + E_j^- \int_0^L e^{-i(w+2\pi k)z'} dz' \right) = \\
&= \sum_j e^{-i2\pi k \sum_n^j d_n} \left(\frac{E_j^+}{i\,(w-2\pi k)} \, e^{i(w-2\pi k)z'} \Big|_0^L + \frac{E_j^-}{-i\,(w+2\pi k)} \, e^{-i(w+2\pi k)z'} \Big|_0^L \right) = \\
&= \sum_j e^{-i2\pi k \sum_n^j d_n} \left(\frac{E_j^+}{i\,(w-2\pi k)} \left(e^{i(w-2\pi k)L} - 1 \right) + \frac{E_j^-}{-i\,(w+2\pi k)} \left(e^{-i(w+2\pi k)L} - 1 \right) \right) = \\
&= \sum_j e^{-i2\pi k \sum_n^j d_n} \left(-i \frac{E_j^+}{w-2\pi k} \left(e^{i(w-2\pi k)L} - 1 \right) + i \frac{E_j^-}{w+2\pi k} \left(e^{-i(w+2\pi k)L} - 1 \right) \right).
\end{aligned}
$$

Likewise for the complex conjugate of the field, *i.e.* $\bar{E}_j(z') = E_j^{+,*} e^{-iwz'} + E_j^{-,*} e^{iwz'}$, where w is not conjugated because, in the scenario we are interested

in, we are above the light line of each component medium.

$$\hat{\bar{E}}(k) = \sum_j \int_0^L \left(E_j^{+,*} e^{-iwz'} + E_j^{-,*} e^{iwz'} \right) e^{-i2\pi k \left(z' + \sum_n^j d_n \right)} dz' = \tag{5.17}$$

$$= \sum_j \int_0^L \left(E_j^{+,*} e^{-iwz'} + E_j^{-,*} e^{iwz'} \right) e^{-i2\pi k z'} e^{-i2\pi k \sum_n^j d_n} dz' = \tag{5.18}$$

$$= \sum_j e^{-i2\pi k \sum_n^j d_n} \int_0^L \left(E_j^{+,*} e^{-iwz'} e^{-i2\pi k z'} + E_j^{-,*} e^{iwz'} e^{-i2\pi k z'} \right) dz' = \tag{5.19}$$

$$= \sum_j e^{-i2\pi k \sum_n^j d_n} \int_0^L \left(E_j^{+,*} e^{i(-w-2\pi k)z'} + E_j^{-,*} e^{i(w-2\pi k)z'} \right) dz' = \tag{5.20}$$

$$= \sum_j e^{-i2\pi k \sum_n^j d_n} \left(E_j^{+,*} \int_0^L e^{-i(w+2\pi k)z'} dz' + E_j^{-,*} \int_0^L e^{i(w-2\pi k)z'} dz' \right) = \tag{5.21}$$

$$= \sum_j e^{-i2\pi k \sum_n^j d_n} \left(\frac{E_j^{+,*}}{-i\,(w+2\pi k)} \, e^{-i(w+2\pi k)z'} \Big|_0^L + \frac{E_j^{-,*}}{i\,(w-2\pi k)} \, e^{i(w-2\pi k)z'} \Big|_0^L \right) = \tag{5.22}$$

$$= \sum_j e^{-i2\pi k \sum_n^j d_n} \left(\frac{E_j^{+,*}}{-i\,(w+2\pi k)} \left(e^{-i(w+2\pi k)L} - 1 \right) + \frac{E_j^{-,*}}{i\,(w-2\pi k)} \left(e^{i(w-2\pi k)L} - 1 \right) \right) = \tag{5.23}$$

$$= \sum_j e^{-i2\pi k \sum_n^j d_n} \left(i \frac{E_j^{+,*}}{w+2\pi k} \left(e^{-i(w+2\pi k)L} - 1 \right) - i \frac{E_j^{-,*}}{w-2\pi k} \left(e^{i(w-2\pi k)L} - 1 \right) \right) \tag{5.24}$$

Thus, all in all, since $\Re[E(z)] = \frac{1}{2}\left(E(z) + \bar{E}(z)\right)$, the overall Fourier trans-

form is given by the following expression.

$$\hat{E}(k) = \frac{1}{2}\left(\hat{E}(k) + \hat{\tilde{E}}(k)\right) = \tag{5.25}$$

$$= \frac{1}{2}\sum_j e^{-i2\pi k\sum_n^j d_n}\left(-i\frac{E_j^+}{w-2\pi k}\left(e^{i(w-2\pi k)L}-1\right) + i\frac{E_j^-}{w+2\pi k}\left(e^{-i(w+2\pi k)L}-1\right)\right) + \tag{5.26}$$

$$+ \frac{1}{2}\sum_j e^{-i2\pi k\sum_n^j d_n}\left(i\frac{E_j^{+,*}}{w+2\pi k}\left(e^{-i(w+2\pi k)L}-1\right) - i\frac{E_j^{-,*}}{w-2\pi k}\left(e^{i(w-2\pi k)L}-1\right)\right) = \tag{5.27}$$

$$= \frac{1}{2}\sum_j e^{-i2\pi k\sum_n^j d_n}\left\{-i\left(E_j^+ + E_j^{-,*}\right)\frac{e^{i(w-2\pi k)L}-1}{w-2\pi k} + i\left(E_j^- + E_j^{+,*}\right)\frac{e^{-i(w+2\pi k)L}-1}{w+2\pi k}\right\}. \tag{5.28}$$

5.3.3 In-cavity tapering

Consider a quarter-wavelength stack whose unit cell is formed by two layers of index n_1, n_2 and thicknesses

$$d_1 = \frac{\lambda_0}{4n_1} \tag{5.29}$$

$$d_2 = \frac{\lambda_0}{4n_2}. \tag{5.30}$$

The Bloch wave vector at the center of the PBG, as derived in eq. (A.69), can be shown to be[48]

$$q = \frac{\pi}{\Lambda} + i\frac{\Delta n}{n\Lambda}. \tag{5.31}$$

Thus, a plane wave travelling inside the band gap would propagate as

$$E(x) \propto \cos(\frac{\pi}{\Lambda}x)e^{-\frac{\Delta n}{n\Lambda}|x|} \propto \cos(\frac{\pi}{\Lambda}x)e^{-\gamma|x|}, \tag{5.32}$$

and its Fourier transform can be easily shown to consist of two Lorentzian contributions

$$\hat{E}(k) \propto \frac{\gamma}{(k \pm \frac{\pi}{\Lambda})^2 + \gamma^2}. \tag{5.33}$$

As could have been guessed from the form of the field in eq. (5.32), the Fourier transform has two sharp contributions centred at $k = \mp\frac{\pi}{\Lambda})^2$, with a FWHM proportional to $\gamma = \frac{\Delta n}{n\Lambda}$. The width of these peaks, which is ultimately due to the sharpness of the decay in real space, depends on structural parameters of the quarter-wavelength stack which cannot be tuned. On the other hand, a looser confinement in real space could be assumed to shrink the k-space

distribution. In the presence of a Gaussian envelope function for the electric field, *i.e.*

$$E(x) \propto \cos(\frac{\pi}{\Lambda}x)e^{-\frac{x^2}{2\sigma^2}}, \tag{5.34}$$

would lead to a Gaussian Fourier transform such as

$$\hat{E}(k) \propto \frac{\sigma}{2}e^{-\frac{\sigma^2}{2}(k\pm\frac{\pi}{\Lambda})^2}. \tag{5.35}$$

Eq. (5.35), as in eq. (5.33), has two contributions at $k = \pm\frac{\pi}{\Lambda}$, but the width of the peaks in this case is inversely proportional to the standard deviation σ: the peaks can now be shrunk by increasing the slackness of the envelope function of the electric field in real space. This observation led Noda et al. to the first in-plane Fourier transform-based design algorithm for photonic crystal nanocavities[73]. Furthermore, by comparing eq. (5.35) and eq. (5.32), one notices that the decay rates can be equated by assuming an imaginary part of the Bloch wave vector equal to $\gamma = x/(2\sigma^2)$.

But what specific kind of tapering profile could give rise to such an electric field distribution? It is clear, by analogy with potential wells in semiconductor heterostructures, that the lattice constant must shrink as one gets closer to the centre: as the period Λ shrinks, the photonic band gap of the shrunk structure is blue-shifted proportionally. This forms the optical analogue of a potential well for electrons. Expanding the dispersion relation $\omega(k)$ around the band edge $k = \pm\frac{\pi}{\Lambda}$, one gets, up to second order,

$$\omega = \omega(\pi/\Lambda) + a(k - \pi/\Lambda)^2, \tag{5.36}$$

where the coefficient $a < 0$ due to the negative curvature of the dispersion relation close to this point. Symmetry also forbids odd powers from showing in the Taylor expansion. This dispersion relation can be turned into a complex one by substituting $k = \pi/\Lambda + i\gamma$ to get $\omega = \omega_{LBE} - a\gamma^2$. A little algebra then leads to

$$\omega_{LBE}(x) = \omega + a\left(\frac{x}{2\sigma^2}\right)^2 = \tag{5.37}$$

$$= \omega(1 - \alpha x^2), \tag{5.38}$$

where $\alpha = -a/(4\omega\sigma^4) > 0$ due to the curvature of the band being negative. Altogether, the lower band edge of the photonic band gap at the centre of the cavity can be blue shifted by reducing the lattice constant according to $\Lambda(x) = \Lambda/(1 - \alpha x^2)$. If $\alpha x^2 \ll 1$, then the fraction can be Taylor expanded into

$$\Lambda(x) = \Lambda(1 + \alpha x^2). \tag{5.39}$$

which links the in-cavity lattice constants to that of the DBR stack out of the cavity via a quadratic dependency.

5.3.4 Optimal tapering parameters

In order to induce an optical resonance inside the cavity, we designed a quadratic tapering of the thicknesses of each ridge block. It has been shown elsewhere that such a tapering creates an in-cavity electric field distribution with a Gaussian profile. Thus, starting from the central end of the lateral Bragg reflectors, we shrank the period according to the relation

$$\Lambda_j = \Lambda_0 \left[1 + \alpha \left(\frac{j}{N_{taper}} \right)^2 \right], \tag{5.40}$$

where the index $j \in [-N_{taper}, \cdots, N_{taper}]$ and Λ_0 is the period at the centre of the cavity, corresponding to $j = 0$. To enforce continuity of the layer thicknesses between the lateral DBR and the cavity, one must have

$$\Lambda_{j=N_{taper}} = \Lambda_{DBR}, \tag{5.41}$$

which leads to an equation for the attenuation coefficient α, *i.e.*

$$\alpha = -1 + \frac{\Lambda_{DBR}}{\Lambda_0}. \tag{5.42}$$

As a consequence, the minimum ridge period at the center of the cavity equals

$$\Lambda_0 = \frac{\Lambda_{DBR}}{\alpha + 1}. \tag{5.43}$$

The parameters α and N_{taper} define the height and width of the optical potential well, respectively, and can in principle be chosen arbitrarily. However, we chose to obtain at least a rough estimate of these parameters with some physical insight in the confinement mechanism. Scaling the lattice constant $\Lambda_{DBR} \to \Lambda_0$ leads to a shift of the bandgap upward in energy. Therefore, we may assume that a good criterion to obtain a tight confinement of light occurs when the lower band edge of the PBG lies in the centre of the photonic band gap caused by the lateral DBRs. In terms of angular frequency, this can be translated as

$$\omega_{LBE}^{centre} = \omega_{DBR}^{mid-gap}. \tag{5.44}$$

The mid-gap angular frequency of the first-order photonic band gap due to a 1D PhC of period Λ_0 and alternating layers of indices n_1 and n_2 can be shown[86] to be

$$\omega_{mid} = \frac{2\pi c}{\Lambda_0} \frac{n_1 + n_2}{4 n_1 n_2}. \tag{5.45}$$

When the refractive index contrast is reasonably weak, *i.e.* $\Delta n = |n_1 - n_2| \ll n$, with n being the average refractive index, $n = (n_1 + n_2)/2$, the mid-gap frequency can be simplified to

$$\omega_{mid} = \frac{\pi c}{n \Lambda_0}. \tag{5.46}$$

Solving the gap condition in eq. (A.60) yields an approximation for the width of the gap, *i.e.*

$$\Delta\omega = \omega_{mid}\frac{4}{\pi}\frac{|n_1 - n_2|}{n_1 + n_2} \approx \omega_{mid}\frac{2\Delta n}{\pi n}, \tag{5.47}$$

Plugging this relation in eq. (5.44), we can then write

$$\omega_{LBE}^{centre} = \omega_{DBR}^{centre} - \frac{\Delta\omega_{mid}}{2} = \tag{5.48}$$

$$= \omega_{DBR}^{centre}\left(1 - \frac{\Delta\omega_{mid}}{2\omega_{DBR}^{centre}}\right) \approx \tag{5.49}$$

$$\approx \frac{\pi c}{n\Lambda_0}\left(1 - \frac{\Delta n}{n\pi}\right) \tag{5.50}$$

By comparison, the centre (angular) frequency in the PBG of a one-dimensional photonic crystal of period Λ_{DBR} would be, according to eq. (5.46),

$$\omega_{mid} = \frac{\pi c}{n\Lambda_{DBR}}. \tag{5.51}$$

Thus, equating eq. (5.50) and eq. (5.51) yields the optimal ratio between the periods, *i.e.*

$$\frac{\Lambda_0}{\Lambda_{DBR}} \approx 1 - \frac{\Delta n}{n\pi}. \tag{5.52}$$

This approximate equation can then be exploited to estimate the shrinking parameter α given in eq. (5.42), *i.e.*

$$\alpha = -1 + \left(1 - \frac{\Delta n}{n\pi}\right)^{-1}. \tag{5.53}$$

5.3.5 Step-by-step approach

Thus, we tried to simplify the analysis by resorting to effective-index theory, thereby reducing the dimensionality of the system. The effective-index method has already been succesfully applied in the context of guided Bloch surface waves in ridges[13], therefore it is surely reliable even in the context under scrutiny. From this point on, we followed the following steps:

- We divided the structure in two regions, as shown in fig. 5.1: the *loaded* region, which supports the ridge waveguide, and the *bare* region, in which the ridge has been etched away. For each of these regions, we calculated the wave vector component $k_\parallel$ of the Bloch surface waves: the results were $k_{bare} = 13.60\ \mu\text{m}^{-1}$ and $k_{load} = 16.43\ \mu\text{m}^{-1}$, corresponding the effective indices $n_{load}^{eff} = 1.391$ and $n_{bare}^{eff} = 1.152$.

- To take into account lateral confinement of the BSW, the ridge was substituted with the effective index of the TM0 mode supported by a

symmetrical slab waveguide of core index n_{load}^{eff} surrounded by two semi-infinite media of refractive index n_{bare}^{eff}. The result is depicted in fig. 5.5.

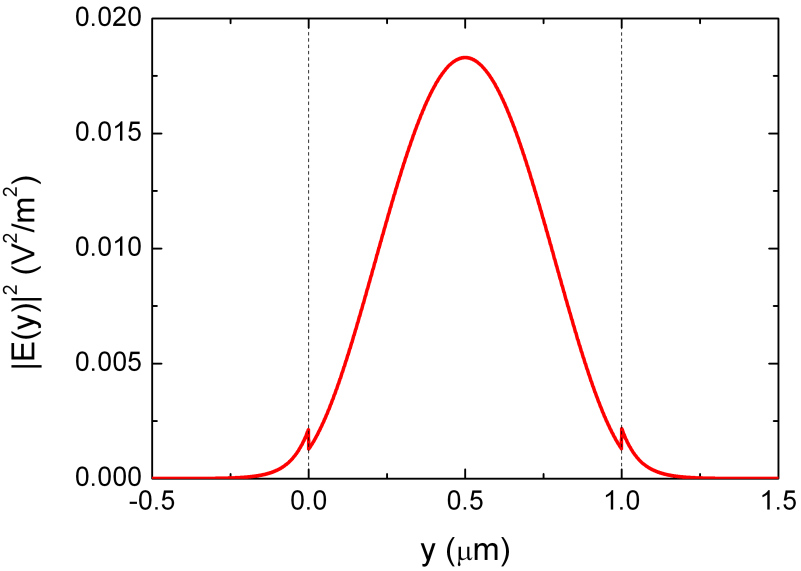

Figure 5.5: Mode profile of the TM0 mode supported by a symmetric slab waveguide of core index n_{load}^{eff} and cladding index n_{load}^{eff}. The mode is found at $k_{\parallel} = 16.204\ \mu\text{m}^{-1}$, corresponding to an effective index $n_{TM0}^{eff} = 1.372$.

- For top-view simulations, the lateral mirrors in the ridge waveguide are formed by stacking alternating *loaded* layers of index $n_{TM0}^{eff} = 1.372$ and *bare* layers of index $n_{bare}^{eff} = 1.152$ in the x direction. The widths of the mirrors are given by the quarter-wavelength condition:

$$d_{load} = \frac{\lambda_0}{4n_{TM0}^{eff}} \approx 97 \text{ nm} \tag{5.54}$$

$$d_{bare} = \frac{\lambda_0}{4n_{bare}^{eff}} \approx 115 \text{ nm}. \tag{5.55}$$

  The period of the DBR is

$$\Lambda_{DBR} = \frac{\lambda_0}{4}\left(\frac{1}{n_{TM0}^{eff}} + \frac{1}{n_{bare}^{eff}}\right) \tag{5.56}$$

- The tapering in the central region consists of a quadratic shrinking of the lattice constant. The shrinking was achieved with the following relation:

$$\Lambda_j = \Lambda_{DBR}\left[1 + \alpha\left(\frac{j}{N_{taper}}\right)\right], \tag{5.57}$$

The shrinking parameters we selected were $N_{DBR} = 20$, $N_{taper} = 15$ and $\alpha = 8.05 \times 10^{-2}$.

- The resulting multilayer was simulated using the transfer-matrix method reported in appendix A. The transmission spectrum is shown in fig. 5.6.

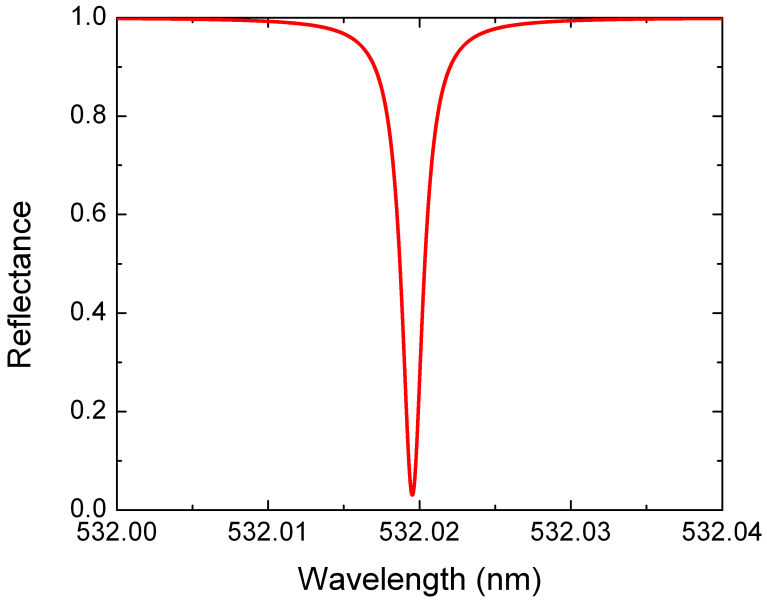

Figure 5.6: Reflectance spectrum along y (top-view) of a nanobeam cavity formed by a quarter-wavelength stack of alternating n_{GBSW} and n_{bare} indices with a parabolic in-cavity thickness profile. A dip in the reflectance can be seen for $\lambda \approx \lambda_0 = 532.0$ nm.

The FWHM estimated from figure 5.6 is $FWHM = 6.973 \times 10^{-6}$ nm, which yields a 1D quality factor

$$Q_{TM} = \lambda_0 / FWHM \approx 7.6 \times 10^7. \tag{5.58}$$

The square modulus of the electric field inside the cavity can be evaluated at normal incidence by setting the energy equal to the reflectance minimum and running. The result is shown in fig. 5.7.

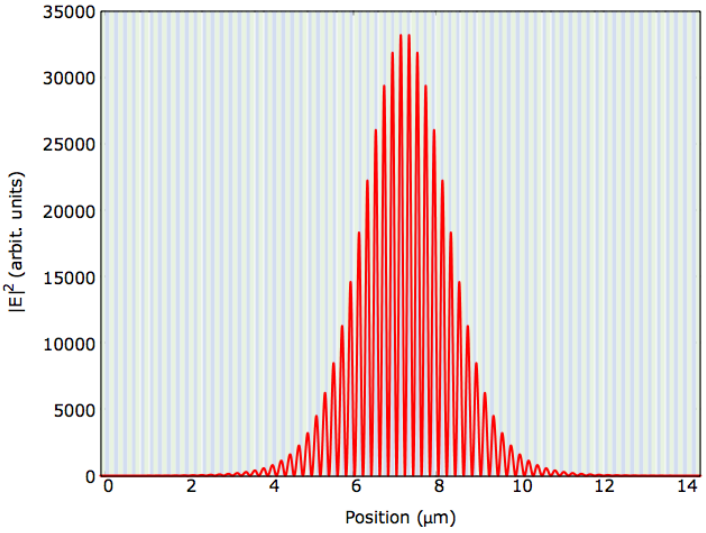

Figure 5.7: Square modulus of the electric field along the x direction.

- At this point, one can calculate the Fourier transform of the electric field profile either directly via the coefficient obtained via the transfer matrix approach, with the method outlined in section 5.3.2, or with any numerical Fast Fourier Transform (FFT) algorithm. The result is plotted in figure 5.8.

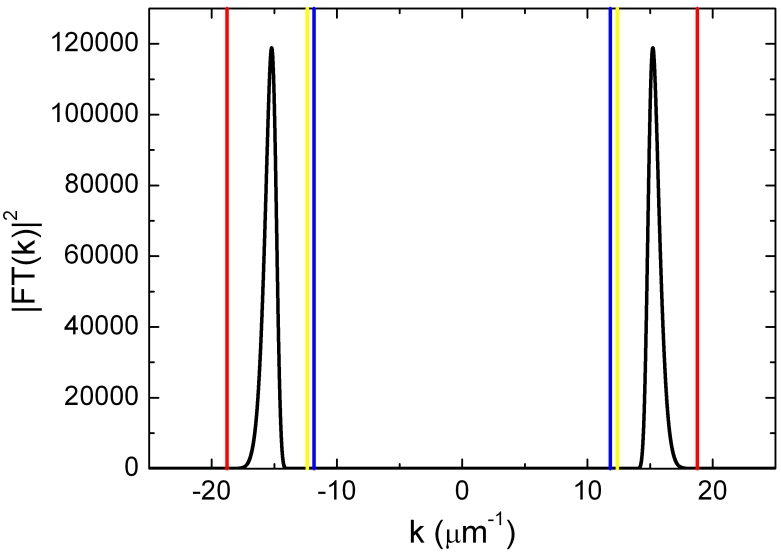

Figure 5.8: Fourier transform of the real part of the in-cavity electric field. The yellow and red lines correspond to the upper and lower band-edge in fig. 5.9, respectively. The blue line represent the light line of the external medium.

The vertical lines plotted in fig. 5.8 correspond to the boundaries of each confinement mechanism: the light line of the external medium falls at $k_{ext} = 11.83\ \mu\text{m}^{-1}$, the upper and lower band-edges fall at $k_{UBE} = 12.38\ \mu\text{m}^{-1}$ and $k_{LBE} = 18.78\ \mu\text{m}^{-1}$, respectively. As can be seen, with the approach outlined in this chapter most of the Fourier components fall below the lightcone[83].

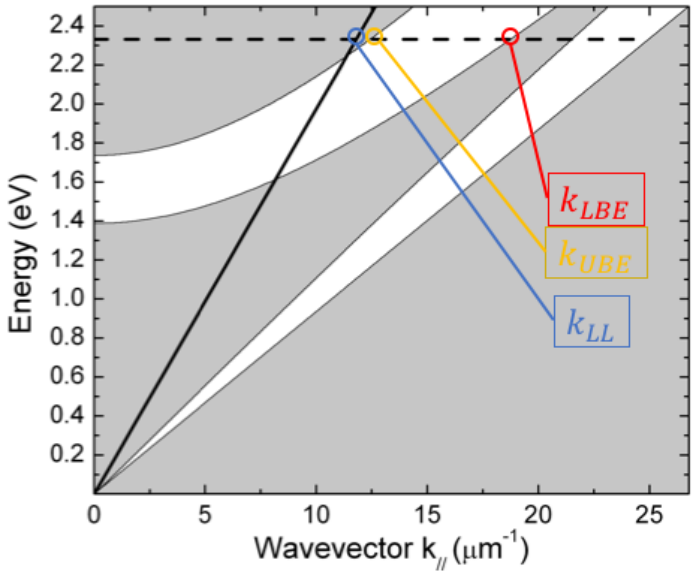

Figure 5.9: Magnified view of the photonic band gap around the energy of interest, $E = 2.331$ eV ($\lambda_0 = 532$ nm). The boundaries of both total internal reflection and PBG confinement are highlighted: $k_{ext} = 11.83\ \mu\text{m}^{-1}$, $k_{UBE} = 12.38\ \mu\text{m}^{-1}$ and $k_{LBE} = 18.78\ \mu\text{m}^{-1}$.

- Eventually the structure is analyzed via Meep (`https://meep.readthedocs.io/en/latest/`), the Massachusetts Institute of Technology's own ab-initio FDTD software. A full-fledged explanation of the FDTD procedure shall not be given here, as it would lead us astray from the central topic of this thesis; a thorough discussion on this topic can however be found, for example, in [87] and [88]. The results are reported in the next section.

5.4 Results and discussion

In order to test the validity of our approach, we ran two two-dimensional simulations for the structure under scrutiny: a *top-view* simulation and a *side-view* simulation. In both cases, we relied on effective-index theory to compute the proper effective indices for the two views.

The result of the side-view simulation in Meep is reported in fig. 5.10.

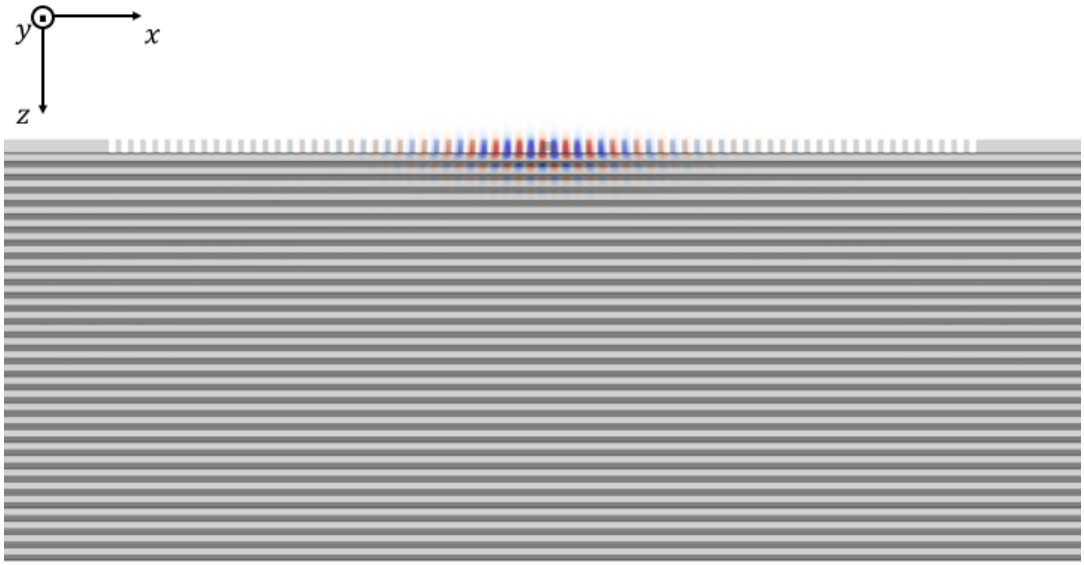

Figure 5.10: Side-view simulation of the BSW nanobeam cavity. The field is confined in the center of the cavity.

Harmonic analysis yielded a mode at $\tilde{\nu} = 1.863\ \mu\text{m}^{-1}$, corresponding to $\lambda_{side} \approx 537$ nm, with a quality factor $Q_{side} \approx 9.4 \times 10^4$.

The result of the top-view simulation is shown in picture 5.11.

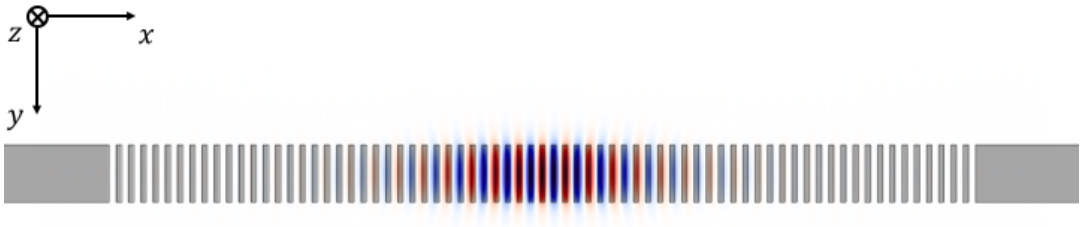

Figure 5.11: Top-view simulation of the BSW nanobeam cavity. The field is confined in the center of the cavity.

In this case, Meep found a slightly detuned mode at $\tilde{\nu} = 1.862\ \mu\text{m}^{-1}$, corresponding to $\lambda_{side} \approx 537$ nm, with a the FDTD quality factor was $Q_{top} \approx 9.5 \times 10^4$.

Unfortunately, our approach does not allow for a straightforward evaluation of the mode volume of the in-cavity mode. One-dimensional mode lengths can be promptly evaluated by semi-analytical or, if needs be, numerical integration of the mode profiles shown in the previous section, *i.e.* fig. 5.7, fig. 5.5 and fig. 5.4, by sequentially applying the definition given in eq. (A.74). This would

yield independent modal lengths L_x, L_y and L_z. However, it is clear that $V_{mod} \neq L_x L_y L_z$, and the relationship between these figures and the modal volume V_{mod} is unclear and, most likely, inconsistent. Thus, a full-fledged evaluation of the mode volume calls for a thorough three-dimensional FDTD simulation. What can be done is a rough estimation of the *mode size* by estimating the FWHM of the two-dimensional FDTD simulations given by fig. 5.10, fig. 5.11, etc. In this way, a figure such as $V_{mod} \approx 4\ \mu m^3$ can be obtained. By comparison, this is much smaller than the typical modal volume for a ring resonator, which roughly speaking amounts to an effective modal area, *i.e.* the transverse mode supported by the looping ridge, multiplied by the length of the circumference, which is typically on the order of $L = 2\pi R \approx 2\pi \times 10^2\ \mu m$.

Further analyses would be needed to understand why the transfer-matrix quality factor Q_{TM} from eq. (5.58) and the FDTD quality factors in figures 5.10 and 5.11 do not match. In spite of this slight discrepancy, the FDTD results confirm the validity of our approximate approach.

5.5 Conclusions

In this chapter we have sketched a novel design protocol for Bloch surface wave-based nanobeam cavities. The approach mainly relies on two principles. On the one hand, the full three-dimensional structure is approximated to two two-dimensional structures by means of effective index theory, in which the 3D nature of the physical objects is hidden in the effective index of the optical modes they support. On the other hand, the confinement of light itself proceeds from the application of the so-called Noda's argument, in which the cavity was designed so as to obtain an in-cavity field with no spurious Fourier components either inside the light cone or outside the photonic band gap of the supporting multilayer. Our design algorithm led to a structure that was tested with FDTD simulations: despite a not entirely unexpected mismatch in the quality factors, harmonic analysis performed by the FDTD software confirmed the presence of a resonance at the desired wavelength and a quality factor on the order of 10^5.

Chapter 6

Conclusions and perspectives

This thesis represents a selection of the results I gathered during my PhD at the University of Pavia, from autumn 2015 to late summer 2018.

The first topic I focused on during my PhD regarded Bloch surface waves at large. While browsing through the recent scientific literature, my supervisor and I noticed that the majority of the papers we happened upon simply took for granted that Bloch surface waves had some sort of advantage in terms of surface field with respect to simpler, totally TIR-based solutions. Moreover, we noticed a certain confusion regarding the term *surface field enhancement*, which had somehow been juxtaposed to the value of the electric field close to the surface of the photonic structure. This was particularly problematic: the typical theoretical scheme involves a plane wave coupling into the mode by means of a prism, where modes are signalled by the divergence of a properly calculated transmission coefficient for the supporting structure. This implies that by properly tuning the parameters of the coupling mechanism, the electric field at the surface can assume any value, thus making a direct comparison of this figure between different photonic structures essentially immaterial.

Thus, our first goal was to understand whether Bloch surface waves actually had a strategic advantage or if similar performance could in principle be achieved with alternative electromagnetic modes in simpler (or cheaper) structures. To pursue this goal, we focused on two figures of merit - the *modal length* and the *electric field at the external surface* - and compared the performance of the TE0 mode supported by an asymmetrical slab waveguide and the BSW supported by a truncated one-dimensional photonic crystal. We spent a lot of attention on widening the scope of our analysis: on the one hand, we considered dielectric media with refractive indices ranging from typical polymeric materials to hard semiconductors both in the weak and strong refractive-index contrast regimes; on the other hand, we decided to rely on energy-scaled figures of merit in order to make our conclusions valid for any work wavelength - at least as long as the chromatic dispersion of the specific materials can be neglected. As to the modal length, we showed that for refractive index contrasts $\Delta n > 0.5$, the modal length of BSWs is smaller than that of the TE0 mode:

indeed, this means that BSWs have larger electromagnetic energy densities, but this maximum occurs in a generic point inside the structure, *i.e.* unaccessible from the outside world. In addition to this, BSWs were also shown to exhibit larger surface fields with respect to the TE0 mode, thus confirming the correctness of the generalized interest in BSWs typically shown in scientific papers. However, we also calculated that this enhancement only reached up to 45%, which implies that in certain occasions one may resort to regular asymmetric slabs instead of going the extra mile and fabricate a complex photonic crystal.

After this, we investigated the interaction between Bloch surface waves and one-dimensional gratings fabricated on top of the supporting truncated one-dimensional photonic crystal. As expected, the presence of a further periodicity transversal to the main one gives rise to a folding of the dispersion of the modes inside the first Brillouin zone, and this leads to the opening of a photonic band gap. We then evaluated the dependence of both the width of the band gap and the photonic modes on the structural parameters of the grating. This analysis was carried out with two approaches: on the one hand, we relied on rigorous coupled-wave analysis to calculate the exact dispersion of the modes; then, we also approximated the grating with a uniform slab via effective-index theory, and managed to recover the exact dispersions to an extremely high level of accuracy. Among our conclusions, we can mention that, as expected, an increase in the optical thickness of the effective slab - caused for example by an increase in the filling fraction of the grating - redshifts the dispersion of the guided BSWs. In addition to this, we showed that increasing the height of the grating causes both a widening of the photonic band gap and a redshift of the mode dispersion.

From this point, we moved from one-dimensional systems and decided to focus on two-dimensional structures. A few years ago, BSWs had already been shown experimentally to resonate in optical microdisks; this result was extremely promising with a view to full on-chip integration of Bloch surface waves, but also came at the cost of rather large modal volumes. More or less contemporarily, we started looking for Bloch surface wave-based ring resonators. A collaboration with professor S. M. Weiss from Vanderbilt University brought to the realization of a porous silicon ring resonator on top of a truncated periodic multilayer supporting BSWs. We studied the system by a variety of means involving transfer matrices, effective-index theory and FDTD simulations, while the experimental group in Tennessee devoted itself to the fabrication of the device in porous silicon and the realization of the experiment. We showed the experimental transmission spectrum to be compatible with our theoretical expectations, thus confirming the first experimental observation of a Bloch surface wave-based ring resonator. Professor Weiss and her collaborator measured an experimental quality factor $Q \approx 10^3$.

Lastly, we moved to full three-dimensional confinement of light by considering the design of a Bloch surface wave-based nanobeam cavity. As usual, we

relied on a variety of theoretical techniques such as transfer matrices, effective-index theory and FDTD simulations and also on the so-called *Noda's argument* to try and devise an algorithm to design BSW-based nanobeam cavities tuned to a specific wavelength and with reasonably high quality factors. By gradually removing Fourier components out of the light cone, we managed to obtain a structure characterized by two-dimensional quality factors in the order of $Q \sim 10^5$. These results were tested with 2D FDTD simulations, and we are still looking forward to a full 3D confirmation of our recipe.

Altogether, this three-year research project moved from one-dimensional theoretical observations to the design of 2D BSW ring resonators and finally to the development of an algorithm for the design of cavities leading to full 3D confinement of BSWs. I believe that these results provided additional insight into the field of these particular solutions of Maxwell's equation in truncated photonic crystals. However, *though much is taken, much abides*, and I look forward to the new directions and further applications the research on BSWs might take in the near future.

Appendix A

Transfer Matrix Method

The propagation of electromagnetic radiation in a multilayered structure can be studied by means of the so-called transfer matrix method (TMM). This method is particularly convenient in the presence of linear propagation, since in this case the transfer matrix itself can be expressed as a simple product of *interface* and *propagation* matrices.

A.1 General derivation

Let us start the discussion by assuming a multilayer such as the one shown in Fig. A.1.

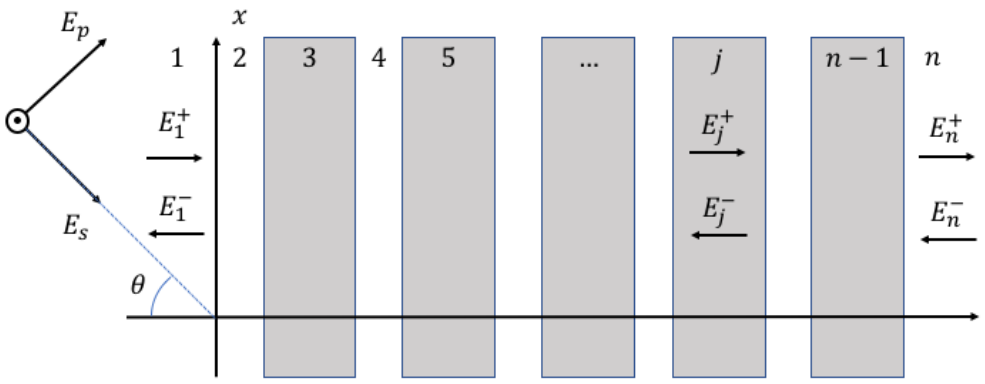

Figure A.1: ML structure

The structure consists of n layers characterized by a width d_j and a refractive index n_j. If the axis are oriented as in Fig. A.1, *i.e.* with light impinging in the π_{xz} plane and the layers perpendicular to the z axis, the electric field in each layer can be decomposed as a sum of propagating and counter-propagating

waves as

$$E_j(r) = [E_j^+ e^{ik_z z} + E_j^- e^{-ik_z z}]e^{i(k_x x - \omega t)}, \tag{A.1}$$

where harmonic time dependence $\propto exp(-i\omega t)$ was also assumed. In this equation, k_x and k_z are the components of the wave vector along the x and z axis and E_j^+, E_j^- are the amplitudes of the forward and backward waves, respectively. The notation in eq. A.1 is valid for both $s-$ and $p-$polarized radiation. The fields across different layers are linked by the usual continuity conditions implied by Maxwell's equations, which, in the absence of surface charge or current densities, can be written as:

$$E_{1\parallel} = E_{2\parallel}, \tag{A.2}$$
$$H_{1\parallel} = H_{2\parallel}, \tag{A.3}$$
$$D_{1\perp} = D_{2\perp}, \tag{A.4}$$
$$B_{1\perp} = B_{2\perp}. \tag{A.5}$$

In particular, the tangential components of both the electric and the magnetic fields are conserved at every interface between the i-th and $(i+1)$-th layer. By introducing a vector $\boldsymbol{E_j}$ containing the amplitudes of both the forward and backward propagating electric fields, that is

$$\boldsymbol{E_j} = \begin{pmatrix} E_j^+ \\ E_j^- \end{pmatrix}, \tag{A.6}$$

the continuity condition on a single interface can be enforced by writing

$$\boldsymbol{E_i = M_{i,j} E_j}, \tag{A.7}$$

where the $M_{i,i+1}$ matrix is defined as

$$\boldsymbol{M_{i,i+1}} = \frac{\mathbf{1}}{\boldsymbol{t_{ij}}} \begin{pmatrix} \mathbf{1} & \boldsymbol{r_{ij}} \\ \boldsymbol{r_{ij}} & \mathbf{1} \end{pmatrix}, \tag{A.8}$$

where r_{ij} and t_{ij} are the polarization-dependent Fresnel coefficients given by

$$r_{ij}^s = \frac{w_i - w_j}{w_i + w_j}, \qquad t_{ij}^s = \frac{2 \cdot w_i}{w_i + w_j} \tag{A.9}$$

for s-polarization and

$$r_{ij}^p = \frac{\varepsilon_j w_i - \varepsilon_i w_j}{\varepsilon_j w_i + \varepsilon_i w_j}, \qquad t_{ij}^p = \frac{2 n_i n_j \cdot w_i}{\varepsilon_j w_i + \varepsilon_i w_j} \tag{A.10}$$

for p-polarization. In these equations, the ws represent the component of the wave vector perpendicular to the interfaces in each layer, *i.e.*

$$w_i = \frac{2\pi n_i}{\lambda_0} \cos\theta. \tag{A.11}$$

Moreover, straightforward manipulations of the definitions given in eq. (A.9) and (A.10) yield a series of useful symmetry relations:

$$r_{ij} = -r_{ji} \tag{A.12}$$
$$t_{ij}t_{ji} = 1 + r_{ij}r_{ji}. \tag{A.13}$$

In order to account for the phase gained by the field as it propagates inside a layer, one can write, provided $d < d_j$,

$$\boldsymbol{E_j(z_j + d) = \Phi_j E_j(z_j),} \tag{A.14}$$

where the *propagation matrix* was introduced, defined as

$$\Phi_j = \begin{pmatrix} \exp iw_j d & 0 \\ 0 & \exp -iw_j d \end{pmatrix}. \tag{A.15}$$

Once propagation and interface matrices are defined as in equations (A.15) and A.8, one can defined the *transfer matrix* for the whole structure by multiplying them in the same order as they appear inside the layered structure:

$$M_{1\to n} = M_{n-1\to n}\Phi_{n-1}M_{n-2\to n-1}\Phi_{n-2} \cdot \Phi_2 M_{1\to 2}\Phi_1. \tag{A.16}$$

The *transfer matrix* $M_{1\to n}$ links the forward- and backward-propagating components on one side of the multi-layered structure to those on the other side. For the sake of clarity, let us assume that an electric field is impinging on the structure only from the first layer, as in fig. A.1. In this case, we can write

$$\begin{pmatrix} E_n^+ \\ 0 \end{pmatrix} = M_{1\to n} \begin{pmatrix} E_1^+ \\ E_1^- \end{pmatrix} \tag{A.17}$$
$$\begin{pmatrix} E_n^+ \\ 0 \end{pmatrix} = \begin{pmatrix} M_{11} & M_{12} \\ M_{21} & M_{22} \end{pmatrix} \begin{pmatrix} E_1^+ \\ E_1^- \end{pmatrix}. \tag{A.18}$$

Carrying out the algebraic product, we end up with the following equations,

$$E_n^+ = M_{11}E_1^+ + M_{12}E_1^- \tag{A.19}$$
$$0 = M_{21}E_1^+ + M_{22}E_1^-. \tag{A.20}$$

The second one can be cast in the following form

$$-M_{21}E_1^+ = M_{22}E_1^- \tag{A.21}$$
$$-\frac{M_{21}}{M_{22}} = \frac{E_1^-}{E_1^+}, \tag{A.22}$$

where on the right-hand side of the equation we find the ratio between the backward-propagation and the forward-propagating field amplitudes, *i.e.* the Fresnel reflection coefficient by definition:

$$R = -\frac{M_{21}}{M_{22}} = \frac{E_1^-}{E_1^+}. \tag{A.23}$$

As to the second equation A.19, it can be rearranged to yield

$$\frac{E_n^+}{E_1^+} = M_{11} + M_{12}\frac{E_1^-}{E_1^+}; \tag{A.24}$$

in it, one can recognize both the Fresnel reflection coefficient defined in eq. (A.23) and the Fresnel transmission coefficient,

$$T = \frac{E_n^+}{E_1^+}. \tag{A.25}$$

Thus, substituting these two figures yields

$$T = M_{11} + M_{12}r = \tag{A.26}$$

$$= M_{11} - \frac{M_{21}M_{12}}{M_{22}} = \tag{A.27}$$

$$= \frac{M_{11}M_{22} - M_{21}M_{12}}{M_{22}} = \tag{A.28}$$

$$= \frac{\det(M_{1\to n})}{M_{22}}, \tag{A.29}$$

an expression for the transmission coefficient in terms of transfer matrix elements.

The transfer matrix $M_{1\to n}$ can be useful for a variety of applications, such as evaluating the overall reflectance or transmittance of a multi-layered structure or to calculate the photonic modes supported by this structure.

As an example, consider a layer of thickness d_c and refractive index n_c sandwiched between two semi-infinite leads chacterized by refractive indices n_1 and n_2, as shown in picture A.2.

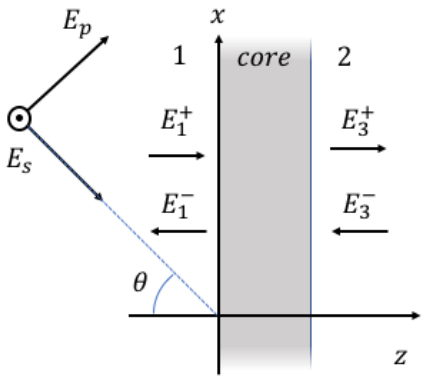

Figure A.2: A simple dielectric slab sandwiched between two semi-infinite media.

In this case, the interface matrices are

$$I_{1,c} = \frac{1}{t_{1,c}} \begin{pmatrix} 1 & r_{1,c} \\ r_{1,c} & 1 \end{pmatrix}, \tag{A.30}$$

for the interface between medium 1 and the core, and

$$I_{c,2} = \frac{1}{t_{c,2}} \begin{pmatrix} 1 & r_{c,2} \\ r_{c,2} & 1 \end{pmatrix}, \tag{A.31}$$

for the interface between the core and medium 2, while the propagation matrix in the core region is

$$\Phi = \begin{pmatrix} e^{iwd_c} & 0 \\ 0 & e^{-iwd_c} \end{pmatrix}, \tag{A.32}$$

where w is the component of the wave vector perpendicular to the interfaces of the slab. The transfer matrix A.16 is then given by

$$M_{1\to3} = \frac{1}{t_{2,c}t_{c,1}} \begin{pmatrix} 1 & r_{2,c} \\ r_{2,c} & 1 \end{pmatrix} \begin{pmatrix} e^{iwd_c} & 0 \\ 0 & e^{-iwd_c} \end{pmatrix} \begin{pmatrix} 1 & r_{c,1} \\ r_{c,1} & 1 \end{pmatrix} = \tag{A.33}$$

$$= \frac{1}{t_{2,c}t_{c,1}} \begin{pmatrix} 1 & r_{2,c} \\ r_{2,c} & 1 \end{pmatrix} \begin{pmatrix} e^{iwd_c} & r_{c,1}e^{iwd_c} \\ r_{c,1}e^{-iwd_c} & e^{-iwd_c} \end{pmatrix} = \tag{A.34}$$

$$= \frac{1}{t_{2,c}t_{c,1}} \begin{pmatrix} e^{iwd_c} + r_{2,c}r_{c,1}e^{-iwd_c} & r_{c,1}e^{iwd_c} + r_{2,c}e^{-iwd_c} \\ r_{c,1}e^{-iwd_c} + r_{2,c}e^{iwd_c} & e^{-iwd_c} + r_{2,c}r_{c,1}e^{iwd_c} \end{pmatrix}. \tag{A.35}$$

The transmittance given by eq. (A.26) becomes

$$T = \frac{\det(M)}{M_{22}} = \tag{A.36}$$

$$= \frac{1}{t_{2,c}t_{c,1}} \left[\frac{\left(e^{iwd_c} + r_{2,c}r_{c,1}e^{-iwd_c}\right)\left(e^{iwd_c} + r_{2,c}r_{c,1}e^{-iwd_c}\right)}{M_{22}} + \right. \tag{A.37}$$

$$\left. - \frac{\left(r_{c,1}e^{iwd_c} + r_{2,c}e^{-iwd_c}\right)\left(r_{c,1}e^{-iwd_c} + r_{2,c}e^{iwd_c}\right)}{M_{22}} \right] = \tag{A.38}$$

$$= \frac{1}{t_{2,c}t_{c,1}} \frac{1 - r_{c,1}^2 - r_{2,c}^2 + (r_{2,c}r_{c,1})^2}{e^{-iwd_c}(r_{2,c}r_{c,1}e^{2iwd_c} + 1)} = \tag{A.39}$$

$$= \frac{1}{t_{2,c}t_{c,1}} \frac{1 - r_{c,1}^2 - r_{2,c}^2(1 - r_{c,1}^2)}{e^{-iwd_c}(r_{2,c}r_{c,1}e^{2iwd_c} + 1)} = \tag{A.40}$$

$$= \frac{1}{t_{2,c}t_{c,1}} \frac{(1 - r_{c,1}^2)(1 - r_{2,c}^2)}{e^{-iwd_c}(r_{2,c}r_{c,1}e^{2iwd_c} + 1)} = \tag{A.41}$$

$$= \frac{1}{t_{2,c}t_{c,1}} \frac{t_{c,1}t_{1,c}t_{2,c}t_{c,2}e^{iwd_c}}{(r_{2,c}r_{c,1}e^{2iwd_c} + 1)} = \tag{A.42}$$

$$= \frac{t_{1,c}t_{c,2}e^{iwd_c}}{1 - r_{2,c}r_{1,c}e^{2iwd_c}}, \tag{A.43}$$

where use has been made of the symmetry relations described above in equations (A.12) and (A.13). The procedure to evaluate the reflectance starts from eq. (A.23) and follows the same steps; the result is

$$R = r_{1,c} + \frac{t_{1,c} r_{c,2} t_{c,1} e^{2iwd_c}}{1 - r_{2,c} r_{1,c} e^{2iwd_c}}. \tag{A.44}$$

The validity of these equations, sometimes reported as Airy's equations[89], can be tested by resorting to an elementary derivation. If the amplitude of

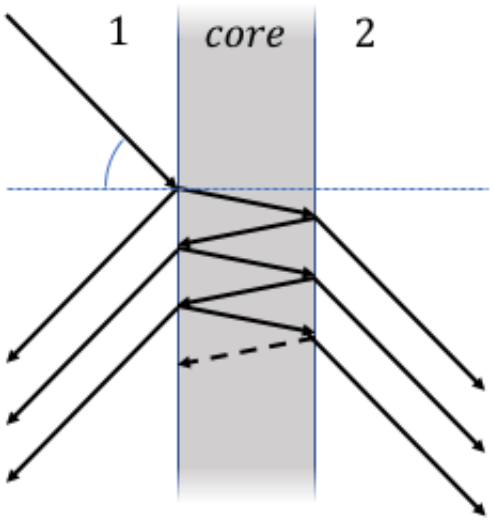

Figure A.3: Multiple reflections and transmissions from a simple dielectric slab.

the electric field impinging from medium 1 is E_i, the overall amplitude of the reflected light will be given by a series of contributions:

$$E_r = E_i \left(r_{1,c} + t_{1,c} r_{c,2} t_{c,1} e^{i\delta} + t_{1,c} r_{c,2} r_{c,1} r_{c,2} t_{c,1} e^{i\delta} + \cdots \right), \tag{A.45}$$

where $\delta = 2wd_{core}$ is the phase acquired by a full trip inside the core region. In equation (A.45), one can recognize light reflected straight-away off the first interface ($r_{1,c}E_i$), light transmitted through the first interface, reflected from the second and transmitted again through the first interface, although in the other direction ($t_{1,c} r_{c,2} t_{c,1} e^{2i\delta} E_i$), etc. Each time light adds a round trip inside the core region, it gains a phase factor $e^{i\delta}$ and an additional reflection factor $r_{c,2} r_{c,1}$. This means that the contributions sum to a geometric series whose ratio is $r_{c,2} r_{c,1} e^{i\delta}$, *i.e.*

$$E_r = E_i \left(r_{1,c} + t_{1,c} r_{c,2} t_{c,1} e^{i\delta} \sum_{n=0}^{\infty} (r_{c,2} r_{c,1} e^{i\delta})^n \right) = \tag{A.46}$$

$$= E_i \left(r_{1,c} + \frac{t_{1,c} r_{c,2} t_{c,1} e^{i\delta}}{1 - r_{c,2} r_{c,1} e^{i\delta}} \right), \tag{A.47}$$

which is the same as eq. (A.44).

The transfer-matrix method can also be used to investigate the photonic modes supported by a particular multi-layered photonic structure.

Reflectance and transmittance can be seen as simple optical response functions for the structure under scrutiny. In particular, once they have been calculated - via the transfer-matrix method or otherwise - one can investigate which modes are supported by a particular structure by studying the poles of either R or T, *i.e.*

$$1 - r_{2,c} r_{1,c} e^{2iwd_c} = 0. \tag{A.48}$$

As an example, the TE-polarized modes supported by a silicon ($n_{Si} = 3.48$) slab of thickness $d = 320$nm are shown in Fig.

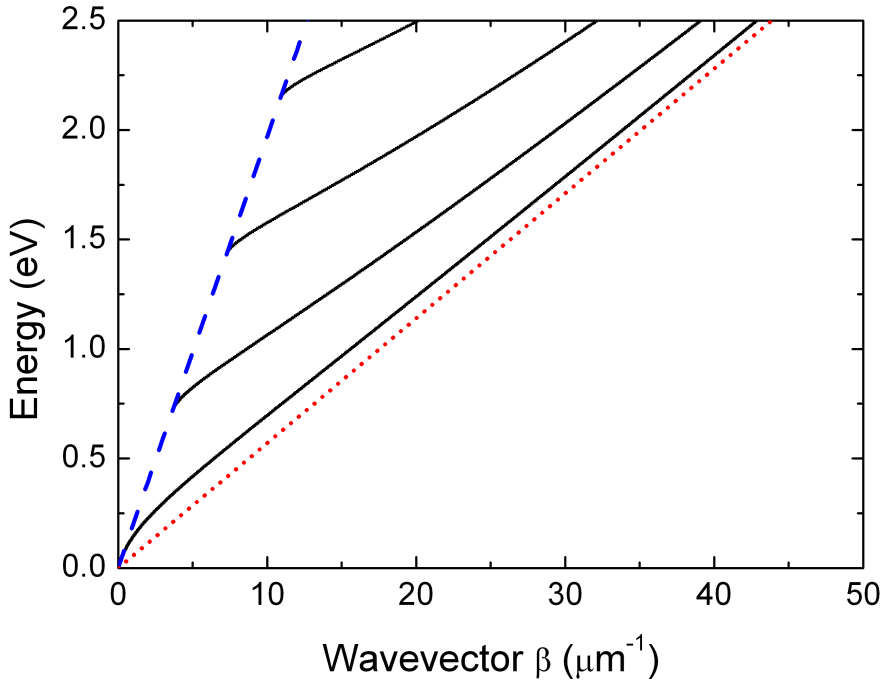

Figure A.4: TE modes supported by a 320 nm silicon slab ($n = 3.48$). The dashed blue line and the red dotted line represent the air and silicon light lines, respectively.

A.2 Transfer matrix for a bilayer

Consider a system formed by the infinite repetition of a unit cell consisting of two layers: the first one has thickness d_1 and refractive index n_1, the second one has thickness d_2 and refractive index n_2. The transfer matrix for such a system can be built according to eq. (A.16) as

$$M = I_{12} \Phi_2 I_{21} \Phi_1, \tag{A.49}$$

where the component matrices are

$$I_{12} = \frac{1}{t_{12}} \begin{pmatrix} 1 & r_{12} \\ r_{12} & 1 \end{pmatrix}, \quad I_{21} = \frac{1}{t_{21}} \begin{pmatrix} 1 & r_{21} \\ r_{21} & 1 \end{pmatrix}, \quad \Phi_j = \begin{pmatrix} e^{iwd_j} & 0 \\ 0 & e^{-iwd_j} \end{pmatrix}. \tag{A.50}$$

After some tedious algebra, the transfer matrix becomes

$$M = \begin{pmatrix} e^{i(\phi_1+\phi_2)} + r_{12}r_{21}e^{i(\phi_1-\phi_2)} & r_{21}e^{i(\phi_2-\phi_1)} + r_{12}e^{-i(\phi_1+\phi_2)} \\ r_{12}e^{i(\phi_1+\phi_2)} + r_{21}e^{i(\phi_1-\phi_2)} & r_{12}r_{21}e^{i(\phi_2-\phi_1)} + e^{-i(\phi_1+\phi_2)} \end{pmatrix}, \tag{A.51}$$

and the trace becomes

$$Tr(T) = \frac{1}{t_{12}t_{21}} \left[\left(e^{i(\phi_1+\phi_2)} + e^{-i(\phi_1+\phi_2)} \right) + r_{12}r_{21} \left(e^{i(\phi_1-\phi_2)} + e^{-i(\phi_1-\phi_2)} \right) \right] \tag{A.52}$$

If we further assume that the phases are real, *i.e.* $\phi_1 = w_1 d_1$ and $\phi_2 = w_2 d_2$, the trace of the bilayer transfer matrix reduces to

$$Tr(T_{period}) = 2\cos(\phi_1)\cos(\phi_2) - 2\sin(\phi_1)\sin(\phi_2) \left(\frac{2}{t_{12}t_{21}} - 1 \right). \tag{A.53}$$

If one desires to write the trace in terms of wave vector components, then one just needs to recall the definition of the Fresnel coefficient given above, *i.e.*

$$r_{12} = \begin{cases} \frac{w_1 - w_2}{w_1 + w_2} & \text{TE-polarized wave} \\ \frac{\xi_1 - \xi_2}{\xi_1 + \xi_2} & \text{TM-polarized wave} \end{cases} \tag{A.54}$$

for the reflection coefficient, where $\xi_i = \frac{w_i}{\epsilon_i}$, and

$$t_{12} = \begin{cases} 1 + r_{12} & \text{TE-polarized wave} \\ \frac{n_1}{n_2}(1 + r_{12}) & \text{TM-polarized wave} \end{cases} \tag{A.55}$$

for the transmission coefficients.

Substituting these yields

$$\begin{aligned} Tr(T) = {} & e^{iw_1d_1}\cos(w_2d_2) + \frac{i}{2}e^{iw_1d_1}\left(\frac{w_1}{w_2} + \frac{w_2}{w_1}\right)\sin(w_2d_2) + \\ & + e^{-iw_1d_1}\cos(w_2d_2) - \frac{i}{2}e^{-iw_1d_1}\left(\frac{w_1}{w_2} + \frac{w_2}{w_1}\right)\sin(w_2d_2) = \\ & = 2\cos(w_1d_1)\cos(w_2d_2) - \sin(w_1d_1)\sin(w_2d_2)\left(\frac{w_1}{w_2} + \frac{w_2}{w_1}\right). \end{aligned} \tag{A.56}$$

Although less wieldy than its equivalent form in eq. (A.53), this equation can be shown to be easily convertible between TE and TM polarization. Indeed, the term in the parentheses can be cast in the convenient form

$$C = \frac{\alpha_1}{\alpha_2} + \frac{\alpha_2}{\alpha_1}, \tag{A.57}$$

where α_1 and α_2 have polarization-dependent form:

$$\alpha_i = \begin{cases} n_i\cos(\theta_i) & \text{TE-polarized wave} \\ \cos(\theta_i)/n_i & \text{TM-polarized wave} \end{cases} \tag{A.58}$$

A.3 Gap condition

When the physical system under scrutiny features translational invariance, the eigenvalues of the transfer matrix M in eq. (A.51) must be $\lambda_{1,2} = e^{\pm iq\Lambda}$, where $\Lambda = d_1 + d_2$ is the period of the bilayer. Then one can deduce that the trace of the transfer matrix must be

$$Tr(M) = e^{ik_{Bloch}\Lambda} + e^{-ik_{Bloch}\Lambda} = 2\cos(k_{Bloch}\Lambda). \tag{A.59}$$

Equating formulas (A.59) and (A.52), one gets

$$2\cos(k_{Bloch}\Lambda) = \frac{1}{t_{12}t_{21}}\left[\left(e^{i(\phi_1+\phi_2)}+e^{-i(\phi_1+\phi_2)}\right)+r_{12}r_{21}\left(e^{i(\phi_1-\phi_2)}+e^{-i(\phi_1-\phi_2)}\right)\right]. \tag{A.60}$$

It is then straightforward to notice that the absolute value of the LHS in eq. (A.60) is bounded by 2, whereas the RHS is not. As a consequence, one is not guaranteed to find values of $k_{Bloch} \in \mathbb{R}$ that satisfy the equation. When this happens, then $k_{Bloch} = iq \in \mathbb{C}$. The set of values of the parallel component of the propagation wave vector for which this happens is called *photonic band gap*.

The imaginary part of the Bloch wave vector, $q = \Im[k_{Bloch}]$ can be easily found from eq. (A.60). Introducing $z = e^{ik_{Bloch}}$, then $z^{-1} = e^{-ik_{Bloch}}$, and the trace becomes

$$z + \frac{1}{z} = Tr(M), \tag{A.61}$$

and this leads to

$$z^2 - Tr(M)z + 1 = 0. \tag{A.62}$$

Thus, as $k_\parallel$ varies, one can immediately understand if the gap condition is verified by checking whether the second-degree equation has real or imaginary solutions. If the discriminant

$$\Delta = [Tr(M)]^2 - 4 \tag{A.63}$$

is negative, then $z \in \mathbb{C}$. Since $z = e^{ik_{Bloch}}$, this means that the Bloch wave vector is real, *i.e.* that $k_\parallel$ does not lie in the photonic band gap. On the other hand, if $\Delta > 0$, then the solutions to eq. (A.62) are real, *i.e.* $k_{Bloch} \in \mathbb{C}$. Following up,

$$z_{1,2} = \frac{Tr(M) \pm \sqrt{\Delta}}{4}; \tag{A.64}$$

the proper solution can be selected by recalling that $\Im[kBloch] > 0$ is needed to enforce exponential decay of the field in the stacking direction. This implies that if $Tr(M) > 0$, then $z = z_1 = \frac{Tr(M)+\sqrt{\Delta}}{4}$, otherwise $z = -z_2 = \frac{-Tr(M)+\sqrt{\Delta}}{4}$. Finally, the imaginary part of the Bloch wavevector will be

$$q = \Im[k_{Bloch}] = \frac{1}{\Lambda}\ln z. \tag{A.65}$$

The behavior of q is shown in fig (A.5) and (A.6) for both varying and fixed energy.

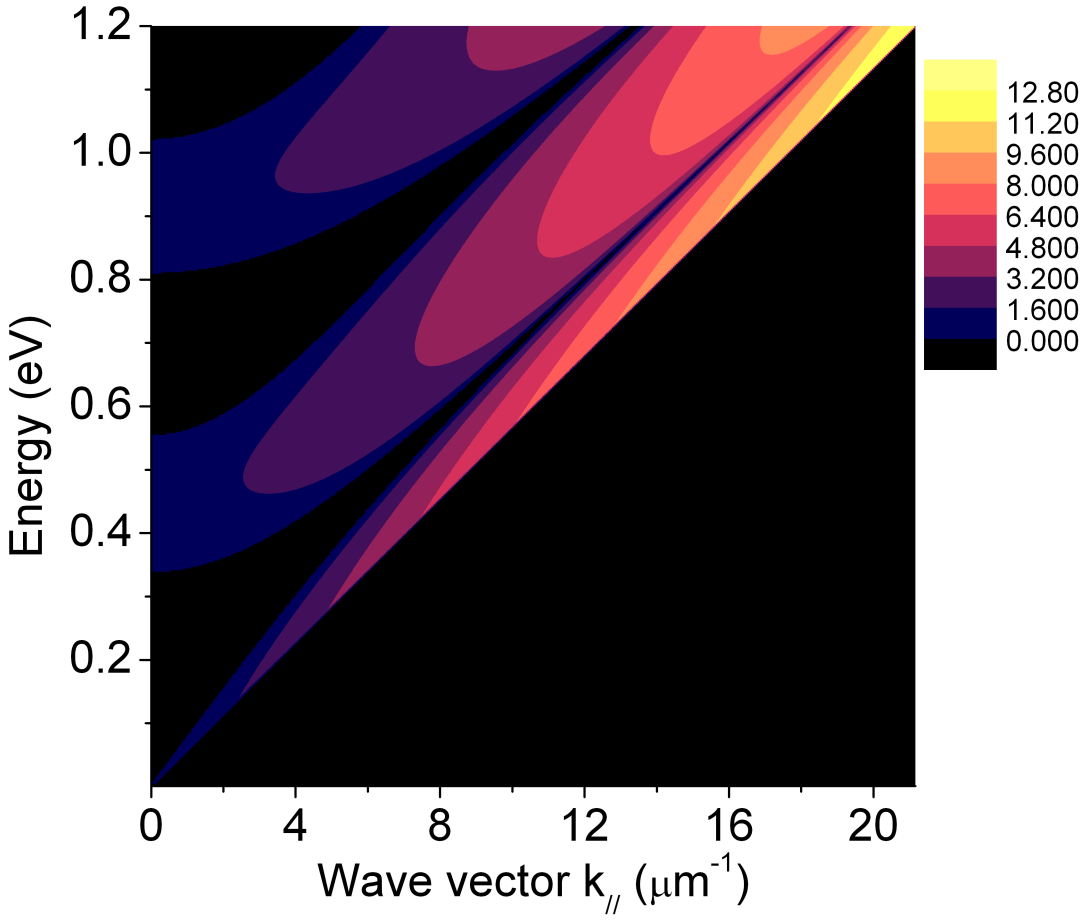

Figure A.5: TE-polarized photonic band gap for a semi-infinite Si/SiO_2 multilayer of thicknesses $d_1 = 260$ nm, $d_2 = 320$ nm and refractive indices $n_1 = 3.48$, $n_2 = 1.44$.

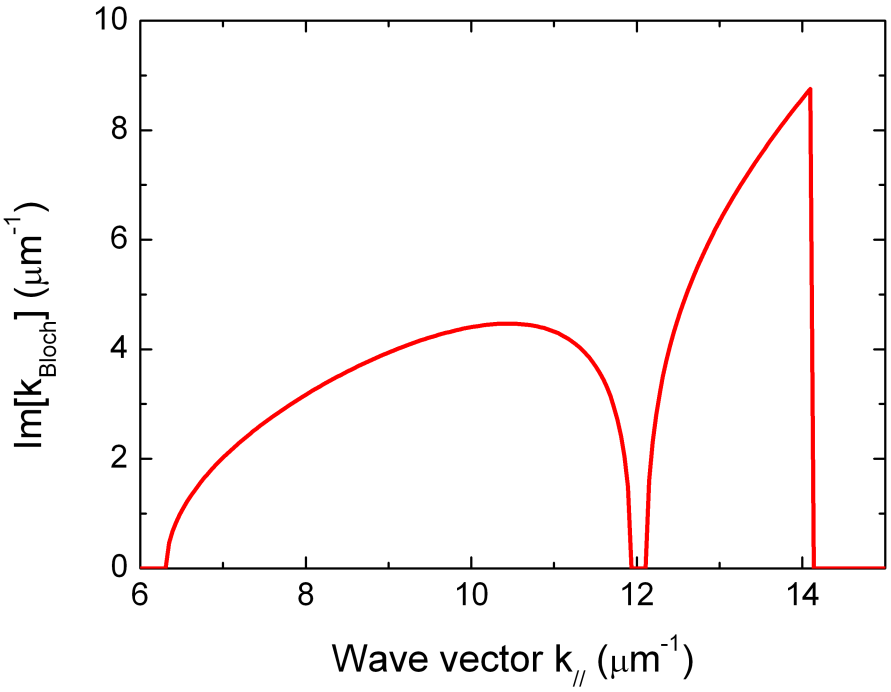

Figure A.6: Imaginary part of the Bloch wave vector for a semi-infinite Si/SiO_2 multilayer of thicknesses $d_1 = 260$ nm, $d_2 = 320$ nm and refractive indices $n_1 = 3.48$, $n_2 = 1.44$ at a fixed energy $E = 0.8$ eV and for TE-polarization.

The trace given in eq. (A.60) can be further simplified when all the phase factors $\phi_j = w_j d_j$ are real. In this case, the trace becomes

$$\cos(q\Lambda) = \cos(w_1 d_1)\cos(w_2 d_2) - \frac{1}{2}\left(\frac{\alpha_1}{\alpha_2} + \frac{\alpha_2}{\alpha_1}\right)\sin(w_1 d_1)\sin(w_2 d_2), \quad \text{(A.66)}$$

where the αs depend on the polarization and are defined as

$$\text{TE polarization} \begin{cases} \alpha_j = w_j \\ \alpha_i = w_i \end{cases} \quad \text{(A.67)}$$

and

$$\text{TM polarization} \begin{cases} \alpha_j = \varepsilon_i w_j \\ \alpha_i = \varepsilon_j w_i \end{cases} \quad \text{(A.68)}$$

In the case of a quarter-wavelength stack, one has $w_j d_j = \pi/2$, and eq. (A.66) can be simplified to obtain the following value for the complex Bloch wave vector:

$$q = \frac{\pi}{\Lambda} + i\frac{\Delta n}{n\Lambda}. \quad \text{(A.69)}$$

A.4 Photonic band gap for TM polarization

In the simplest picture, reflection and transmission of an electric field impinging on a surface can be explained by Fresnel coefficients, given by equations (A.9) and (A.9), and reported here for convenience:

$$r_s = \frac{n_1 \cos\theta_1 - n_2 \cos\theta_2}{n_1 \cos\theta_1 + n_2 \cos\theta_2} \qquad t_s = \frac{2n_1 \cos\theta_1}{n_1 \cos\theta_1 + n_2 \cos\theta_2}. \tag{A.70}$$

$$r_p = \frac{n_1 \cos\theta_2 - n_2 \cos\theta_1}{n_1 \cos\theta_2 + n_2 \cos\theta_1} \qquad t_p = \frac{2n_1 \cos\theta_1}{n_1 \cos\theta_2 + n_2 \cos\theta_1}. \tag{A.71}$$

In the current notation, a ray of light impinges on an interface between a medium n_1 and a medium n_2 with an angle θ_1, and emerges beyond the interface with an angle θ_2. When the two angles are complementary, *i.e* $\theta_1 + \theta_2 = \pi/2$, clearly $\sin(\theta_2) = \sin(\pi/2 - \theta_1) = \cos(\theta_1)$; this implies that

$$n_1 \sin\theta_1 = n_2 \sin\theta_2 = n_2 \cos\theta_1, \tag{A.72}$$

from Snell's law of refraction. The angle of incidence θ_1 which satisfies this equation is the well-known *Brewster angle* θ_B, given by

$$\theta_B = \arctan\frac{n_2}{n_1}. \tag{A.73}$$

If this angle is substituted into eq. (A.71), we can see that $r_p = 0$, thus frustrating interference in the periodic multilayer. In this particular condition, the multilayer becomes transparent and the gap closes, as shown in picture A.7.

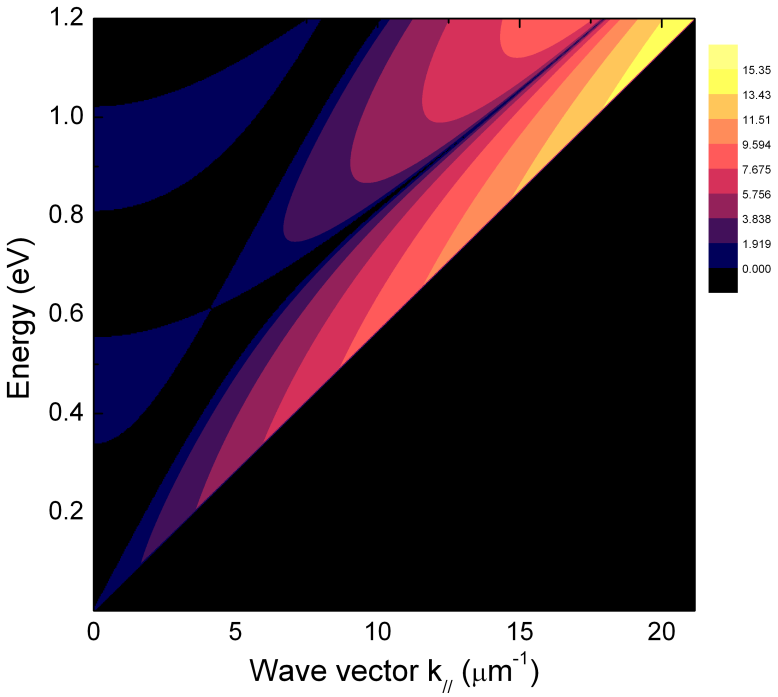

Figure A.7: TM-polarized photonic band gap for a semi-infinite Si/SiO_2 multilayer of thicknesses $d_1 = 260$ nm, $d_2 = 320$ nm and refractive indices $n_1 = 3.48$, $n_2 = 1.44$. The color scale corresponds to the value of the imaginary part of the Bloch wave vector $q = \Im[k_{Bloch}]$.

This closure of the photonic band gap in the case of p polarization makes TM BSWs less appealing with respect to non-dielectric solutions such as surface plasmon polaritons.

A.5 Modal length of a BSW

In a 1D scheme, the general definition of *modal length* is given by

$$L_{mod} = \frac{1}{\varepsilon_{max}|E_{max}|^2} \int_{-\infty}^{\infty} |E(z)|^2 \varepsilon(z) dz \tag{A.74}$$

The *modularity* of a semi-infinite one-dimensional photonic crystal can be exploited to split the general definition (A.74) in its various contributions:

$$L_{mod} = \frac{1}{\varepsilon_{max}|E_{max}|^2} \left[\int_{\text{ext}} |E(z)|^2 \varepsilon_{ext} dz + \int_{1^{st} \text{ period}} |E(z)|^2 \varepsilon(z) dz + \int_{2^{nd} \text{ period}} |E(z)|^2 \varepsilon(z) dz + \int_{3^{rd} \text{ period}} |E(z)|^2 \varepsilon(z) dz + \ldots \right] \tag{A.75}$$

Moreover, Bloch surface waves live inside the photonic band gap, and Bloch-Floquet theorem then implies exponential decay in the z direction:

$$E(z+\Lambda) = e^{-q\Lambda}E(z). \tag{A.76}$$

This means that the integral on each period beyond the first can be expressed as the one on the first times a factor accounting for the exponential decay:

$$\begin{aligned} L^{mod}_{1^{st}\text{ period}} &= \frac{1}{\varepsilon_{max}|E_{max}|^2}\int_{1^{st}period}|E(z)|^2\varepsilon(z)dz = I \qquad \text{(A.77)}\\ L^{mod}_{2^{nd}\text{ period}} &= \frac{1}{\varepsilon_{max}|E_{max}|^2}\int_{2^{nd}period}|E(z)|^2\varepsilon(z)dz = \\ &= \frac{1}{\varepsilon_{max}|E_{max}|^2}\int_{1^{st}period}|E(z+\Lambda)|^2\varepsilon(z)dz = \\ &= \frac{e^{-2q\Lambda}}{\varepsilon_{max}|E_{max}|^2}\int_{1^{st}period}|E(z)|^2\varepsilon(z)dz = e^{-2q\Lambda}I \\ L^{mod}_{3^{rd}\text{ period}} &= \frac{1}{\varepsilon_{max}|E_{max}|^2}\int_{3^{rd}period}|E(z)|^2\varepsilon(z)dz = e^{-4q\Lambda}I \qquad \text{(A.78)}\\ &\dots \qquad \text{(A.79)} \end{aligned}$$

These terms can be summed as a geometric series of ratio $r = e^{-2q\Lambda}$, and the overall modal length in the case of N repeated unit cells becomes

$$L_{mod,N} = I\left(1 + e^{-2q\Lambda} + e^{-4q\Lambda} + e^{-6q\Lambda} + ...\right) = \frac{1-e^{-2q(N+1)\Lambda}}{1-e^{-2k\Lambda}}I. \tag{A.80}$$

When $N \to \infty$, we resort to the case of a semi-infinite truncated 1D PhC, *i.e.*

$$L_{mod,\infty} = \frac{1}{1-e^{-2q\Lambda}}I. \tag{A.81}$$

Equation (A.81) tells us that we can construct the overall modal length just by calculating the contribution on the first period. This can be written as

$$\begin{aligned} I &= \frac{1}{\varepsilon_{max}|E_{max}|^2}\int_{1^{st}\text{ period}}|E(z)|^2\varepsilon(z)dz = \qquad \text{(A.82)}\\ &= \frac{1}{\varepsilon_{max}|E_{max}|^2}\left[\int_0^{\sigma d_1}|E(z)|^2n_1^2dz + \int_0^{d_2}|E(z)|^2n_2^2dz\int_0^{(1-\sigma)d_1}|E(z)|^2n_1^2dz\right], \end{aligned}$$

where the truncation factor $\sigma \in [0;1]$, whose precise derivation will be given in section A.8, represents the fraction of layer d_1 enabling the existence of a Bloch surface wave inside the photonic band gap, as explained in eq. (A.132).

In the remainder of this section, the electric fields in each layer will be split in a forward-propagating wave and a backward-propagating wave.

The external field, *i.e.*

$$E_{ext}(z) = E_e^+e^{ik_ez} + E_e^-e^{-ik_ez}, \tag{A.83}$$

can be simplified by recalling that BSWs are guided modes, and thus live below the light line of the external medium, *i.e.* $k_e = iw_e$, and that a divergence of the field at infinity in the $(-\infty, 0)$ region of the z axis would be unphysical. Altogether, the external field becomes

$$E_{ext}(z) = E_e^- e^{w_e z}, \tag{A.84}$$

For the rest of the layers, one can proceed likewise.

$$\begin{aligned} E_1(z) &= E_1^+ e^{iw_1 z} + E_1^- e^{-iw_1 z} \\ E_2(z) &= E_2^+ e^{iw_2 z} + E_2^- e^{-iw_2 z} \\ E_3(z) &= E_3^+ e^{iw_1 z} + E_3^- e^{-iw_1 z}, \end{aligned} \tag{A.85}$$

where the wave vector components along z, *i.e.* w_1 and w_2, are defined as

$$w_i = \sqrt{\left(\frac{2\pi}{\lambda_0} n_i\right)^2 - k_\parallel^2}. \tag{A.86}$$

As explained in eq. (A.7), the field amplitudes E_j^+ and E_j^- can all be found by resorting to transfer matrix theory by fixing the value of the field on the first interface between the external dielectric medium and the periodic multilayer, *i.e.* the amplitude E_e^- in eq. (A.84). For example, one can write

$$\begin{pmatrix} 0 \\ E_e^- \end{pmatrix} = I_{1,ext} \begin{pmatrix} E_1^+ \\ E_1^- \end{pmatrix}, \tag{A.87}$$

and substituting the expression for $I_{1,ext}$ given in eq. (A.8) yields

$$\frac{1}{t_{1e}} \begin{pmatrix} 1 & r_{1e} \\ r_{1e} & 1 \end{pmatrix} \begin{pmatrix} E_1^+ \\ E_1^- \end{pmatrix} = \begin{pmatrix} 0 \\ E_e^- \end{pmatrix}, \tag{A.88}$$

from which one derives

$$E_1^+ = \frac{r_{1e}}{t_{1e}} E_e^- \tag{A.89}$$

$$E_1^- = \frac{1}{t_{1e}} E_e^- \tag{A.90}$$

The fields in the second layer d_2 and in the remainder of the first layer, $(1-\sigma)d_1$, can be found with the same method. The calculation is trivial but lengthy, and to avoid unnecessary complications, it is thus omitted. The results are

$$E_2^+ = \frac{1}{t_{21}} \left(E_1^+ e^{i\phi_1} + r_{21} E_1^- e^{-i\phi_1} \right) \tag{A.91}$$

$$E_2^- = \frac{1}{t_{21}} \left(r_{21} E_1^+ e^{i\phi_1} + E_1^- e^{-i\phi_1} \right) E_3^+ \quad = \frac{1}{t_{12}} \left(E_2^+ e^{i\phi_2} + r_{12} E_2^- e^{-i\phi_1} \right) \tag{A.92}$$

$$E_3^- = \frac{1}{t_{12}} \left(r_{12} E_2^+ e^{i\phi_2} + E_2^- e^{-i\phi_1} \right) \tag{A.93}$$

Once that the electric field amplitudes in the unit cell have been found, the electric field amplitudes in the rest of the multilayer can be found by taking into account Bloch-Floquet theory and the fact that BSWs live inside the PBG, as summarized in equation (A.76).

In the j-th layer, the field can be written in terms of forward- and backward-propagating waves as $E_j(z) = E_j^+ e^{iw_j z} + E_j^- e^{-iw_j z}$, therefore its modulus square is

$$\begin{aligned} |E_j(z)|^2 &= (E_j^+ e^{iw_j z} + E_j^- e^{-iw_j z})(E_j^{+,*} e^{-iw_j z} + E_j^{-,*} e^{iw_j z}) = \\ &= |E_j^+|^2 + |E_j^-|^2 + 2\Re\{E_j^+ E_j^{-,*} e^{i2w_j z}\} \end{aligned} \tag{A.94}$$

Plugging this expression in the general definition of modal length given in eq. (A.74) yields

$$L_{mod}^{u.c.} = K\left(\int_0^{\sigma d_1} \varepsilon_1 |E_1(z)|^2 dz + \int_0^{d_2} \varepsilon_2 |E_2(z)|^2 dz + \int_0^{(1-\sigma)d_1} \varepsilon_1 |E_3(z)|^2 dz\right) \tag{A.95}$$

where the constant $K = 1/(\varepsilon|E|^2)_{max}$ was introduced to improve readability.

The integration on the unit cell then yields

$$\begin{aligned} L_{mod}^{u.c.} = K\Bigg[&\epsilon_1(|E_1^+|^2 + |E_1^-|^2)\sigma d_1 + \Im\left\{\frac{E_1^+ E_1^{-,*}}{w_1}\left(e^{i2w_1\sigma d_1} - 1\right)\right\} + \\ &\epsilon_2(|E_2^+|^2 + |E_2^-|^2) d_2 + \Im\left\{\frac{E_2^+ E_2^{-,*}}{w_2}\left(e^{i2w_2 d_2} - 1\right)\right\} + \\ &\epsilon_1(|E_3^+|^2 + |E_3^-|^2)(1-\sigma) d_1 + \Im\left\{\frac{E_3^+ E_1^{-,*}}{w_1}\left(e^{i2w_1(1-\sigma)d_1} - 1\right)\right\}\Bigg]. \end{aligned} \tag{A.96}$$

The rest of the structure can be fully taken into account, according to eq., by means of eq. (A.76) as

$$L_{mod} = K\left[V_{mod}^{ext} + \frac{1}{1 - e^{-2q\Lambda}} L_{mod}^{u.c.}\right] \tag{A.97}$$

A closed expression for the $K = 1/(\varepsilon|E|^2)_{max}$ factor can derived thusly. Given the usual expression for the field in the j-th layer, *i.e.*

$$E_j(z) = E_j^+ e^{ik_j z} + E_j^- e^{-ik_j z}, \tag{A.98}$$

its square modulus has been shown to be

$$|E_j(z)|^2 = |E_j^+|^2 + |E_j^-|^2 + 2\Re\left\{E_j^+ E_j^{-,*} e^{2ik_j z}\right\}. \tag{A.99}$$

This expression can be derived and set equal to zero to find the $z_{max} = \bar{z}$ where the maximum of the square modulus of the field occurs, *i.e.*

$$\frac{\partial |E_j(z)|^2}{\partial z} = 2ikE_j^+ E_j^{-,*} e^{2ik_j z} - 2ik_j E_j^{+,*} B_j e^{-2ik_j z} = 0. \tag{A.100}$$

This implies

$$E_j^+ E_j^{-,*} e^{2ik_j z} = E_j^{+,*} E_j^- e^{-2ik_j z}, \tag{A.101}$$

where it can be easily recognized that the two sides of the equation are the complex conjugate of each other. In turn, this yields

$$\Im\{E_j^+ E_j^{-,*} e^{2ik_j z}\} = 0, \tag{A.102}$$

or, spelled out for the real and imaginary components,

$$\Im\{E_j^+ E_j^{-,*}(\cos(2k_j z) + i\sin(2k_j z))\} = 0. \tag{A.103}$$

This equation can be cast in the form

$$\cos(2k_j z)\Im\{E_j^+ E_j^{-,*}\} + \sin(2k_j z)\Re\{E_j^+ E_j^{-,*}\} = 0, \tag{A.104}$$

which, under the hypothesis that $\cos(2kz) \neq 0$, reduces to

$$\frac{\Im\{E_j^+ E_j^{-,*}\}}{\Re\{E_j^+ E_j^{-,*}\}} = \tan(\phi_{E_j^+ E_j^{-,*}}) = -\tan(2k_j z), \tag{A.105}$$

where $\phi_{E_j^+ E_j^{-,*}} = \phi$ is a shortcut for the argument of the complex number $E_j^+ E_j^{-,*} = |E_j^+ E_j^{-,*}| e^{i\phi}$. Finally, inverting this expression yields

$$\bar{z} = \frac{\pi m - \phi(E_j^+ E_j^{-,*})}{2k_j}, \tag{A.106}$$

where $m \in \mathbb{Z}$ is an integer.

The calculation of the second derivative was carried out, but it is not included here. The main result is that for $\bar{z}$ to correspond to a maximum of the square modulus of the field, m must be an *even* integer.

Now that $\bar{z}$ is known, the maximum can be evaluated by plugging eq. (A.106) in the general definition given in eq. ().

$$\begin{aligned}
|E_j(\bar{z})|^2 &= |E_j^+|^2 + |E_j^-|^2 + E_j^+ E_j^{-,*} e^{2ik_j\bar{z}} + E_j^{+,*} E_j^- e^{-2ik_j\bar{z}} = \\
&= |E_j^+|^2 + |E_j^-|^2 + |E_j^+ E_j^{-,*}| e^{i\phi} e^{2ik_j\bar{z}} + |E_j^{+,*} E_j^-| e^{-i\phi} e^{-2ik_j\bar{z}} = \\
&= |E_j^+|^2 + |E_j^-|^2 + |E_j^+ E_j^{-,*}| e^{i\phi} e^{i(\pi m - \phi)} + |E_j^{+,*} E_j^-| e^{-i\phi} e^{-i(\pi m - \phi)} = \\
&= |E_j^+|^2 + |E_j^-|^2 + |E_j^+ E_j^{-,*}| (e^{i\pi m} + e^{-i\pi m}) = \\
&= |E_j^+|^2 + |E_j^-|^2 + 2|E_j^+ E_j^{-,*}| \cos(\pi m) = \\
&= |E_j^+|^2 + |E_j^-|^2 + 2|E_j^+ E_j^{-,*}|.
\end{aligned} \tag{A.107}$$

where the evenness of m was employed, together with the fact that $E_j^{+,*} E_j^- = (E_j^+ E_j^{-,*})^*$.

All one is left to do is to sequentially evaluate expression (A.107) in each layer forming the unit cell, to understand where the maximum falls: this defines the pre-factor K included in eq. (A.96).

The external field contributes to the modal length with a term

$$L_{mod}^{ext} = \int_{-\infty}^{0} \epsilon_{ext}|E(z)|^2 dz = n_{ext}^2 (E_e^-)^2 \int_{-\infty}^{0} e^{2w_e z} dz = \frac{n_{ext}^2 (E_e^-)^2}{2w_e}, \quad \text{(A.108)}$$

where the K factor was omitted and $k_e = \sqrt{(k_0 n_{ext})^2 - k_\parallel^2} = iw_e$.

This concludes the calculation of the modal length in a truncated periodic multilayer.

A.6 Mode normalization

In eq. (A.89) and (A.91), the amplitudes of the forward- and backward-propagating waves which form the electric field in each layer were derived in terms of the only component left in the external dielectric medium E_{ext}^-. This parameter can be fixed by properly normalizing each mode so that it transports the energy of a photon, according to the general expression[1]

$$\int_{-\infty}^{+\infty} \epsilon(z)|E(z)|^2 dz = \frac{\hbar\omega}{2} \quad \text{(A.109)}$$

Expressions for the square modulus of the field in each layer were worked out in the previous section. Substituting everything yields

$$\begin{aligned}
\frac{\hbar\omega}{2K} = V_{mod}^{ext} + \frac{1}{1-e^{-2k\Lambda}} \Bigg\{ & \epsilon_1 \int_0^{\sigma d_1} \Big(|A_1|^2 + |B_1|^2 + 2\Re\{A_1 B_1^* e^{i2w_1 z}\} \Big) dz + \\
& \epsilon_2 \int_0^{d_2} \Big(|A_2|^2 + |B_2|^2 + 2\Re\{A_2 B_2^* e^{i2w_2 z}\} \Big) dz + \\
& \epsilon_1 \int_0^{(1-\sigma)d_1} \Big(|A_3|^2 + |B_3|^2 + 2\Re\{A_3 B_3^* e^{i2w_1 z}\} \Big) dz \Bigg\} = \\
= V_{mod}^{ext} + \frac{1}{1-e^{-2k\Lambda}} \Bigg\{ & \epsilon_1 (|A_1|^2 + |B_1|^2)\sigma d_1 + \Im\left\{ \frac{A_1 B_1^*}{w_1} \Big(e^{i2w_1 \sigma d_1} - 1 \Big) \right\} + \quad \text{(A.110)} \\
& \epsilon_2 (|A_2|^2 + |B_2|^2) d_2 + \Im\left\{ \frac{A_2 B_2^*}{w_2} \Big(e^{i2w_2 d_2} - 1 \Big) \right\} + \quad \text{(A.111)} \\
& \epsilon_1 (|A_3|^2 + |B_3|^2)(1-\sigma) d_1 + \Im\left\{ \frac{A_3 B_3^*}{w_1} \Big(e^{i2w_1 (1-\sigma) d_1} - 1 \Big) \right\} \Bigg\}. \quad \text{(A.112)}
\end{aligned}$$

[1] This expression is taken from [90], where the ratio between the phase and group velocities v_p/v_g was simplified by assuming negligible chromatic dispersion, at least in the relevant wavelength range.

Inserting the expressions for the amplitudes in equations (A.89, A.91), with an explicit dependence on E_e^-, allows one to factorize E_e^- and invert the formula. The procedure is trivial, but also lengthy, and the final expression will not be reported here. In all the relevant sections in this thesis, the expression was evaluated numerically to enforce mode normalization.

A.7 Electric field at the surface

It is worth noting that the closed expression for the external field given in eq. (A.84), *i.e.*

$$E_{ext}(z) = E_e^- e^{w_e z}, \tag{A.113}$$

depends only on the transversal component of the wave vector w_e and the normalization constant E_e^-. Once these have been fixed, the value of the electric field at the surface, S_{BSW} is simply given by

$$S_{BSW} = \sqrt{\frac{K_{eV\to J}}{\epsilon_0}} B, \tag{A.114}$$

where the vacuum permittivity $\epsilon_0 = 8.85 \times 10^{-18}$ and the conversion constant $K_{eV\to J} = 1.6 \times 10^{-19}$ have been taken into account to calculate fields in units of V/m.

A.8 Calculation of the truncation factor σ

When one deals with one-dimensional photonic crystals, the choice of the unit cell is totally arbitrary. However, the structures analyzed in the previous sections are only *semi-infinite*, *i.e.* they extend indefinitely only in the $(0, +\infty)$ region. Thus, different unit cells may lead to different truncations. In solid-state physics, the Kronig-Penney model[91] is an extremely simplified model of an electron in a one-dimensional periodic potential which however manages to foresee the appearance of bands of allowed energies and especially forbidden bands between them where no states may exist, referred to as *band-gaps*. Introducing defects in the periodicity breaks the translational invariance and may cause new states to appear in the previously forbidden bands. We can incorporate the same reasoning in the photonic realm.

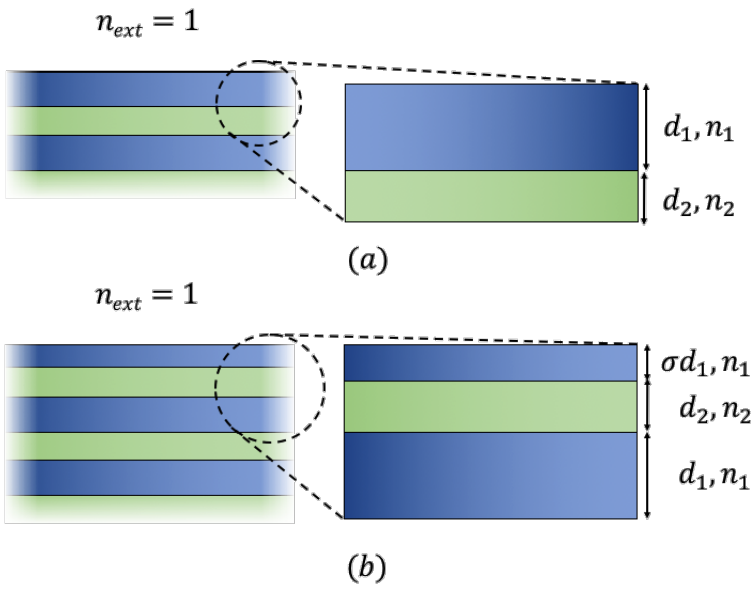

Figure A.8: Semi-infinite multilayer structures having the same bulk properties but different truncations.

For example, a unit cell such as the one shown in fig. (A.8b) gives rise to a semi-infinite bulk photonic crystal alternating layers (d_1, n_1) and (d_2, n_2), exactly as the one in fig. (A.8a), but also to a truncation factor of thickness σd_1 and refractive index n_1, which may introduce spurious modes inside the otherwise forbidden band-gap. In this section, we will dwell on some features of the truncation factor σ and especially on its derivation.

To start with, let us work out the relationship between the transfer matrix M for structure (A.8a) and that for structure (A.8b), M_σ.

The semi-infinite 1D multilayer is periodic, therefore, from Bloch's theorem, we can derive the following identity

$$\begin{pmatrix} M_{11} & M_{12} \\ M_{12}^* & M_{11}^* \end{pmatrix} \begin{pmatrix} a_0 \\ b_0 \end{pmatrix} = e^{ik_{Bloch}\Lambda} \begin{pmatrix} a_0 \\ b_0 \end{pmatrix}, \tag{A.115}$$

where $\Lambda = d_1 + d_2$ is the multilayer period and $e^{ik_{Bloch}\Lambda}$ is the eigenvalue of the transfer matrix M. The calculation of the matrix entries is rather straightforward, and follows directly from the definitions given in eq.s (A.15, A.8):

$$M = \frac{1}{t_{12}t_{21}} \begin{pmatrix} e^{iw_1d_1} & 0 \\ 0 & e^{-iw_1d_1} \end{pmatrix} \begin{pmatrix} 1 & r_{12} \\ r_{12} & 1 \end{pmatrix} \begin{pmatrix} e^{iw_2d_2} & 0 \\ 0 & e^{-iw_2d_2} \end{pmatrix} \begin{pmatrix} 1 & r_{21} \\ r_{21} & 1 \end{pmatrix}; \tag{A.116}$$

now, we employ the Fresnel coefficients' identities $t_{ij} = 1 + r_{ij}$ and $r_{ij} = -r_{ji}$ to obtain

$$M = \frac{1}{1 - r_{12}^2} \begin{pmatrix} e^{iw_1d_1}\left(e^{iw_2d_2} - r_{12}^2 e^{-iw_2d_2}\right) & -2ir_{12}e^{iw_1d_1}\sin(w_2d_2) \\ 2ir_{12}e^{-iw_1d_1}\sin(w_2d_2) & e^{-iw_1d_1}\left(e^{-iw_2d_2} - r_{12}^2 e^{iw_2d_2}\right) \end{pmatrix} \tag{A.117}$$

We can now focus on the the second structure, namely the one in fig. (A.8b), with the truncation layer σd_1 shown explicitly. In this case, the transfer matrix for the first unit cell M_σ can be written as

$$M_\sigma = \Phi_\sigma^{-1}\Phi_1 I_{12}\Phi_2 I_{21}\Phi_\sigma = \Phi_\sigma^{-1} M \Phi_\sigma, \tag{A.118}$$

where Φ_σ is the propagation matrix relative to the truncation layer, *i.e.*

$$\Phi_\sigma = \begin{pmatrix} e^{iw_1\sigma d_1} & 0 \\ 0 & e^{-iw_1\sigma d_1} \end{pmatrix}, \tag{A.119}$$

Even in this case, we can apply Bloch's theorem to get

$$M_\sigma \begin{pmatrix} a_\sigma \\ b_\sigma \end{pmatrix} = \Phi_\sigma^{-1} M \Phi_\sigma \begin{pmatrix} a_\sigma \\ b_\sigma \end{pmatrix} = e^{ik_{Bloch}\Lambda} \begin{pmatrix} a_\sigma \\ b_\sigma \end{pmatrix}, \tag{A.120}$$

and, comparing eq. (A.115) and eq. (A.120) we deduce

$$\Phi_\sigma \begin{pmatrix} a_\sigma \\ b_\sigma \end{pmatrix} = \begin{pmatrix} a_0 \\ b_0 \end{pmatrix} \implies \begin{pmatrix} a_\sigma \\ b_\sigma \end{pmatrix} = \Phi_\sigma^{-1} \begin{pmatrix} a_0 \\ b_0 \end{pmatrix}. \tag{A.121}$$

According to eq. (A.118), matrices M and M_σ are similar, and thus they represent the same transformation written in different bases. Since all the properties relative to the linear transformation are conserved under a change of basis, the characteristic polynomial and its derived properties, the eigenvalues, the trace and the determinant of the matrices will be the same. In particular, as was already pointed out in section (A.3), the photonic band structure depends on the eigenvalues of the transfer matrix, and is thus independent of the basis the operator was written in.

The field cannot propagate into the dielectric external medium because of total internal reflection, therefore

$$\frac{1}{t_{e1}} \begin{pmatrix} 1 & r_{e1} \\ r_{e1} & 1 \end{pmatrix} \begin{pmatrix} a_\sigma \\ b_\sigma \end{pmatrix} = \begin{pmatrix} 0 \\ E_e^- \end{pmatrix}. \tag{A.122}$$

Multiplying the first row of the matrix yields

$$a_\sigma = r_{1e} b_\sigma. \tag{A.123}$$

We can now plug the definition of Φ_σ^{-1} in eq. (A.121) and carry out the following product:

$$\begin{pmatrix} a_\sigma \\ b_\sigma \end{pmatrix} = \begin{pmatrix} e^{-iw_1\sigma d_1} a_0 \\ e^{iw_1\sigma d_1} b_0 \end{pmatrix}, \tag{A.124}$$

which can finally be inserted in eq. (A.123) to get

$$\frac{b_0}{a_0} r_{1e} e^{i2w_1\sigma d_1} = 1. \tag{A.125}$$

The definition of the Fresnel reflection coefficient given in eq. (A.54), *i.e.*

$$r_{1e} = \frac{w_1 - w_e}{w_1 + w_e}. \tag{A.126}$$

can be inverted to get

$$w_e = w_1 \frac{1 - r_{1e}}{1 + r_{1e}}. \tag{A.127}$$

The field is evanescent in the external dielectric medium, so $w_e = iq_e \in \mathbb{C}/\mathbb{R}$ and we can write

$$q_e = iw_1 \frac{r_{1e} - 1}{r_{1e} + 1}, \tag{A.128}$$

Recalling eq. (A.123), this equation becomes

$$q_e = iw_1 \frac{a_\sigma - b_\sigma}{a_\sigma + b_\sigma}. \tag{A.129}$$

We can now employ eq. (A.124) to convert this equation from a relation linking a_σ and b_σ to one linking a_0 and b_0, *i.e.*

$$q_e = iw_1 \frac{a_0 - b_0 e^{i2w_1\sigma d_1}}{a_0 + b_0 e^{i2w_1\sigma d_1}}. \tag{A.130}$$

Finally, we can plug in $b_0 = \frac{a_0}{M_{12}} \left(e^{ik_{Bloch}\Lambda} - M_{11}\right)$ from eq. (A.115) to get

$$q_e = iw_1 \frac{M_{12} e^{-i2w_1\sigma d_1} + M_{11} - e^{ik_{Bloch}\Lambda}}{M_{12} e^{-i2w_1\sigma d_1} - M_{11} + e^{ik_{Bloch}\Lambda}}. \tag{A.131}$$

This last relation can be inverted to obtain a defining equation for the truncation factor σ:

$$\sigma = \frac{i}{2w_1 d_1} \ln\left(\frac{(M_{11} - e^{iKL})(iw_1 + q_e)}{(q_e - iw_1)M_{12}}\right). \tag{A.132}$$

The matrix elements that show up in eq. (A.132) are completely defined in eq. (A.117), and their values are reported here for convenience:

$$M_{11} = \frac{e^{iw_1 d_1}}{1 - r_{12}^2} \left(e^{iw_2 d_2} - r_{12}^2 e^{-iw_2 d_2}\right) \tag{A.133}$$

$$M_{12} = -2ir_{12} e^{iw_1 d_1} \sin(w_2 d_2). \tag{A.134}$$

Appendix B

Slab waveguide modes

Consider the simple asymmetric slab waveguide reported in fig. B.1

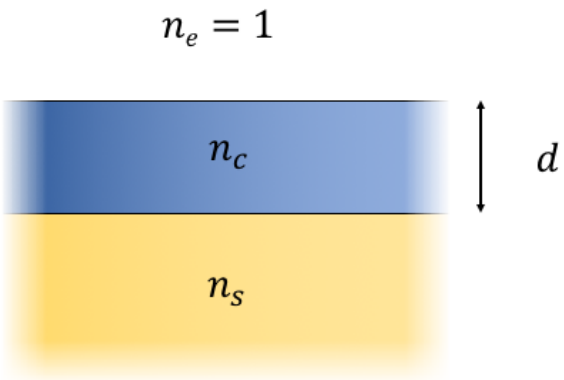

Figure B.1: A general asymmetric slab waveguide.

The slab has core thickness d, and refractive indices n_c for the core, $n_e = 1$ for the external medium and n_s for the substrate; the whole structure is made of dielectric media, which means that the refractive indices are real.

From Pythagora's theorem, the transverse component of the propagation wave vector in each layer is defined according to

$$w_j = \sqrt{(k_0 n_j)^2 - \beta^2}, \tag{B.1}$$

where $k_0 = 2\pi/\lambda_0$ and β is the component of the propagation wave vector parallel to the interfaces.

We are interested in guided modes, therefore, from physical consideration, we know that

$$w_e = iq, \tag{B.2}$$
$$w_c = h, \tag{B.3}$$
$$w_s = ip, \tag{B.4}$$

where[1]

$$q = \sqrt{\beta^2 - (k_0 n_e)^2}, \tag{B.5}$$

$$h = \sqrt{(k_0 n_c)^2 - \beta^2}, \tag{B.6}$$

$$p = \sqrt{\beta^2 - (k_0 n_s)^2}. \tag{B.7}$$

Thus, for s-polarized modes we can write, from eq. (A.9),

$$r_{ce} = \frac{h - iq}{h + iq} \tag{B.8}$$

$$r_{cs} = \frac{h - ip}{h + ip}. \tag{B.9}$$

From the mode condition worked out in eq. (A.48), we get

$$1 - \frac{h - iq}{h + iq}\frac{h - ip}{h + ip}e^{2ihd} = 0, \tag{B.10}$$

or

$$e^{2ihd} = \frac{h + iq}{h - iq}\frac{h + ip}{h - ip}. \tag{B.11}$$

At this point, it would be sufficient to equate the real part of the left-hand side of the equation to the real part of the right-hand side, and likewise for the imaginary part. However, in order to simplify the calculations, the equation can be rewritten with a slight variation:

$$e^{2ihd} + 1 = \frac{h + iq}{h - iq}\frac{h + ip}{h - ip} + 1. \tag{B.12}$$

This leads to

$$\cos(2hd) + i \cdot \sin(2hd) + 1 = \frac{(h + iq)(h + ip) + (h - ip)(h - iq)}{(h - ip)(h - iq)} \tag{B.13}$$

$$= \frac{(h + iq)(h + ip) + (h - ip)(h - iq)}{(h + p^2)(h + q^2)}(h + ip)(h + iq) \tag{B.14}$$

$$= \frac{2(h^2 - qp)}{(h + p^2)(h + q^2)}(h^2 - qp + i(qh + ph)). \tag{B.15}$$

Instead of equating directly as explained above, one can resort to a trick and equate the ratio of the imaginary part to the real part of the LHS to that on the RHS:

$$\frac{\sin(2hd)}{\cos(2hd) + 1} = \frac{qh + ph}{h^2 - qp}. \tag{B.16}$$

[1]The concepts reported in this Appendix follow the notation in [48].

Now, remembering that

$$\tan(x) = \frac{\sin(2x)}{1+\cos(2x)}, \tag{B.17}$$

we can finally write the dispersion relation for the TE modes in an asymmetric slab waveguide:

$$\tan(hd) = \frac{qh+ph}{h^2-qp}. \tag{B.18}$$

Thus, as the core thickness d increases, the asymmetric slab can support more modes. In order for the slab to support m-th TE mode, one can invert eq. (B.19), substitute the wave vector definitions in eq. (B.5, B.6, B.7) and define a cut-off thickness [48] given by

$$\frac{d}{\lambda_0} = \frac{1}{2\pi\sqrt{n_c^2-n_s^2}}\left[m\pi + \arctan\sqrt{\frac{n_s^2-n_e^2}{n_c^2-n_s^2}}\right]. \tag{B.19}$$

B.1 Modal length of the TE0 mode

The *modal length* of a guided mode is defined in general as

$$L_{mod} = \frac{1}{\varepsilon_{max}|E_{max}|^2}\int_{-\infty}^{\infty}|E(z)|^2\varepsilon(z)dz \tag{B.20}$$

The fundamental TE mode in an asymmetrical slab waveguide can be parametrized as [48]

$$E_m(z) = \begin{cases} e^{-qz}, & \text{if } z \geq 0 \\ C(\cos(hz) - \frac{q}{h}\sin(hz)), & \text{if } -d \leq z < 0 \\ C(\cos(hd) + \frac{q}{h}\sin(hd))e^{p(z+d)}, & \text{if } -d \leq z < 0 \end{cases} \tag{B.21}$$

where C is a normalization constant and q, h and p are the wave vector components perpendicular to the interfaces defined in eq. (B.5, B.6, B.7). To calculate C, one must impose that the mode transports the energy of a photon, *i.e.*

$$A\int_{-\infty}^{+\infty}|E(z)|^2\varepsilon(z)dz = \frac{\hbar\omega}{2} \tag{B.22}$$

where $A = 1\ \mathrm{m}^2$ is a transversal area necessary for the proper normalization of the field. From eq. (B.21) and (B.23), one can immediately deduce

$$C = \sqrt{\frac{\hbar\omega}{2(I_e+I_c+I_s)}}, \tag{B.23}$$

where I_s, I_c and I_e are the integrals of the fields times the dielectric functions over the relevant ranges, as given by eq. (B.21). The calculation is trivial, and the results are

$$I_e = \frac{\varepsilon_e}{2q} \tag{B.24}$$

$$I_s = \frac{\varepsilon_s[\cos(hd) + \frac{q}{h}\sin(hd)]^2}{2p} \tag{B.25}$$

$$I_c = \frac{\varepsilon_c}{2}\left[d + \frac{\sin(2hd)}{2h} + \frac{q^2}{h^2}\left(d - \frac{\sin(2hd)}{2h}\right) + \right.$$
$$\left. + \frac{q}{h^2}\Big(1 - \cos(2hd)\Big)\right]. \tag{B.26}$$

The maximum of the field modulus square of the fundamental TE mode will occur inside the core region. To find this, we can derive eq. (B.26) and set the derivative equal to 0 to find the location of the maximum. Substituting this back into the equation yields a value

$$E_{max} = C\frac{\sqrt{h^2 + q^2}}{h} \tag{B.27}$$

Altogether, the modal length in eq. (B.20) becomes

$$L_{mod} = \frac{h}{\varepsilon_c(h^2 + q^2)}(I_e + I_c + I_s). \tag{B.28}$$

Appendix C

Basics of light confinement

Light confinement in dielectric structures can be mainly ascribed to two different physical principles, namely *total internal reflection* and the presence of a *photonic band-gap*. In the following sections, the basic theory underlying these two phenomena will be developed.

As a common hypothesis to both topics, it will be assumed that we are working with linear, homogeneous and isotropic media. In this case, the solutions of Maxwell's equations can have plane-wave form,

$$\mathbf{E}(\mathbf{r},t) = \mathbf{E}e^{i\mathbf{k}\cdot\mathbf{r}}e^{-i\omega t} + c.c. \tag{C.1}$$

If the media involved are homogeneous and isotropic, then the wave vector $\mathbf{k}$ is linked to the frequency via the *dispersion relation*

$$k^2 - \frac{\omega^2}{c^2}n^2 = 0. \tag{C.2}$$

C.1 Total internal reflection (TIR)

Assume a light wave is traveling through a medium of refractive index n_1 with a propagation vector

$$\mathbf{k} = \omega/c\hat{k} = \frac{2\pi n_1}{\lambda_0}\hat{k}, \tag{C.3}$$

where λ_0 is the wavelength of light in vacuum, linked to the photon energy via

$$E = \frac{hc}{\lambda_0} \approx \frac{1.23984\ldots}{\lambda_0\ (\mu\text{m})}\ \text{eV}\cdot\mu\text{m}, \tag{C.4}$$

when it strikes an interface with another medium of refractive index $n_2 < n_1$.

Without loss of generality, assume that the interface lies in the z plane, and that the plane of incidence is the $x-z$ plane.

Light impinging on an interface between two media typically gives rise to both a *reflected* and a *refracted* wave[92, 48].

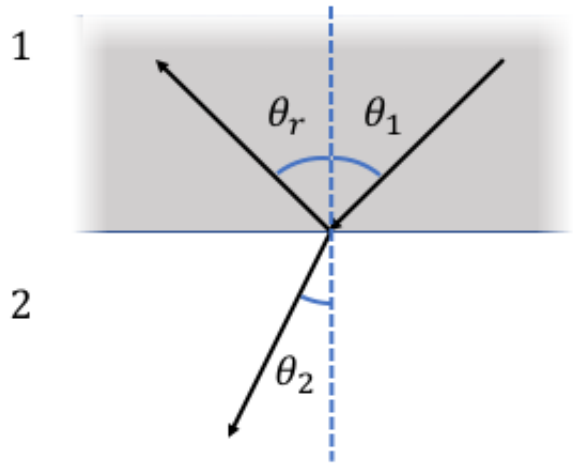

Figure C.1: A light ray strikes a plane interface between two media with an angle θ_1 and is both reflected (angle θ_r) and refracted (angle θ_2); all the angles are conventionally measured with respect to the interface normal. The angle of incidence is θ_1, while the angle of refraction is θ_2

This behavior is easily summarized by two equations. The first, the so-called *law of reflection*, simply states that

$$\theta_r = \theta_1, \tag{C.5}$$

i.e. the incoming and outgoing angles are the same as measured from the surface normal.

As to refraction, if the interface is planar and homogeneous, at least at the scale of the wavelength of light, the in-plane component of the propagation vector, namely $k_{\parallel} = (k_x, 0, 0)$ must be conserved. This in turn implies

$$k_{1,x} = k_{2,x} \tag{C.6}$$

$$n_1 \sin(\theta_1) = n_2 \sin(\theta_2), \tag{C.7}$$

which is the renowned *Snell's law* of optics.

According to eq.(C.7), the angle of refraction θ_2 must satisfy this identity:

$$\sin\theta_2 = \frac{n_1}{n_2}\sin\theta_i \tag{C.8}$$

$$\theta_2 = \arcsin\left[\frac{n_1}{n_2}\sin\theta_i\right] \tag{C.9}$$

Thus, whenever the argument of the inverted sine in (C.9) is greater than unity, the formula ceases to yield angles for the refracted light ray. The equation can then be used to derive a threshold condition, as refracted light can at the most propagate along the interface between the two media, *i.e.* at 90° with respect

to the interface normal $\hat{z}$. The incoming angle θ_1 for which $\theta_2 = 90° = \pi/2$ is known as *critical angle* θ_c:

$$\theta_c = \arcsin \frac{n_2}{n_1}; \tag{C.10}$$

Whenever $\theta_i > \theta_c$, no refracted ray emerges from the interface, and light is confined in the first medium. In this scenario, we say that light undergoes *total internal reflection*[1].

The same situation can be analyzed in terms of wave vectors. According to eq. (C.3), light is traveling in medium n_1 with a wave vector $\mathbf{k_1} = \mathbf{k_0} n_1$. This vector can be decomposed in two independent components $\mathbf{k_x}$ and $\mathbf{k_y}$ whose moduli satisfy

$$k_1^2 = k_{1,x}^2 + k_{1,z}^2, \tag{C.11}$$

or[2]

$$k_{1,z} = \sqrt{k_1^2 - k_{1,x}^2}. \tag{C.12}$$

Likewise, the propagation vector in the second medium satisfies

$$k_2^2 = k_{2,x}^2 + k_{2,z}^2. \tag{C.13}$$

From equations (C.11) and (C.13), we can already deduce the *TIR* condition we derived earlier by simply assuming no component of the propagation wave vector in medium n_2 along $\hat{z}$, *i.e.*

$$k_{2,z} = 0 \tag{C.14}$$

$$k_{2,x} = k_2 = k_{1,x} \tag{C.15}$$

$$n_1 \sin(\theta_1) = n_2 \sin(\theta_2). \tag{C.16}$$

But we can even go further and recognize that, for each medium, the decomposition given in eq. (C.12) allows us to split the energy-wave vector plane in two regions, as shown in fig. C.2.

The dashed blue line corresponds to the set of point for which eq. C.14 holds, i.e.

$$k_{2,z} = \sqrt{k_2^2 - k_{2,x}^2} = 0; \tag{C.17}$$

likewise, the dotted blue line corresponds to the condition $k_{1,z} = 0$. These lines are known as *light lines*, as they separate regions where $k_z^2 > 0$, to their lefts, from regions where $k_z^2 < 0$, to their rights. If we recall the plane-wave form of the solutions to Maxwell's equation given in eq. C.1, it is straightforward to notice that $\Im k_z \neq 0$, *i.e.* whenever k_x lies to the right of the light line corresponding to medium n_j, implies that the electric field in the corresponding layer will undergo exponential decay in the transversal direction, as

$$\mathbf{E}(\mathbf{r}, t) = \mathbf{E} e^{i\mathbf{k}\cdot\mathbf{r}} e^{-i\omega t} + c.c. \propto \mathbf{E} e^{-\Im[k_z] z} \tag{C.18}$$

[1] If the situation were reversed and light were traveling in the lighter medium, *i.e.* $n_1 < n_2$, then the n_2/n_1 ratio would be smaller than unity and no critical angle θ_c would exist.

[2] Here and in the following sections the sign of the square root will be chosen so that the imaginary part of k_z satisfies $\Im k_z \geq 0$; if $\Im k_z = 0$, then we choose $\Re k_z > 0$

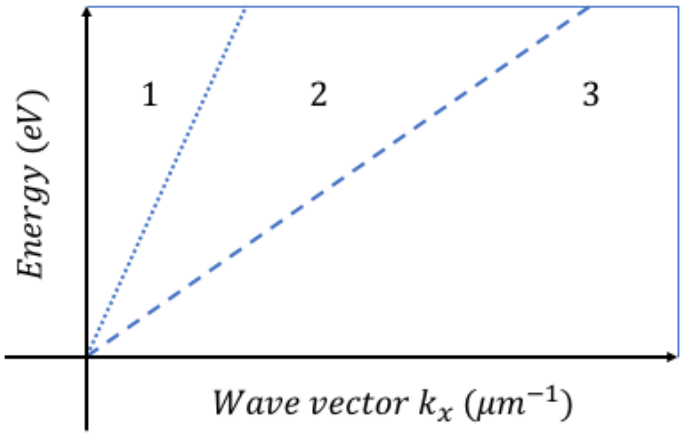

Figure C.2: The energy-wavevector plane showing ith two light lines for media n_1 (dotted) and n_2 (dashed).

C.2 Photonic band gap (PBG)

As is well known from basic solid state theory, crystals, *i.e.* highly ordered structures in which the potential is periodic in at least one dimension, may show the presence of an electronic band gap, an energy range in which electrons cannot propagate inside the crystal[93].

Much as semiconductors control electrons, structure with periodic optical properties can be employed to control photons. *Photonic crystals* were discovered in the late 1980s in two seminal works by Yablonovitch[94], then at Bell Communications Research, and John[95], then at Princeton University.

Yablonovitch's goal in his 1987 *Physical Review Letters* paper was to investigate this new field to somehow dam losses arising from light being emitted at unwanted frequencies or directions in many optical devices, such as semiconductor lasers. The breakthrough was the observation that carving a transparent medium in order to create an artificially periodic structure would induce a behavior analogous to a crystal lattice; in this case, however, the periodicity would be appointed to the refractive indices of the materials.

Indeed, *photonic band gaps*, *i.e.* energy regions for which light propagation inside a periodic structure is forbidden, arise due to electromagnetic waves interfering inside the device[96, 31, 1, 97]. Much of the initial interest was in three-dimensional photonic band gaps, which in Yablonovitch's own words are *"a frequency band in three-dimensional dielectric structures in which electromagnetic waves are forbidden irrespective of the propagation direction in space"*[94], but even lower-dimensional PBGs can find applications in controlling the propagation of light in photonic crystals.

Though Yablonovitch's interest was mainly focused on 3D photonic crystals, due to the *completeness* of their photonic band gaps, in the following chapters my focus will be on 1D photonic crystals. More in detail, the main object of my research will be based on the repetition of a *bilayer* unit cell.

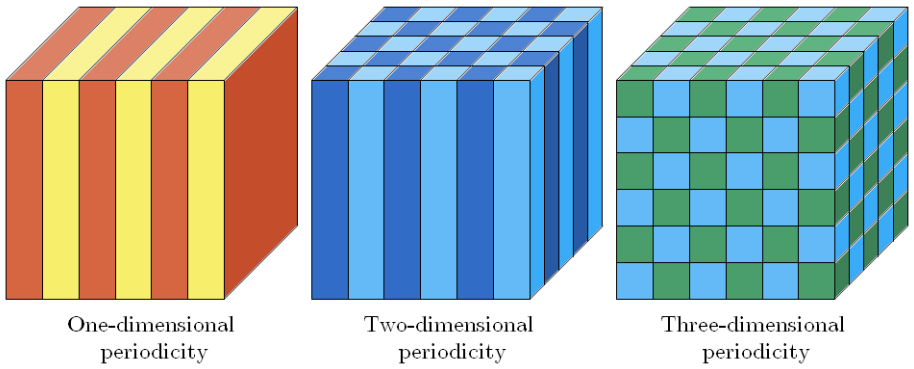

Figure C.3: Examples of 1-, 2- and 3-dimensional photonic crystals, *i.e.* structures characterized by a periodic repetition of dielectric materials along one or more axes; different refractive indices are mapped onto different colours.

Nature also boasts striking examples of photonic crystals. One such example are opals, *i.e.* mineraloids formed by successive depositions of silicon dioxide from silica-rich water. Some insects, such as members of the *Morpho* or *Polyommatus* butterfly genus, arthropods of the *Pachyrrhynchus* and *Hoplia* genus and even more complex animals such as peacocks, *Pavo cristatus*, all owe their iridescent colours to *structural coloration* instead of more common pigments.

All the naturally occurring photonic crystals mentioned up to now all feature a lattice constant comparable to the wavelength of visible light. However, artificial photonic crystals can be designed and fabricated so as to tailor the interaction between light and the microscopically structured device by varying the lattice constant, the structure of the lattice or the refractive index of the materials involved. This causes the photonic band gap to shift in the energy-wave vector plane, leading the condition for constructive or destructive interference to shift as well and changing the structural coloration.

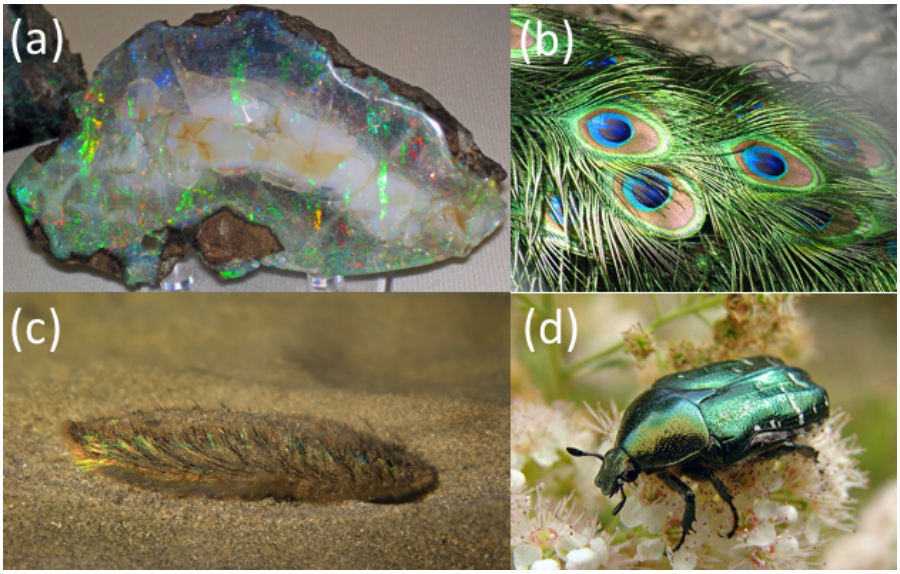

Figure C.4: Naturally occurring photonic crystals: (a) an iridescent opal encased in a rock matrix; (b) dark *ocelli* on peacock feathers; (c) the marine polychaete worm *Aphrodita aculeata*; (d) *Rose chafer* adult beetle (*Cetonia aurata*). All pictures were taken from the Wikimedia Foundation website (https://commons.wikimedia.org/).

Appendix D

On semi-infinite structures

When doing calculations involving periodic multilayers, one might be interested in understanding the limiting behaviour of its optical response as the number of periods N goes to infinity.

For instance, consider the structure shown in fig. D.1, *i.e.* a multilayer built with the repetition of a two-layer unit cell (n_a, d_a and n_b, d_b). Imagine inserting a infinitesimally thin air buffer between each unit cell.

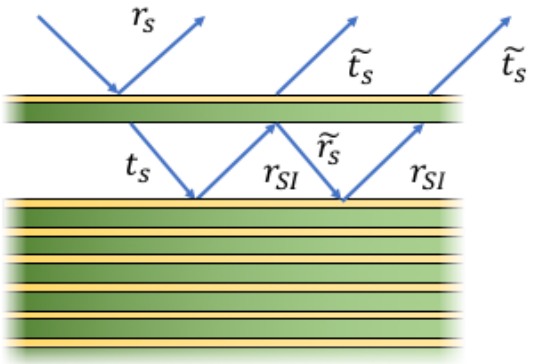

Figure D.1: A semi-infinite periodic multilayer resulting from the repetition of a single bilayer unit cell. A thin layer of air has been inserted between the first unit cell and the bulk multilayer.

As sketched in fig. D.1, the overall reflection coefficient of the whole semi-infinite multilayer is the sum of various contributions:

1. Light reflected by the first unit cell (r_S);

2. Light transmitted by the first unit cell (t_S), then reflected by the underlying structure (which is the whole semi-infinite multilayer, thus r_{SI}) and then transmitted by the inverse unit cell ($\tilde{t_S}$);

3. Light transmitted by the first unit cell (t_S), then reflected by the underlying structure (r_{SI}), then reflected by the inverse unit cell above ($\tilde{r_s}$), reflected again by the semi-infinite structure (r_{SI}) and then transmitted by the inverse unit cell ($\tilde{t_S}$);

4. ...

Thus, all in all, the reflection coefficient is

$$r_{SI} = r_s + t_s r_{SI} \tilde{t_s} + t_s r_{SI} \tilde{r_s} r_{SI} \tilde{t_s} + ... = \quad = r_s + t_s r_{SI} \tilde{t_s} \left(1 + \tilde{r_s} r_{SI} + ...\right) = = r_s + t_s r_{SI} \tilde{t_s} \frac{1}{1 - \tilde{r_s} r_{SI}} \tag{D.1}$$

This implicit formula can be further developed:

$$r_{SI} \left(1 - \tilde{r_s} r_{SI}\right) = r_s \left(1 - \tilde{r_s} r_{SI}\right) + t_s r_{SI} \tilde{t_s} 0 = -r_{SI} + \tilde{r_s} r_{SI}^2 + r_s - r_s \tilde{r_s} r_{SI} + t_s r_{SI} \tilde{t_s} 0 = \tilde{r_s} r_{SI}^2 - r_{SI} \left(\tag{D.2}$$

The overall reflection coefficient r_{SI} can then be found by solving the second-degree equation $\Delta = \left(1 + t_s \tilde{t_s} - r_s \tilde{r_s}\right)^2 - 4 r_s \tilde{r_s}$. This yields

$$r_{SI}^{\pm} = \frac{\left(1 + t_s \tilde{t_s} - r_s \tilde{r_s}\right) \pm \sqrt{\left(1 + t_s \tilde{t_s} - r_s \tilde{r_s}\right)^2 - 4 r_s \tilde{r_s}}}{2 \tilde{r_s}} \tag{D.3}$$

The modes supported by the semi-infinite periodic multilayer can finally be found by looking for the poles of eq. (D.3), *i.e.* where $\tilde{r_s} = 0$.

This result shows that the modes supported by a semi-infinite one-dimensional photonic crystal can be found by considering the unit cell, inverting it, and calculating the transmittance poles of this inverted structure.

Bibliography

[1] P. Yeh, A. Yariv, and A. Y. Cho. Optical surface waves in periodic layered media. *Appl. Phys. Lett.*, 32:104–105, 1978.

[2] A.Y. Cho, A. Yariv, and P. Yeh. Observation of confined propagation in bragg waveguides. *Applied Physics Letters*, 30(9):471–472, 1977. cited By 57.

[3] Amnon Yariv, Pochi Yeh, and Chi-Shain Hong. Electromagnetic propagation in periodic stratified media. *Journal of the Optical Society of America*, 67(4):423–438, 1977.

[4] R. D. Meade, A. Devenyi, J. D. Joannopoulos, O. L. Alerhand, D. A. Smith, and K. Kash. Novel applications of photonic band gap materials: low-loss bends and high q cavities. *J. Appl. Phys.*, 75:4753–4755, 1994.

[5] W.M. Robertson and M.S. May. Surface electromagnetic wave excitation on one-dimensional photonic band-gap arrays. *Applied Physics Letters*, 74(13):1800–1802, 1999. cited By 145.

[6] W.M. Robertson, G. Arjavalingam, R.D. Meade, K.D. Brommer, A.M. Rappe, and J.D. Joannopoulos. Observation of surface photons on periodic dielectric arrays. *Optics Letters*, 18(7):528–530, 1993. cited By 105.

[7] M. Liscidini and J.E. Sipe. Enhancement of diffraction for biosensing applications via bloch surface waves. *Appl. Phys. Lett.*, 91(253125), 2007.

[8] Krishanu Ray, Ramachandram Badugu, and Joseph R Lakowicz. Bloch surface wave-coupled emission from quantum dots by ensemble and single molecule spectroscopy. *RSC advances*, 5(67):54403–54411, 2015.

[9] Marco Liscidini, Matteo Galli, Molu Shi, Giacomo Dacarro, Maddalena Patrini, Daniele Bajoni, and J. E. Sipe. Strong modification of light emission from a dye monolayer via bloch surface waves. *Opt. Lett.*, 34(15):2318–2320, Aug 2009.

[10] Robert D. Meade, Karl D. Brommer, Andrew M. Rappe, and J. D. Joannopoulos. Electromagnetic bloch waves at the surface of a photonic crystal. *Phys. Rev. B*, 44:10961, 1991.

[11] Marco Liscidini and John E. Sipe. Analysis of bloch-surface-wave assisted diffraction-based biosensors. *Journal of the Optical Society of America B*, 26(2), 2009.

[12] E. M. Purcell. Spontaneous emission probabilities at radio frequences. *Physical Review*, 69(11-12), 1946. Proceedings of the American Physical Society (B10).

[13] Marco Liscidini. Surface guided modes in photonic crystal ridges: the good, the bad, and the ugly. *J. Opt. Soc. Am. B*, 29(8):2103–2109, Aug 2012.

[14] E. Descrovi, T. Sfez, M. Quaglio, D. Brunazzo, L. Dominici, F. Michelotti, H. P. Herzig, O. J. F. Martin, and F. Giorgis. Guided bloch surface waves on ultrathin polymeric ridges. *Nano Letters*, 10(6):2087–2091, 2010.

[15] R. Dubey, B. Vosoughi Lahijani, E. Barakat, M. Häyrinen, M. Roussey, M. Kuittinen, and H. P. Herzig. Near-field characterization of a bloch-surface-wave-based 2d disk resonator. *Optics Letters*, 41(21):4867–4870, 2016.

[16] M. Menotti and M. Liscidini. Optical resonators based on bloch surface waves. *Journal of the Optical Society of America B: Optical Physics*, 32(3):431–438, 2015.

[17] Yoshihiro Akahane, Takashi Asano, Bong-Shik Song, and Susumu Noda. High-q photonic nanocavity in a two-dimensional photonic crystal. *Nature*, 425:944–947, 2003.

[18] Bong-Shik Song, Susumu Noda, Takashi Asano, and Yoshihiro Akahane. Ultra-high-q photonic double-heterostructure nanocavity. *Nature Materials*, 4:207–210, 2005.

[19] Eiichi Kuramochi, Masaya Notomi, Satoshi Mitsugi, Akihiko Shinya, Takasumi Tanabe, and Toshifumi Watanabe. Ultrahigh-q photonic crystal nanocavities realized by the local width modulation of a line defect. *Applied Physics Letters*, 88(4):041112, 2006.

[20] Kartik Srinivasan, Paul E. Barclay, and Oskar Painter. Fabrication-tolerant high quality factor photonic crystal microcavities. *Opt. Express*, 12(7):1458–1463, Apr 2004.

[21] J. Topolancik, F. Vollmer, and B. Ilic. Random high-q cavities in disordered photonic crystal waveguides. *Applied Physics Letters*, 91(20):201102, 2007.

[22] K. Hennessy, A. Badolato, M. Winger, D. Gerace, M. Atatüre, S. Gulde, S. Fält, E. L. Hu, and A. Imamoğlu. Quantum nature of a strongly coupled single quantum dot cavity system. *Nature*, 445:896, 2007.

[23] T. Yoshie, A. Scherer, J. Hendrickson, G. Khitrova, H. M. Gibbs, G. Rupper, C. Ell, O. B. Shchekin, and D. G. Deppe. Vacuum rabi splitting with a single quantum dot in a photonic crystal nanocavity. *Nature*, 432:200, 2004.

[24] Jelena Vučković, Marko Lončar, Hideo Mabuchi, and Axel Scherer. Design of photonic crystal microcavities for cavity qed. *Phys. Rev. E*, 65:016608, Dec 2001.

[25] Marko Lončar, Axel Scherer, and Yueming Qiu. Photonic crystal laser sources for chemical detection. *Applied Physics Letters*, 82(26):4648–4650, 2003.

[26] Takasumi Tanabe, Masaya Notomi, Satoshi Mitsugi, Akihiko Shinya, and Eiichi Kuramochi. All-optical switches on a silicon chip realized using photonic crystal nanocavities. *Applied Physics Letters*, 87(15):151112, 2005.

[27] Marko Lončar, Tomoyuki Yoshie, Axel Scherer, Pawan Gogna, and Yueming Qiu. Low-threshold photonic crystal laser. *Applied Physics Letters*, 81(15):2680–2682, 2002.

[28] Gilberto A. Rodriguez, John D. Lonai Raymond L Mernaugh, and Sharon M Weiss. Porous silicon bloch surface and sub-surface wave structure for simultaneous detection of small and large molecules. *Nanoscale Res. Lett.*, 9:383, 2014.

[29] Daniele Aurelio and Marco Liscidini. Electromagnetic field enhancement in bloch surface waves. *Phys. Rev. B*, 96:045308, Jul 2017.

[30] Hajar Kaviani Baghbadorani, Daniele Aurelio, Jamal Barvestani, and Marco Liscidini. Guided modes in photonic crystal slabs supporting bloch surface waves. *J. Opt. Soc. Am. B*, 35(4):805–810, Apr 2018.

[31] Pochi Yeh, Amnon Yariv, and Chi-Shain Hong. Electromagnetic propagation in periodic stratified media. i. general theory. *J. Opt. Soc. Am.*, 67(4):423–438, Apr 1977.

[32] X.-B. Kang, L.-J. Liu, H. Lu, H.-D. Li, and Z.-G. Wang. Guided bloch surface wave resonance for biosensor designs. *Journal of the Optical Society of America A: Optics and Image Science, and Vision*, 33(5):997–1003, 2016.

[33] F. Giorgis, E. Descrovi, C. Summonte, L. Dominici, and F. Michelotti. Experimental determination of the sensitivity of bloch surface waves based sensors. *Optics Express*, 18(8):8087–8093, 2010.

[34] E. Kretschmann and H. Raether. Radiative decay of non radiative surface plasmons excited by light. *Zeitschrift für Naturforschung A*, 23(12):2135–2136, 1968.

[35] M. Liscidini, M. Galli, M. Shi, G. Dacarro, M. Patrini, D. Bajoni, and J. E. Sipe. Strong modification of light emission from a dye monolayer via bloch surface waves. *Optics Letters*, 34:2318–2320, 2009.

[36] V. Paeder, V. Musi, L. Hvozdara, S. Herminjard, and H.P. Herzig. Detection of protein aggregation with a bloch surface wave based sensor. *Sensors and Actuators, B: Chemical*, 157(1):260–264, 2011. cited By 29.

[37] T. Kitada, H. Ota, X. Lu, N. Kumagai, and T. Isu. Surface emitting devices based on a semiconductor coupled multilayer cavity for novel terahertz light sources. *IEICE Transactions on Electronics*, E100C(2):171–178, 2017.

[38] P. Munzert, N. Danz, A. Sinibaldi, and F. Michelotti. Multilayer coatings for bloch surface wave optical biosensors. *Surface and Coatings Technology*, 314:79–84, 2017.

[39] L. Yu, E. Barakat, T. Sfez, L. Hvozdara, J. Di Francesco, and H.P. Herzig. Manipulating bloch surface waves in 2d: A platform concept-based flat lens. *Light: Science and Applications*, 3:e124, 2014.

[40] Ramachandram Badugu, Kazimierz Nowaczyk, Emiliano Descrovi, and Joseph R. Lakowicz. Radiative decay engineering 6: Fluorescence on one-dimensional photonic crystals. *Analytical Biochemistry*, 442(1):83–96, 2013.

[41] Muhammad Umar Khan and Brian Corbett. Bloch surface wave structures for high sensitivity detection and compact waveguiding. *Science and Technology of Advanced Materials*, 17(1):398–409, 2016.

[42] Kandammathe Valiyaveedu Sreekanth, Shuwen Zeng, Jingzhi Shang, Ken-Tye Yong, and Ting Yu. Excitation of surface electromagnetic waves in a graphene-based bragg grating. *Scientific Reports*, 2:737, 2012.

[43] J. E. Sipe and J. Becher. Surface energy transfer enhanced by optical cavity excitation: a pole analysis. *J. Opt. Soc. Am.*, 72:288–295, 1982.

[44] A. Delfan, M. Liscidini, and J.E. Sipe. Surface enhanced raman scattering in the presence of multilayer dielectric structures. *J. Opt. Soc. Am. B*, 29:1863, 2012.

[45] J. S. Foresi, P. R. Villeneuve, J. Ferrera, E. R. Thoen, G. Steinmeyer, S. Fan, J. D. Joannopoulos, L. C. Kimerling, Henry I. Smith, and E. P. Ippen. Photonic-bandgap microcavities in optical waveguides. *Nature*, 390:143–145, 1997.

[46] Muhammad Umar Khan and Brian Corbett. Bloch surface wave structures for high sensitivity detection and compact waveguiding. *Science and Technology of Advanced Materials*, 17(1):398–409, 2016. PMID: 27877891.

[47] J. Homola. Surface plasmon resonance sensors for detection of chemical and biological species. *Chemical Reviews*, 108(2):462–493, 2008. PMID: 18229953.

[48] Amnon Yariv and Pochi Yeh. *Photonics - Optical Electronics in Modern Communications*. Oxford University Press, Oxford, 2006.

[49] Emiliano Descrovi. Resonant diffraction of symmetric and antisymmetric bloch surface waves on a corrugated periodic multilayer slab. *Opt. Lett.*, 34(13):1973–1975, Jul 2009.

[50] E. Descrovi, T. Sfez, L. Dominici, W. Nakagawa, F. Michelotti, F. Giorgis, and H.-P. Herzig. Near-field imaging of bloch surface waves on silicon nitride one-dimensional photonic crystals. *Optics Express*, 16(8):5453–5464, 2008. cited By 45.

[51] Lucio Claudio Andreani and Dario Gerace. Photonic-crystal slabs with a triangular lattice of triangular holes investigated using a guided-mode expansion method. *Phys. Rev. B*, 73:235114, Jun 2006.

[52] Tristan Sfez, Emiliano Descrovi, Lorenzo Dominici, Wataru Nakagawa, Francesco Michelotti, Fabrizio Giorgis, and Hans-Peter Herzig. Near-field analysis of surface electromagnetic waves in the bandgap region of a polymeric grating written on a one-dimensional photonic crystal. *Applied Physics Letters*, 93(6):061108, 2008.

[53] Emiliano Descrovi, Fabrizio Giorgis, Lorenzo Dominici, and Francesco Michelotti. Experimental observation of optical bandgaps for surface electromagnetic waves in a periodically corrugated one-dimensional silicon nitride photonic crystal. *Opt. Lett.*, 33(3):243–245, Feb 2008.

[54] Gilberto A. Rodriguez, Shuren Hu, and Sharon M. Weiss. Porous silicon ring resonator for compact, high sensitivity biosensing applications. *Opt. Express*, 23(6):7111–7119, Mar 2015.

[55] Alberto Sinibaldi, Riccardo Rizzo, Giovanni Figliozzi, Emiliano Descrovi, Norbert Danz, Peter Munzert, Aleksei Anopchenko, and Francesco Michelotti. A full ellipsometric approach to optical sensing with bloch surface waves on photonic crystals. *Opt. Express*, 21(20):23331–23344, Oct 2013.

[56] J.-C. Weeber, A. Bouhelier, G. Colas des Francs, L. Markey, and A. Dereux. Submicrometer in-plane integrated surface plasmon cavities. *Nano Letters*, 7(5):1352–1359, 2007. PMID: 17439291.

[57] Colin J. Alleyne, Andrew G. Kirk, Ross C. McPhedran, Nicolae-Alexandru P. Nicorovici, and Daniel Maystre. Enhanced spr sensitivity using periodic metallic structures. *Opt. Express*, 15(13):8163–8169, Jun 2007.

[58] Richa Dubey, Elsie Barakat, Markus H?yrinen, Matthieu Roussey, Seppo K. Honkanen, Markku Kuittinen, and Hans Peter Herzig. Experimental investigation of the propagation properties of bloch surface waves on dielectric multilayer platform. *Journal of the European Optical Society - Rapid Publications*, 13(1), 2017.

[59] M. Patrini, M. Galli, F. Marabelli, M. Agio, L. C. Andreani, D. Peyrade, and Y. Chen. Photonic bands in patterned silicon-on-insulator waveguides. *IEEE Journal of Quantum Electronics*, 38(7):885–890, 2002.

[60] M. Galli, D. Bajoni, M. Belotti, F. Paleari, M. Patrini, G. Guizzetti, D. Gerace, M. Agio, L. C. Andreani, D. Peyrade, and Y. Chen. Measurement of photonic mode dispersion and linewidths in silicon-on-insulator photonic crystal slabs. *IEEE Journal on Selected Areas in Communications*, 23(7):1402–1410, 2005.

[61] D. M. Whittaker and I. S. Culshaw. Scattering-matrix treatment of patterned multilayer photonic structures. *Phys. Rev. B*, 60:2610–2618, Jul 1999.

[62] Marco Liscidini, Dario Gerace, Lucio Claudio Andreani, and J. E. Sipe. Scattering-matrix analysis of periodically patterned multilayers with asymmetric unit cells and birefringent media. *Phys. Rev. B*, 77:035324, Jan 2008.

[63] Peter Bienstman, S Selleri, L Rosa, HP Uranus, WCL Hopman, R Costa, A Melloni, LC Andreani, JP Hugonin, P Lalanne, D Pinto, SSA Obayya, M Dems, and K Panajotov. Modelling leaky photonic wires: a mode solver comparison. *OPTICAL AND QUANTUM ELECTRONICS*, 38(9-11):731–759, 2006.

[64] C. B. Burckhardt. Diffraction of a plane wave at a sinusoidally stratified dielectric grating. *J. Opt. Soc. Am.*, 56(11):1502–1508, Nov 1966.

[65] C. B. Burckhardt. Efficiency of a dielectric grating. *J. Opt. Soc. Am.*, 57(5):601–603, May 1967.

[66] Taylor K Fryett, Kyle L Seyler, Jiajiu Zheng, Chang-Hua Liu, Xiaodong Xu, and Arka Majumdar. Silicon photonic crystal cavity enhanced second-harmonic generation from monolayer wse 2. *2D Materials*, 4(1):015031, 2017.

[67] Krishanu Ray, Ramachandram Badugu, and Joseph R. Lakowicz. Bloch surface wave-coupled emission from quantum dots by ensemble and single molecule spectroscopy. *RSC Adv.*, 67(5), 2015.

[68] T. Sfez, E. Descrovi, L. Yu, D. Brunazzo, M. Quaglio, L. Dominici, W. Nakagawa, F. Michelotti, F. Giorgis, O.J.F. Martin, and H.P. Herzig. Bloch surface waves in ultrathin waveguides: Near-field investigation of mode polarization and propagation. *Journal of the Optical Society of America B: Optical Physics*, 27(8):1617–1625, 2010. cited By 29.

[69] Tristan Sfez, Emiliano Descrovi, Libo Yu, Marzia Quaglio, Lorenzo Dominici, Wataru Nakagawa, Francesco Michelotti, Fabrizio Giorgis, and Hans Peter Herzig. Two-dimensional optics on silicon nitride multilayer: Refraction of bloch surface waves. *Applied Physics Letters*, 96(15):151101, 2010.

[70] Sharon M. Weiss and Philippe M. Fauchet. Electrically tunable porous silicon active mirrors. *Physica Status Solidi (a)*, 197(2):556–560, 2003.

[71] Guoguang Rong, Ali Najmaie, John E. Sipe, and Sharon M. Weiss. Nanoscale porous silicon waveguide for label-free dna sensing. *Biosensors and Bioelectronics*, 23(10):1572 – 1576, 2008.

[72] W. Bogaerts, P. De Heyn, T. Van Vaerenbergh, K. De Vos, S. Kumar Selvaraja, T. Claes, P. Dumon, P. Bienstman, D. Van Thourhout, and R. Baets. Silicon microring resonators. *Laser & Photonics Reviews*, 6(1):47–73, 2011.

[73] Yoshihiro Akahane, Takashi Asano, Bong-Shik Song, and Susumu Noda. High-q photonic nanocavity in a two-dimensional photonic crystal. *Nature*, 425:944 EP –, 10 2003.

[74] Xiu-Bao Kang, Lan-Jun Liu, Hai Lu, Hai-Dong Li, and Zhi-Guo Wang. Guided bloch surface wave resonance for biosensor designs. *J. Opt. Soc. Am. A*, 33(5):997–1003, May 2016.

[75] Judson D. Ryckman, Marco Liscidini, J. E. Sipe, and S. M. Weiss. Porous silicon structures for low-cost diffraction-based biosensing. *Applied Physics Letters*, 96(17):171103, 2010.

[76] Kerry J. Vahala. Optical microcavities. *Nature*, 424:839 EP –, 08 2003.

[77] Parag B. Deotare and Marko Loncar. *Photonic Crystal Nanobeam Cavities*, pages 2060–2069. Springer Netherlands, Dordrecht, 2012.

[78] Daquan Yang, Huiping Tian, and Yuefeng Ji. High-q and high-sensitivity width-modulated photonic crystal single nanobeam air-mode cavity for refractive index sensing. *Appl. Opt.*, 54(1):1–5, Jan 2015.

[79] Kaiyuan Yao and Yaocheng Shi. High-q width modulated photonic crystal stack mode-gap cavity and its application to refractive index sensing. *Opt. Express*, 20(24):27039–27044, Nov 2012.

[80] Tsan-Wen Lu, Pin-Tso Lin, and Po-Tsung Lee. Photonic crystal horizontally slotted nanobeam cavity for silicon-based nanolasers. *Opt. Lett.*, 37(4):569–571, Feb 2012.

[81] Weixi Liu, Jialin Yan, and Yaocheng Shi. High sensitivity visible light refractive index sensor based on high order mode si3n4 photonic crystal nanobeam cavity. *Opt. Express*, 25(25):31739–31745, Dec 2017.

[82] Qimin Quan and Marko Loncar. Deterministic design of wavelength scale, ultra-high q photonic crystal nanobeam cavities. *Opt. Express*, 19(19):18529–18542, Sep 2011.

[83] Kartik Srinivasan and Oskar Painter. Momentum space design of high-q photonic crystal optical cavities. *Opt. Express*, 10(15):670–684, Jul 2002.

[84] Eiichi Kuramochi, Hideaki Taniyama, Takasumi Tanabe, Kohei Kawasaki, Young-Geun Roh, and Masaya Notomi. Ultrahigh-q one-dimensional photonic crystal nanocavities with modulated mode-gap barriers on sio2 claddings and on air claddings. *Opt. Express*, 18(15):15859–15869, Jul 2010.

[85] Qimin Quan, Parag B. Deotare, and Marko Loncar. Photonic crystal nanobeam cavity strongly coupled to the feeding waveguide. *Applied Physics Letters*, 96(20):203102, 2010.

[86] D. Comoretto et al. *Organic and hybrid photonic crystals*. Springer, 2015.

[87] Allen Taflove and Susan C. Hagness. *Computational electrodynamics: the finite-difference time-domain method*. Artech House, Norwood, 3rd edition, 2005.

[88] Marek S. Wartak. *Computational Photonics: An Introduction with MATLAB*. Cambridge University Press, 2013.

[89] Sergei V. Zhukovsky, Lukas G. Helt, Dongpeng Kang, Payam Abolghasem, Amr S. Helmy, and J.E. Sipe. Analytical description of photonic waveguides with multilayer claddings: Towards on-chip generation of entangled photons and bell states. *Optics Communications*, 301-302:127 – 140, 2013.

[90] Zhenshan Yang, Marco Liscidini, and J. E. Sipe. Spontaneous parametric down-conversion in waveguides: A backward heisenberg picture approach. *Physical Review A*, 77(3):033808, 2008.

[91] R. de L. Kronig and W. G. Penney. Quantum mechanics of electrons in crystal lattices. *Proc. Roy. Soc.*, A130:499, 1930.

[92] Bahaa E. A. Saleh and Malvin Carl Teich. *Fundamentals of Photonics*. Wiley, New York, 2007.

[93] Giuseppe Grosso and Giuseppe Pastori Parravicini, editors. *Solid State Physics*. Academic Press, Amsterdam, second edition edition, 2014.

[94] Eli Yablonovitch. Inhibited spontaneous emission in solid-state physics and electronics. *Phys. Rev. Lett.*, 58:2059–2062, May 1987.

[95] Sajeev John. Strong localization of photons in certain disordered dielectric superlattices. *Phys. Rev. Lett.*, 58:2486–2489, Jun 1987.

[96] E. Yablonovitch. Photonic band-gap structures. *J. Opt. Soc. Am. B*, 10(2):283–295, Feb 1993.

[97] J.D. Joannopoulos, S. G. Johnson, J. N. Winn, and R. D. Meade. *Photonic Crystals: Molding the Flow of Light*. Princeton University Press, II edition (2011).

List of publications

Publications:

1. Yu Wang, **Daniele Aurelio**, Wenyi Li, Peter Tseng, Zhaozhu Zheng, Meng Li, David L. Kaplan, Marco Liscidini, Fiorenzo G. Omenetto, "Modulation of Multiscale 3D Lattices through Conformational Control: Painting Silk Inverse Opals with Water and Light", *Adv. Mater.* 29(38) (2017) (link).

2. **Daniele Aurelio**, Marco Liscidini, "Electromagnetic field enhancement in Bloch surface waves", *Phys. Rev. V* 96(4) (2017) (link)

3. Hajar Kaviani Baghbadorani, **Daniele Aurelio**, Jamal Barvestani, Marco Liscidini, "Guided Modes in Photonic Crystal Slabs Supporting Bloch Surface Waves", *J. Opt. Soc. Am. B* 35, 805-810 (2018) (link)

4. Gilberto Rodriguez, **Daniele Aurelio**, Marco Liscidini, Sharon M. Weiss, "Bloch surface wave ring resonator based on porous silicon" (in preparation)

Proceedings

1. Gilberto Rodriguez, Matteo Menotti, **Daniele Aurelio**, Marco Liscidini, and Sharon Weiss, "Bloch Surface Wave Ring Resonators", *CLEO: QELS Fundamental Science 2016, Poster Session - Thursday (JTh2A)* – (CLEO Proceedings: link)

2. **Daniele Aurelio**, Tommaso Perani, Marco Liscidini, "Light Confinement in Resonators Based on Bloch Surface Waves", *ICTON 2018 proceedings* (in press)

Talks:

1. **Daniele Aurelio**, "Electromagnetic field enhancement in Bloch surface waves", FisMat 2017 - *Italian national conference on the Physics of Matter* (Nanophotonics, plasmonics and photovoltaics section) - Trieste (Italy), October 1-5, 2017 (contributed)

2. **Daniele Aurelio**, Tommaso Perani, Marco Liscidini, "Light Confinement in Resonators Based on Bloch Surface Waves", ICTON 2018 - *International Conference on Transparent Optical Networks*, Bucharest (Romania), July 1-5, 2018 (**invited**)

Presented posters:

1. Gilberto Rodriguez, Matteo Menotti, **Daniele Aurelio**, Marco Liscidini, Sharon Weiss, Bloch surface wave ring resonator @ SIOF (Società Italiana di Ottica e Fotonica) *School of Photonics 2016, Plasmonics and Nano-optics* - Cortona (Italy), July 10-14, 2016.